Institut für Theoretische Physik
der
Technischen Universität München
Lehrstuhl: Univ.-Prof. Dr. F. Schwabl

Collective Dynamics of Molecular Motors

Andrej Vilfan

Vollständiger Abdruck der von der Fakultät für Physik der Technischen Universität München zur Erlangung des akademischen Grades eines

Doktors der Naturwissenschaften (Dr. rer. nat.)

genehmigten Dissertation.

Vorsitzender:	Univ.-Prof. Dr. E. Sackmann
Prüfer der Dissertation:	
1.	Univ.-Prof. Dr. F. Schwabl
2.	Univ.-Prof. Dr. S. Fischer
3.	Univ.-Prof. Dr. W. Götze (schriftliche Beurteilung)

Die Dissertation wurde am 14. 1. 2000 bei der Technischen Universität München eingereicht und durch die Fakultät für Physik am 2. 8. 2000 angenommen.

Danksagung

An dieser Stelle möchte ich mich bei allen bedanken, die zum Gelingen dieser Arbeit beigetragen haben. Bei Herrn Prof. Dr. F. Schwabl bedanke ich mich für die interessante Themenstellung und ständige Unterstützung während der Arbeit. Bei Dr. habil. Erwin Frey möchte ich mich für die engagierte Betreuung bedanken.

Herrn Prof. Dr. Eckhard Mandelkow und Dr. Manfred Thormählen danke ich für fruchtbare Zusammenarbeit auf dem Gebiet der Dekorationsexperimente, ohne die der zweite Teil dieser Arbeit nicht zustande gekommen wäre. Dort, wo meine Arbeit das Gebiet der Reaktions-Diffusions-Modelle berührt, war für mich der Rat von Dr. Jaime Santos und Dr. Uwe Täuber unschätzbar. Für Ratschläge aus dem Bereich der semiflexiblen Polymere und für viele hilfreiche Diskussionen bedanke ich mich bei Dr. Klaus Kroy und Jan Wilhelm. Für wertvolle Hilfe bei verschiedenen Fragen aus dem Bereich der Biophysik möchte ich mich bei Herrn Prof. Dr. Erich Sackmann und seinen Mitarbeitern, besonders bei Dr. Rudolf Merkel, bedanken.

Auch bei allen anderen Kollegen bedanke ich mich für ihre stete Hilfsbereitschaft und angenehme Arbeitsatmosphäre.

Schließlich bedanke ich mich beim Cusanuswerk für das Stipendium, das ich im ersten Teil meiner Promotion erhalten habe, und für die Zeit, an die ich mich gerne erinnern werde. Im zweiten Teil wurde meine Arbeit von der Deutschen Forschungsgemeinschaft im Rahmen des SFB 413 unterstützt.

Contents

Indeed, biologists in general have paid too little attention to the quantitative aspects of their work in the past few hectic decades.

John Maddox [107]

Chapter 1

Introduction

1.1 The diversity of biological motors

The quest for the origins of biological motion belongs to the oldest fields of science and goes back to the old Greeks. In the 3rd century BC, Erasistratus of Ceos, an anatomist and physician from Alexandria, seeked for the cause of movement in the "animal spirit" [55], a kind of subtle vapour being formed in brain and transported through the body by nerves. The view that muscle movement is driven by some fluid has persisted until the 17th century, when the Dutch biologist Jan Swammerdam found out that muscles change their shape during contraction, but not their volume. However, at that time it was still not clear that biological matter obeys the same laws of physics and chemistry as non-living objects. The idea that muscle is a chemical engine using isothermal combustion was first articulated by Hermann von Helmholtz in his work "Über die Erhaltung der Kraft[1]" in 1847.

Later on it was shown that energy liberation in muscles depends on the velocity of shortening [47] and that its source is the hydrolysis of ATP (adenosine

[1]With "Kraft" he actually meant energy

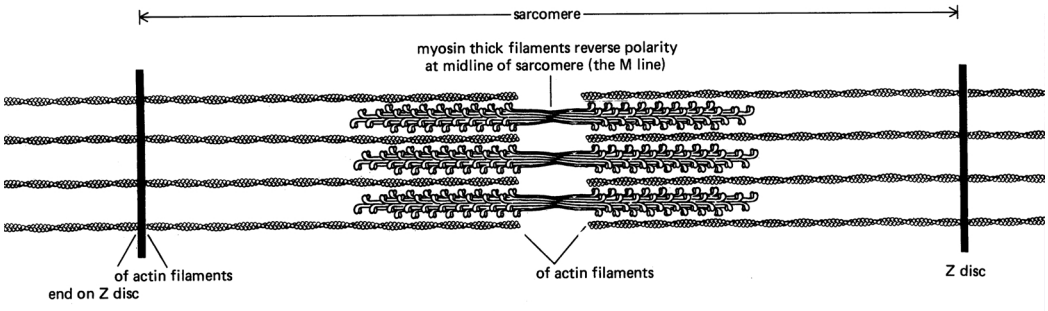

Figure 1.1: Schematic representation of a sarcomere (the basic contractile unit in a muscle). A muscle contracts as thick filaments (myosin) and thin filaments (actin) glide past each other, driven by cross-bridges (myosin heads). From [2].

triphosphate) [44]. The relation of tension on a piece of muscle and its shortening velocity was measured by A.V. Hill in 1938 [63]. The discovery that there are two essential proteins in muscles, namely actin and myosin followed soon [152].

In the 50$^{\text{ies}}$, H.E. Huxley [78] and A.F. Huxley[2] [74] showed that actin and myosin form two sets of filaments which glide past each other and do not contract themselves, as has been thought previously (Fig. 1.1). Seeking the answer to the question what causes the filaments to glide, the so called cross-bridges which link both filaments (later identified as myosin heads) have been discovered [76]. A quantitative theory for the generation of force was developed by A.F. Huxley [73]. The following decades provided more and more detailed evidence on the microscopic structure and function of myosin. A reaction scheme for the operation of myosin cross-bridges and the connected ATP hydrolysis was proposed by Lymn and Taylor [103]. In refined physiological measurements (e.g. [75, 52]) it was investigated how the force reacts to a stretch occurring at a non-uniform velocity.

The second motility process that has been thoroughly investigated was the beating of cilia and flagella. Flagella are used by sperm cells and certain protozoa for cell propulsion. They are about 50 microns long, 0.25 μm in diameter, and can generate waves with a constant amplitude and a typical frequency of 30 s^{-1}. These waves then propel the cell. They usually spread from the cell towards the end of the flagellum, but there are also some exceptions [34]. Flagella contain a bundle of microtubules, called the axoneme. Between each pair of microtubules, there

[2]The common surname is mere coincidence. Not so with the writer Aldous Huxley, who was brother of A.F. Huxley.

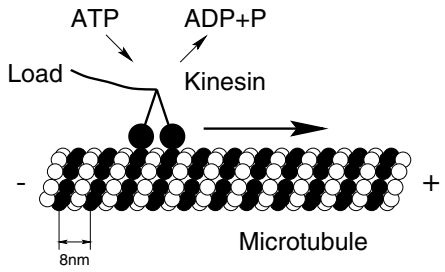

Figure 1.2: Motion of kinesin along microtubules.

are dynein motors every 24 nm which pull the microtubules along each other, thus bending them. Like in case of the myosin motor, the necessary energy is gained from ATP hydrolysis. Cilia are very similar to flagella in their composition, however shorter. They also have a more complex regulatory apparatus [2]. They cover the surfaces of mammalian respiratory passages (e.g. the nose) where they move outwards particles that have been collected in the secretions. Cilia also seem to be involved in establishing the left-right asymmetry during the growth of an organism [1, 2]. Some protozoa are covered with cilia and use them for locomotion. They beat in a whiplike fashion with typical frequencies of 5-10 s^{-1}.

In the 80^{ies}, a third family of motor proteins, namely the kinesins, was discovered [20]. Some eucaryotic cells can grow very long, in the case of nerve cells up to 1 m. Since proteins can only be synthesised in the cell body, they have to be transported to the periphery. The time needed to reach the destination by means of diffusive motion grows with the square of the distance and diffusion therefore soon becomes useless as transport mechanism. Kinesin has been found to perform directed motion along microtubules, which are one of the components of the cytoskeleton [69]. It usually comes with two heads (which actually act as "legs") and "walks" along microtubules towards their "+" end (i.e. cell periphery) over long distances without detaching (Fig. 1.2). Some representatives reach maximum velocities of about 2.5 μm/s (20 cm/day). The heads are connected to a tail domain, which can bind a cargo like a vesicle or an organelle. Further motors involved in the intracellular transport belong to the cytoplasmic dynein and myosin families. Each cell contains a large number of diverse motors differing in their directionality, velocity, the kind of tracks they use and the cargo they bind [2, 34]. Among others, jamming of the kinesin-based transport has been brought into connection with the Alzheimer's disease [110]. Microtubules and their asso-

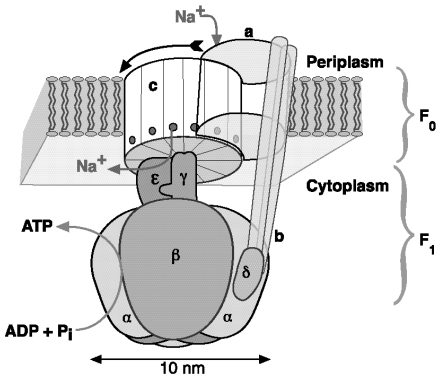

Figure 1.3: A schematic representation of the F_1-F_0-ATP synthase (ATPase) from Ref. [37].

ciated motor proteins also play a crucial role in cell division and separating the chromosomes [150, 2, 34].

Besides the linear motors mentioned by now, there also exists a family of rotary motors. Their best known member is the bacterial flagellar motor (not to be mixed up with wave generation in flagella of eucaryotic cells, driven by dynein) [15, 116, 2]. It is driven by a proton (or sodium ion) flux through the membrane and not by ATP. The rotation reaches speeds of over $100\,\mathrm{s}^{-1}$. Connected to the rotor is a helical flagellum with a certain handedness. If the rotor rotates counterclockwise, several flagella draw together into a coherent bundle and the bacterium swims uniformly into one direction. If the rotor starts rotating clockwise, the flagella fly apart and the bacterium starts tumbling. The switching between directed and random motion gives the bacterium a simple mechanism to search for places with higher food concentration.

A similar mechanism is used by the F_1-F_0-ATP synthase (or ATPase) [19, 123, 182, 37][3]. It is composed of two coupled rotary motors, F_0 and F_1. The F_0 motor is driven by a proton gradient, similar as flagellar motors, while the F_1 part hydrolyses ATP. Both are reversible and can therefore either use a proton gradient to synthesise ATP or hydrolyse ATP to pump protons. The F_1 part operates with an efficiency close to 100% [182]. A schematic representation of the F_1-F_0 motor is shown in Fig. 1.3.

Further mechanisms for generating biological motion include filament polymerisation of actin [118] or tubulin [38], the motion of the RNA Polymerase [176]

[3]Its discovery was awarded with the Nobel prize for chemistry in 1997

(see also [82, 175] for theoretical models) and others.

1.2 Newer experimental techniques

Besides the well established physiological and biochemical measurements, a new series of *in vitro* experiments was started in the 80$^{\text{ies}}$. First there were the gliding assays in which myosin motors were fixed to the glass surface and were able to move fluorescently labelled actin filaments in a worm-like manner [93, 162, 60]. These experiments have shown that the head fragment of myosin is sufficient to move actin [162]. Further, they have shown that the sliding velocity depends on the number of active myosin heads [163]. Other interesting findings were that the actin filaments rotate according to their helical structure during sliding [122]. Theoretical considerations concerning the dynamics of filaments in a gliding assay can be found in Refs. [145, 40, 18].

A striking result of the gliding assays was the finding by Spudich and coworkers that sliding velocity is proportional to the length of the lever-arm (part of the myosin molecule between the head and the tail) [164]. This confirmed the hypothesis that a conformational change in the motor head is amplified by the lever arm to produce a step of about 10 nm.

In conventional gliding assays one has little influence on the force, which is given by the hydrodynamic friction. Therefore a new technique was developed using an electric field to produce an external force on the filament. It allowed for the measurement of velocity relations over a broad range of forces [141]. Interestingly, the results indicate a hysteresis in the force-velocity curve.

Gliding assays were also used for studying kinesin [71, 72], recently also for single-headed molecules [58]. They have become a standard method to observe the influence of mutations on the velocity and direction of motion (e.g. [61]). Since a single molecule of kinesin can move over long distances, one can also reverse the experiment and observe fluorescently labelled kinesin molecules moving along fixed microtubules [165].

The use of optical tweezers (Fig. 1.4) [6, 147] and other micromechanical techniques [180] allowed for a completely new insight into the operation of motors. In the case of kinesin, the stepping of single molecules could be observed [96, 155, 29]. Force-velocity relations have been measured this way [153, 89, 30, 172]. In addition to the average velocity, the measurement of fluctuations [153, 143, 172]

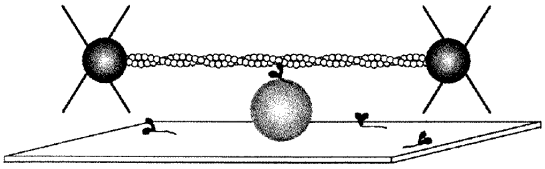

Figure 1.4: The use of optical tweezers to study the single-molecule mechanics of myosin [49]. An actin filament is held between two optical tweezers and brought into the vicinity of a bead covered with myosin molecules.

has provided substantial information about the operation of motors. In the case of myosin one is able to observe how a single head attaches to actin, pulls on it (power-stroke) and releases again [49, 119, 167, 147, 180, 80, 157, 168, 48]. In some cases even two different states could be recognised [168]. While there was initially quite some discrepancy concerning the power-stroke amplitude (the values lay between 4 nm [119] and 23 nm), the newer results [157, 167] seem to have settled at $6-10$ nm (except for the observation of multiple consecutive steps [87], which has not yet found an independent confirmation). A review on optical methods in single-molecule biomechanics can be found in [114].

In parallel, structural investigations have helped uncovering the molecular mechanism of the operation of motors. The structure of single proteins (actin [85], myosin on actin [139], kinesin [95]) has been solved in many cases using X-ray crystallography. Interaction between motors and their tracks was studied in the so called "decoration" experiments, in which actin or tubulin [148, 66, 5, 65, 68, 159] filaments are covered with motor proteins at high densities and then analysed using scanning transmission electron microscopy (STEM) with subsequent 3-D image reconstruction.

1.3 Theoretical modelling

The pioneering work in modelling muscle contraction has been done by A.F. Huxley. In his 1957 article [73] he proposes the basic mechanism of the swinging cross-bridge as the force generating element in muscles. At that time, the structure of muscles composed of actin and myosin filaments was already well established, however not much was known about the myosin heads. It is therefore remarkable how much resemblance the model bears with later models based

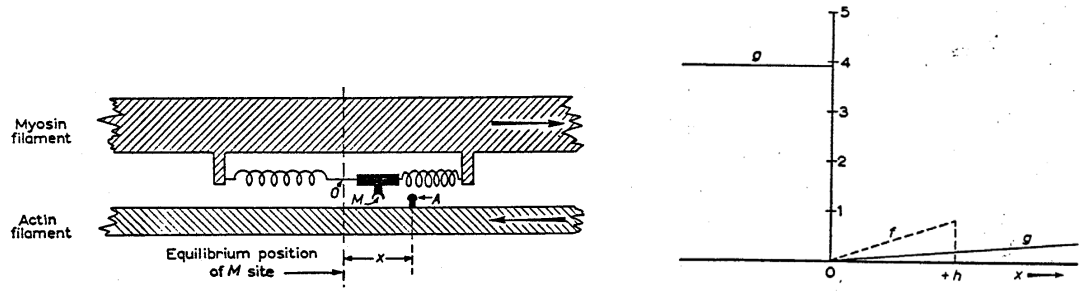

Figure 1.5: (a) Diagram illustrating the original Huxley's model [73] for force generation in muscles. (b) Attachment rate (f) and detachment rate (g) as a function of the relative position of the binding site.

on microscopic data[4]. The basic principle of his model is shown in Figure 1.5a. A cross-bridge which can move in the x-direction can be either in the detached or the attached state. The transition probabilities are given by curves shown in Fig. 1.5b (their form has been chosen in a way to allow analytical calculation). The resulting force was able to explain force-velocity curves from Hill's measurements [63].

Huxley's original model did not contain an explicit conformational change in the cross-bridge. It postulated that the cross-bridge moves back and forth about its equilibrium position as a result of thermal fluctuations. If it is strained to one side and there is a binding site under it, it can bind with a certain rate $f(x)$. An attached head detaches with a certain rate $g(x)$, preferably after it has done its work. Therefore, this model is usually considered as a "thermal ratchet" model [69]. However, whether Huxley's models is a "power-stroke" or a "thermal ratchet" model is not as much a question of the model equations themselves as of their physical interpretation. An asymmetric attachment rate is actually equivalent to a symmetric attachment rate if the attachment is followed immediately by a conformational change (power stroke) that shifts the equilibrium position.[5]

[4]Over four decades later, the author commented proudly: "At that time a *prediction* was still a *prediction* — nowadays one calls it *prediction* if one is able to fit the data." A.F. Huxley during his talk at the Discussion meeting on the molecular physics of biological movement, London, 14.-15. April 1999

[5]On the other hand, Huxley's model differs form the majority of contemporary "ratchet" models in the sense that it proposes discrete binding sites and does not allow an attached head to switch directly from one binding site to the next one (in most ratchet models [83] a motor

In the subsequent years, more detailed physiological experiments on muscles, combined with early structural investigations [77] provided data for modelling force generation in muscles [75]. Measurement of the change in tension after a sudden alteration of the length have been especially elucidating [134]. A four-state model based on these data and its mathematical solution can be found in Ref. [43]. The model did not need much change to remain consistent with experiments in the following years [28].

Parallel to more or less complex physiological models, a new series of physical models has emerged in order to concentrate on some specific properties of motors. In this context we should first mention the model developed by Leibler and Huse [99]. They introduced the classification of motors into "porters" (also called processive motors, or motors with a high duty ratio [70]) and "rowers" (nonprocessive motors, low duty ratio). Porters are able to "walk" and carry loads (therefore the name "porter") over long distances. Their best known representative is kinesin. Rowers, on the other hand, spend little of their time in the strongly bound state, like the rowers on a boat only keep their oars in water for a certain fraction of time. They have to operate in groups in order to be able to pull against an external load[6]. Another example of a simplified 3-state model is reviewed in [158]. Among other results, the article points out how a motor can act as oscillator.

Another simplified version of the 4-state model was recently studied by T. Duke [42]. He reduced the strain-dependence of the transition rates (which has been modelled in a very arbitrary fashion in some previous models, e.g. [133]) to the contributions which follow directly from the change in the free energy. The model provided an explanation of many mechanical and thermodynamic properties of the muscle. Moreover, Duke shows that synchronisation between cross-bridges can occur under certain conditions. This means that a filament in muscle can move stepwise although it is subject to a constant force. Then the use of mean-field like methods solving the differential equations at a constant velocity, which has been used by all previous models, becomes invalid. Once again, this work demonstrated how a minimised model can bring more analytical insight and elucidate aspects that have previously remained hidden in the complexity.

can stay in the strongly bound state and still move over an unlimited distance).

[6]Here the difference between molecular motors and the real rowers comes to expression: due to inertia a boat could well be propelled by a single rower while the motor molecule, dominated by Brownian motion, would immediately loose contact with its track.

The abstraction went one step further in the so called "ratchet" models. They use an asymmetric periodic (usually sawtooth-like) potential in connection with temporally correlated fluctuations to generate directed motion. This can either be achieved in the presence of coloured noise [108, 13], or the fluctuations modulate the potential itself [136, 83, 8, 183, 36]. Ratchet-models have also been developed for the polymerisation of actin-filaments [131], for interacting particles [35, 32] and for a large group of stiffly coupled particles, a situation similar to the actin-myosin motor [83, 84, 81]. They have also been applied to kinesin [8, 36, 9] and recently to the F_1-F_0-ATPase [37]. The charming property of ratchets is that they allow a description in terms of a position-dependent potential [136], which can have a different form in each state (most models consider two states). Some important results of this approach have been the prediction of the existence of anomalous force-velocity relations [83] and the finding that the efficiency can reach its maximum far from equilibrium [129]. Nonetheless, the ratchet mechanisms have already found direct experimental realisation [46, 7] and might be technologically applicable, for instance as particle separation devices. A review on ratchet models can be found in Ref. [81]. For comments on their relation to biological systems also see Refs. [105, 106, 98].

It is not easy to draw a clear line between the "power-stroke" and the "ratchet" models. In power-stroke models the potential describing the behavoiur of a head upon mechanical deformations is different (shifted as whole) for each binding site. In ratchet-models, the periodicity of binding sites is included in the potential and therefore the state is uniquely described by a the position and the chemical state of a particle (motor), without needing the information on which binding site it is attached. Therefore a clear difference between both types of models is that ratchets allow slippage between the wells (binding-sites) without a change in the chemical state of the particle. Another difference is that many ratchet models need a finite viscous friction, while the power-stroke models assume quick equilibration of the probability distribution within a state[7].

Another phenomenological model was published recently by M. Fisher and Kolomeisky [50]. It describes a motor by the coordinate of the site on which it is bound and one of N states. The approach allows some general considerations

[7] In Ref. [9] the authors claim that power-stroke models are characterised by a "deterministic visco-elastic relaxation step" while every model containing a thermally activated transition is a thermal ratchet model. According to this classification, almost all existing models base on the ratchet mechanism.

about force-velocity curves in the case that the steps between the sites are tightly coupled to transitions between chemical states.

Models for kinesin have to account for its two-headed nature and therefore need a somewhat more specific approach. The model by Peskin and Oster [132] proposes that the rear head is always less likely to unbind than the front one. A free head can bind in front of or behind the bound head, depending on the mechanical load on kinesin. Duke and Leibler discussed a model with minimum mechanochemical coupling [41]. The model of Derényi and Vicsek [36] proposes that kinesin moves by pulling the two heads together and apart. A simple ratchet model was applied to kinesin by Astumian and Bier [8] and refined later [9].

Contrary to moving motors, decoration experiments have not yet been the subject of a theoretical study. Yet as we will show they touch many of fields that have been thoroughly investigated in the past. Irreversible adsorption of dimers and other shapes onto one- or more-dimensional lattices has been referred to as random sequential adsorption (RSA) and has been reviewed by Evans [45]. Reversible binding of stiff dimers (and n-mers) has also been studied in the context of DNA-protein interactions, e.g. [111]. An extensive review on cooperative and non-cooperative ligand binding models has been written by T.L. Hill [64]. The continuous version of RSA, called "parking lot" model (cars of equal length parking at the side of a road), has also been studied in its irreversible and reversible version (e.g. [90, 156]). Finally, we will show that the dynamics of the reversible dimer adsorption model can be mapped to reaction-diffusion models, which have been a major topic of statistical mechanics during the last decade. In some cases they have been exactly solved by being mapped to quantum spin chains [3] or other exact models [137] and by using renormalisation group theory [130]. See [26] for a review.

1.4 Outline

The outline of this Thesis is the following. In Chapter 2 we introduce a two-state model for motor proteins, based on a power-stroke mechanism. We study its force-velocity characteristics and show that they can show a higher variety than previously discussed. The simplicity of the model also allows us to find analytical criteria for their classification. In Chapter 3 we extend the model by introducing elastic coupling between the motors. Unlike with stiffly coupled motors, the

mean-field like approach looses its validity. We therefore develop an approximate analytical solution and compare the results with simulation data. Anomalous f-v relations combined with elastic coupling are studied in Chapter 4. We show that such a model leads to spontaneous generation of waves, similar to those observed in cilia and flagella.

In Chapter 5 we turn to cooperative properties of passive dimeric motors. With "passive" we mean that they do not obtain any energy from ATP hydrolysis and therefore obey the law of detailed balance. Our study is motivated by decoration experiments with kinesin on microtubules, which have become one of the major methods for investigating kinesin's structure and function. We first treat the equilibrium behaviour of the dimer adsorption model. Steady-state fluctuations and the relaxation from an initial state far from equilibrium are studied in Chapter 6. We finally extend the dimer adsorption model by introducing an attractive interaction in Chapter 7. It leads to a phase transition between the empty and the decorated phase, analogue to the phase transition in the two-dimensional Ising model. We also address the question how the system reaches the ordered state.

Chapter 2

Force-velocity-relations

In this Chapter we introduce a simple two-state power-stroke model and discuss its force-velocity relations. We take into account that the detachment rates may depend on the strain on the motor. We will show that depending on the functional form of these rates, the model can show a much greater variety of phenomena than previously discussed [73, 99]. These include linear, hyperbolic, anomalous or kinesin-like force-velocity relations. Most results from this Chapter have been published in [171].

2.1 Definition of the model

In the two-state model each motor molecule has two long living states: attached and detached. The duty cycle of a head is shown schematically in Figure 2.1. Our basic model corresponds to the model introduced by Leibler and Huse [99] when only the time limiting steps important for mechanical properties are taken into account. Two-state models have also been used previously for myosin [73] and kinesin [132, 41] as well as in ratchet models [81, 8]. We generalise the two-state model by introducing arbitrarily strain-dependent transition rates and discrete binding sites. Both extensions are crucial for a qualitative and quantitative explanation of experiments.

We define the model as follows. N motors are positioned with their roots on a stiff backbone (the effects of an elastic backbone will be studied in Chapter 3) and can attach to the molecular track (actin or tubulin) as shown in Fig. 2.3. Let x denote the position of a head (free or bound) and y the position of its root at the backbone. $\xi = x - y$ then denotes the strain on a head. Deformations of

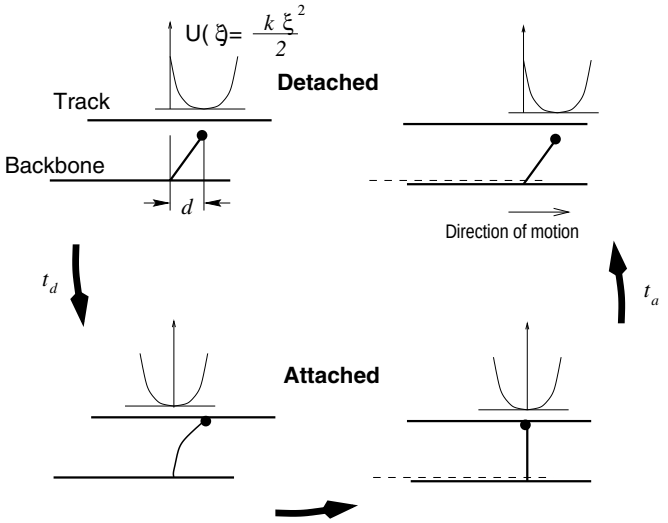

Figure 2.1: A schematic diagram of the two-state cross-bridge model. A free head, anchored in the *backbone* attaches to the *track* with a transition rate t_d^{-1}. Deformations of a head are described in terms of the harmonic potential $U(\xi)$. While the detached head is leaning forwards, it goes through a conformational change immediately after the attachment, making it strained and thus generating force between the track and the backbone. After some time, the head detaches with some given rate, goes through the conformational change again and the cycle can repeat.

a head can be described in terms of a harmonic potential $\mathcal{H} = U(\xi - \xi_d)$ with $U(\xi) \equiv \frac{1}{2}k\xi^2$. After attaching to or detaching from the track, a conformational change in the head, described by shifting the potential by the distance d, takes place, *i.e.* $\xi_d = 0$ in the attached (A) state and $\xi_d = d$ in the detached (D) state. This is the *first spatial asymmetry* in our model and constitutes the basic mechanism for the generation of directed motion. We assume that the transitions between the two states occur stochastically with characteristic times t_a and t_d and that the overall attachment rate t_d^{-1} of a free head is constant. There are two possible microscopic scenarios in which the last assumption is valid. First, such behaviour can be expected if some reaction has to take place before a free head comes into the affine state, which then performs a three-dimensional random walk and quickly attaches to the track (Fig. 2.2a). Alternatively, one could obtain equivalent behavoiour if the time-limiting step consists of non-specific binding to the track instead of the transition to the high-affinity state. On a two-dimensional track with punctual binding sites, the attachment to one of the binding sites is still preceded by a two-dimensional random walk. The probability that the head

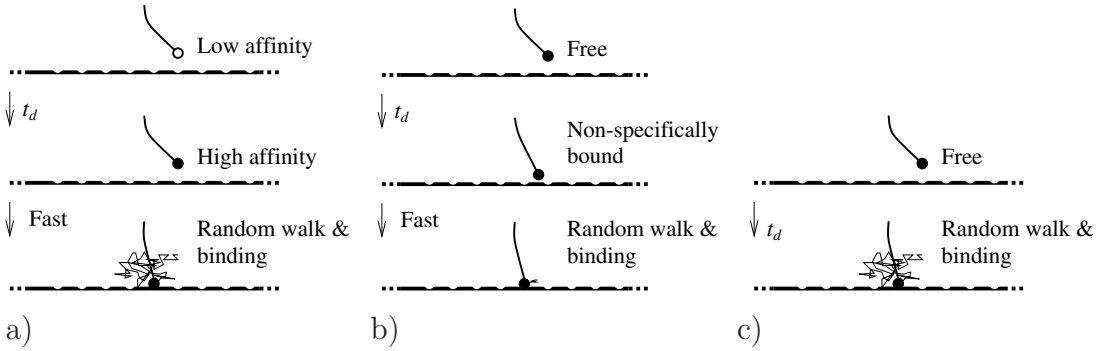

Figure 2.2: Three different binding scenarios for a head. In scenario a) some reaction has to take place before a free head comes into the affine state, which then performs a three-dimensional random walk and quickly attaches to the track. In scenario b) the head first binds non-specifically and then performs a one-dimensional random walk before it binds specifically. In scenario c) the time-limiting step is the random walk itself. We choose the scenario a) in our calculation.

attaches to the site positioned at $x = id$ is proportional to the Boltzmann factor $\exp(-\beta U(x - y - d))$ (with normalisation $\sum_i W_i = 1$)

$$W_i = \frac{e^{-\beta U(ia-y-d)}}{\sum_j e^{-\beta U(ja-y-d)}} \,. \tag{2.1}$$

Here a denotes the separation between the binding sites ($a = 5.5\,\mathrm{nm}$ on actin and 8 nm on microtubules [155]). The same approach (constant total attachment rate and Boltzmann distributed probabilities for binding to a certain site) has also been used by Duke and Leibler in their kinesin model [41]. We will choose this scenario in our further calculation.

A slightly modified scenario was used by Peskin and Oster [132]. They assume a time limiting step consisting of non-specific binding to the track. Afterwards, they assume that a *one-dimensional* random walk takes place as the head "searches" for the next binding site to bind specifically. This scenario is shown in Fig. 2.2b. It also leads to a constant total attachment rate t_d^{-1}, but the probabilities W_i are different than in our scenario. With parameters for kinesin one can show that the difference between this and the first scenario in terms of the force-velocity relation is insignificant.

A third class of models assumes that the time-limiting step is the random walk itself (Fig. 2.2c). This approach has been used in many muscle models, e.g. [73, 158]. Then the attachment rate is not constant any more but depends on

the Boltzmann factors of the binding sites, $t_d^{-1} \propto \sum_i e^{-\beta U(ia-y-d)}$.

An experimental estimate for the amplitude of thermal fluctuations of a free myosin head with data from Ref. [48] ($k = 0.4\,\mathrm{pN/nm}$, $d = 10\,\mathrm{nm}$) gives $\sigma = \sqrt{k_\mathrm{B}T/k} \approx 0.3\,d$. While we assumed a constant attachment rate t_d^{-1}, there is strong experimental evidence for a strain-dependent detachment rate t_a^{-1} of myosin. On one hand, single-molecule in vitro experiments [49, 80] show a strain-dependent detachment rate t_a^{-1} of myosin. Besides, it has been known for a long time that energy liberation rate in muscles depends on the external force (Fenn effect) [47]. This means that the duration of one hydrolysis cycle depends on the external force (or velocity, which is a function of force). Therefore at least one step in the cycle has to be strain-dependent.

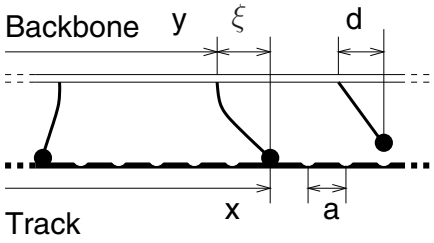

Figure 2.3: Schematic model for the motor heads running along a molecular track.

In generally $t_a(\xi)$ will be an asymmetric function, thus bringing a *second asymmetry* into the model.

2.2 Master equations

We start our analysis by considering a large group of N rigidly coupled independent motors, a situation typical for the actin-myosin motor in muscles. Then the velocity fluctuations resulting from the stochastic operation of single motors can be neglected. We set up a Master equation for the probability density $\Phi_a(\xi, t)$ for a motor being attached with strain ξ at time t and probability $\Phi_d(t)$ for a motor being detached. We also need the probability density $P(\xi, y)$ that a motor at y attaches with a given strain ξ. This will in general depend on the actual position of the motor head y with respect to the binding sites ($x_i = ia$), which is again correlated with the detachment positions. However, this correlation vanishes either for a strain-independent detachment rate or if the motors have a low duty ratio (they spend most of the time in the detached state), which is the case for

myosin. In this case we can replace

$$P(\xi, y) \equiv \sum_i W_i \delta(\xi + y - ia) = \sum_i \frac{e^{-\beta U(\xi - d)}}{\sum_j e^{-\beta U(\xi - d + ja)}} \delta(\xi + y - ia) \,, \tag{2.2}$$

which is a periodic function in y with period a by its average $P(\xi)$

$$P(\xi) \equiv \frac{1}{a} \int_{i_0 a}^{(i_0+1)a} dy P(\xi, y) = \frac{1}{a} \frac{e^{-\beta U(\xi - d)}}{\sum_j e^{-\beta U(\xi - d + ja)}} \,, \tag{2.3}$$

which is, of course, still normalised to 1.

The probability Φ_d and probability density Φ_a obey the following Master equations

$$(\partial_t - v\partial_\xi)\, \Phi_a(\xi, t) = \frac{\Phi_d(t)}{t_d} P(\xi) - \frac{\Phi_a(\xi, t)}{t_a(\xi)} \tag{2.4a}$$

$$\partial_t \Phi_d(t) = -\frac{\Phi_d(t)}{t_d} + \int_{-\infty}^{\infty} d\xi \, \frac{\Phi_a(\xi, t)}{t_a(\xi)} \,, \tag{2.4b}$$

with normalisation

$$\Phi_d(t) + \int_{-\infty}^{\infty} \Phi_a(\xi, t) d\xi = N \,. \tag{2.4c}$$

The force produced by the group of motors is given by

$$F(t) = \int_{-\infty}^{\infty} d\xi \, \Phi_a(\xi, t) \partial_\xi U(\xi) \,. \tag{2.5}$$

For a constant positive velocity we have to find stationary solutions of Eq. 2.4. They read

$$\Phi_a(\xi) = \frac{N \int_{-\infty}^{\infty} d\zeta \, G(\xi, \zeta) \, P(\zeta)}{v t_d + \int_{-\infty}^{\infty} d\xi' \int_{-\infty}^{\infty} d\zeta \, G(\xi', \zeta) \, P(\zeta)} \,, \tag{2.6a}$$

$$G(\xi, \zeta) = \exp\left(- \int_{\xi}^{\zeta} \frac{d\xi'}{v t_a(\xi')} \right) \theta(\zeta - \xi) \,, \tag{2.6b}$$

where $G(\xi, \zeta)$ is a Green's function which can be interpreted as the probability that a motor which has got bound to the track with strain ζ still remains bound when its strain reaches ξ. An example of the functions $P(\xi)$ and $\Phi_a(\xi)$ is shown if Figure 2.4.

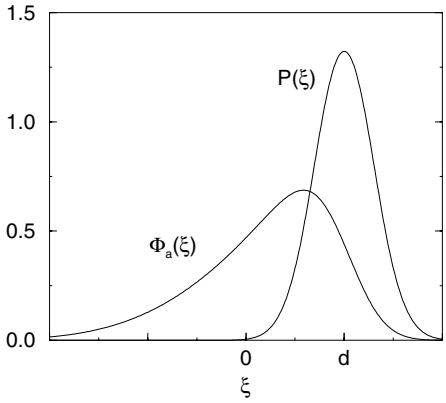

Figure 2.4: The distribution of strain at attachment time $P(\xi)$ and among all attached heads, $\Phi_a(\xi)$ (not normalised). Data were calculated with $\sigma = 0.3\,d$, $a = 0.55\,d$, $t_a(\xi) = t_a^0 \exp(\alpha\xi)$, $\alpha = 0.5/d$, $t_d \gg t_a$ (low duty-ratio) and $v = 1.0\,d/t_a^0$.

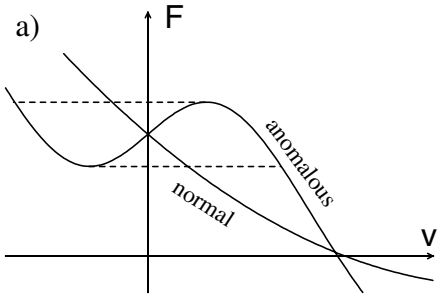

Figure 2.5: Examples of a normal and an anomalous $F - v$ relation, leading to oscillating behaviour.

2.3 Normal and anomalous force-velocity-relations

For a harmonic potential $U(\xi)$ and a strain-independent detachment rate ($t_a(\xi) \equiv t_a$) one always gets a linear force-velocity relation

$$\frac{F}{N} = \frac{t_a k(d - vt_a)}{t_a + t_d}\ . \tag{2.7}$$

It neither depends on the amplitude of thermal fluctuations nor on the distance between the binding sites.

More complex functions $t_a(\xi)$ of course lead to other forms of force-velocity relations. They can be classified into two groups: the normal ones with a monotonously decreasing force for an increasing velocity and the anomalous ones, showing hysteretic behaviour (Fig. 2.5). The reason why anomalous relations are

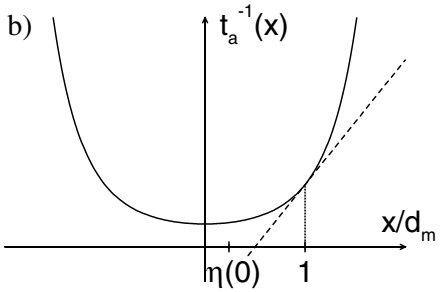

Figure 2.6: A graphical representation of the criterion for the occurrence of oscillations. If the tangent to the detachment rate as a function of x/d_m in the point 1 crosses the x-axis right of the point given by the duty ratio at zero velocity $\eta(0)$, the force-velocity relation is anomalous with a hysteresis around $v = 0$.

interesting is that they allow two different velocities for the same external force. For instance, in a harmonic external potential this leads to spontaneous oscillations if the hysteresis spreads over $v = 0$. Such oscillations were first proposed in a two state ratchet model by Jülicher and Prost [84, 81]. Here we show how such a mechanism can be implemented in a cross-bridge model.

Upon neglecting the discreteness of the binding sites and thermal fluctuations, a simple *sufficient* algebraic criterion for the occurrence of these oscillations can be derived. The zero velocity point certainly lies in a hysteretic range if the slope of the force-velocity relation is positive there. Due to the simplification mentioned above we set $P(\xi) = \delta(\xi - d)$ in Eq. 2.6 and calculate the derivative

$$\left.\frac{dF}{dv}\right|_{v=0} = Nkt_a(d)\eta(0)\left(-1 + (1-\eta(0))d\,t_a(d)\frac{d}{d\xi}\,t_a^{-1}(\xi)\big|_{\xi=d}\right) . \qquad (2.8)$$

At this point we introduced the *duty ratio* (the fraction of time a motor spends in the attached state) [70] at zero velocity as $\eta(v = 0) = t_a(d)/(t_a(d) + t_d)$. If the value of the derivative given by Eq. 2.8 is positive, the force-velocity relation certainly shows anomalous behaviour. A graphical representation of this criterion is shown in Fig. 2.6.

The force-velocity relation as calculated by now describes the mean force a group of motors produces when moving with a given constant velocity. However, the situation is usually reversed and one is interested in the mean velocity at a constant force. Of course, both situations are equivalent in the limit of large N. But for a finite N the motion actually occurs stepwise. This raises the question, how the motors remember on which limb of the hysteresis they currently move.

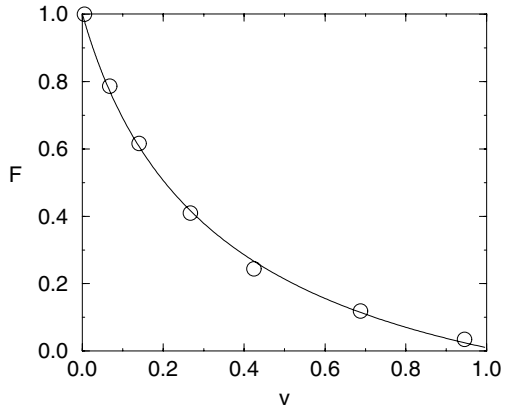

Figure 2.7: The force-velocity relation resulting from (2.5) with $\alpha\, d = 0.55$ and $t_d \gg t_a^0$, compared to Hills data [63]. The scaling on both axes is arbitrary.

The quantity that actually distinguishes between both limbs is the number of currently attached motors. Together with the external force it uniquely defines the velocity. This follows from the fact that the force per attached motor decreases monotonously with increasing velocity (Fig. 2.8), as can be seen from Eq. 2.6. In a finite system the number of motors fluctuates and if it passes a threshold value the velocity jumps from one stable state into the other. The probability for such jumps is highest if the original state is close to the edge of the hysteresis and the number of motors low.

An example of a function always leading to a *normal* $F - v$ relation is $t_a(\xi) = t_a^0 \exp(\alpha\xi)$. It states that the lifetime of the attached state is larger for those heads that have just gone through the power stroke and produce maximum force than for those which have already done their work and now pull backwards. This idea has already been used by A.F. Huxley [73]. Such a dependence is needed for an explanation of the approximately hyperbolic force-velocity dependence in muscle systems. Physiological data by Hill [63] are perfectly fitted within the above analytic results by choosing $\alpha\, d = 0.55$ and $t_d \gg t_a^0$ (Fig. 2.7). Quantised binding sites and thermal fluctuations are found to play only a minor role (neglecting them leads to almost the same curve with $\alpha\, d = 0.58$).

A function that can lead to an *anomalous* $F{-}v$ relation is $t_a(x) \propto \exp(-2\,|\xi|\,/d)$, as shown in Fig. 2.8. For a sufficiently low duty ratio $\eta(0)$ the point $v = 0$ lies within a hysteresis and is unstable if the force is held constant. Instead, a positive finite solution is possible or a negative with $v \to -\infty$. To obtain the latter

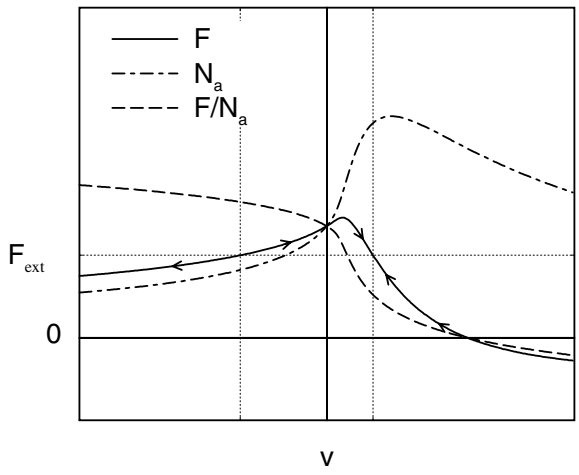

Figure 2.8: An example of the $F - v$ curve for $t_a(\xi) \propto \exp(-2\,|\xi|\,/d)$ and a low duty ratio. The solid line shows the mean force motors would produce at a given velocity. The dashed line shows the mean number of attached motors and the dash-dotted one the mean force per attached motor. Seeking for the velocity at a given force one obtains a stable (higher v) and an unstable (lower v). A third solution is always $v \to -\infty$, but to obtain it one has to include an infinitesimally small friction term.

from our equations, an infinitesimally small friction term has to be added. Now if one lets such a group pull against a harmonic spring with the other end fixed, the extension of the spring oscillates in a sawtooth-like manner with flat ascending slopes (motors working against the spring force) and very steep descending slopes (the spring force pulling motors backwards). Very similar behaviour has been observed in some muscles under specific conditions [181].

2.4 Application to kinesin

So far, our discussion has focused on situations where motors are operating in large groups. There is, however, a second scenario, where only a few molecular motors cooperate at a time, *e.g.* when kinesin transports vesicles along microtubules. Modelling them is guided by the following experimental observations: A kinesin molecule with two heads can move over long distances without detaching from the microtubule [153]. Although it is not yet completely clear how the two kinesin heads "walk" along the protofilaments [17], there are good arguments to

use a model with 8 nm periodicity [69] where each binding site can be occupied only with one head at a time. Single headed kinesin can move microtubules if cooperating in larger groups [58, 59], but not as fast as double-headed [165]. The velocity decreases with increasing load almost linearly [153, 117]. The stall force depends slightly on the ATP concentration [172]. Above the stall force kinesin shows back-and-forth movement, but does not walk backwards [30]. Forward loads can increase the velocity many times [30]. The variance of the trajectory at high ATP concentrations is only about half as large as for a Poisson stepper, indicating that there must be at least two stochastic processes underlying each kinesin step and that the steps are tightly coupled to the ATP hydrolysis cycle [172]. This remains valid even at loads of up to 4 pN (2/3 of the stall force).

From the fluctuation analysis [154, 143, 172] it is quite certain that both the process of attachment and of detachment include an asymmetry between the forward and the backward direction (a new head attaches in front of the other one and the rear head detaches more probably than the front one). The low variance[1] ($r \approx 0.5$) is not *a priori* inconsistent with a model where only one of both asymmetries is present (one where steps with 8 nm and 0 nm occur with equal probabilities), but then everything else in the duty cycle including the dwell times would have to be completely deterministic, which does not seem realistic. The behaviour at superstall forces [30] additionally implies that one of these both asymmetries remains over the whole force range, while the other one reverses at higher forces. In our calculation we restrict ourselves to a model in which the attachment asymmetry gets reversed with increasing load while the detachment asymmetry remains. This approach has already been used by Peskin and Oster [132] and in a similar way by Duke and Leibler [41]. This, however, does not mean that we consider the other case less realistic.

The central quantity of interest is again the force-velocity relation. Because the velocity is not temporally constant as for $N \to \infty$, it has to be calculated directly from transition rates for a constant force. Since an attachment two sites away from the other head is very unprobable, we take only the attachment rate at the front (f) or rear (r) side of the other head into account: $R_a^{f/r} =$

[1] An important feature of the stochastic trajectory is the variance of displacement [154, 143, 172]. The quantity $r = \frac{d}{dt}\langle(x(t) - \langle x(t)\rangle)^2\rangle / \langle v\rangle a$ is a measure for the randomness of the movement. Its value is 1 for a Poisson stepper and 0 for a deterministic process. A two-state model can reach a minimum of $r = 0.5$. The parameters used above lead to $r = 0.62$ at zero load, which is not far from the experimental value $r = 0.52 \pm 0.2$ [154, 143].

$\mathcal{N}\exp[\pm\beta ka(d-F/k)/2]$; $\mathcal{N}$ is chosen such that both rates add up to t_d^{-1}. The respective detachment rates are $R_d^{f/r} = t_a^{-1}((\pm a + F/k)/2)$. The average velocity can then be calculated as the step size a, divided by the average cycle time and multiplied by the difference between the probabilities for a step forwards and for a step backwards

$$v(F) = \frac{a/2}{t_d + 1/(R_d^f + R_d^r)} \left(\frac{R_d^r - R_d^f}{R_d^r + R_d^f} + \frac{R_a^f - R_a^r}{R_a^f + R_a^r} \right) . \tag{2.9}$$

The linear force-velocity curve has led some authors [17, 153] to the conclusion that there is no strain-dependence of the detachment rates. This conclusion, however, is only valid in a model with continuous binding sites [99]. Taking into account discrete binding sites actually leads to a nonlinear, S-shaped curve if the detachment rates are strain-independent. Again the simplest choice is $t_a(\xi) = \exp(\alpha\xi)$. Using a reasonable set of parameters the model is able to reproduce the nearly linear dependence reported in Refs. [153, 117] (Fig. 2.9) with extensions similar to those in Ref. [30]. Fig. 2.9 further shows the velocity for a large number of coupled double-headed and single-headed kinesin molecules. When comparing them to experiments care has to be taken since the pairs are in reality coupled elastically to the backbone, which leads to lower velocities. Beside that both curves depend very sensitively on the choice of $t_a(\xi)$. Nevertheless, they show clearly that the "repulsion" between heads already causes a significant velocity difference between single- and double-headed kinesin.

Another quantity of interest is the probability for the whole molecule detaching from the microtubule during one step is $P_L = t_d/t_a(F/k)$, yielding 5% at zero load and saturating ATP concentration, somewhat higher than comparable observations (1.3%) [165].

In summary, we have shown that a generalised two-state cross-bridge model for molecular motors can lead to a much larger variety of phenomena than previously discussed. We have found analytical results in two limiting cases: for a large number of rigidly coupled motors and for one pair. In the first case we show how different functions describing the strain-dependence of the detachment rate result in linear, hyperbolic or even anomalous force-velocity relations and give a simple algebraic criterion for the latter. Discrete binding sites play only a minor role. For one pair of motors force-velocity-relations as measured on kinesin can be reproduced. They depend crucially on the displacement between the binding sites. The model also shows a significant difference between single- and double-

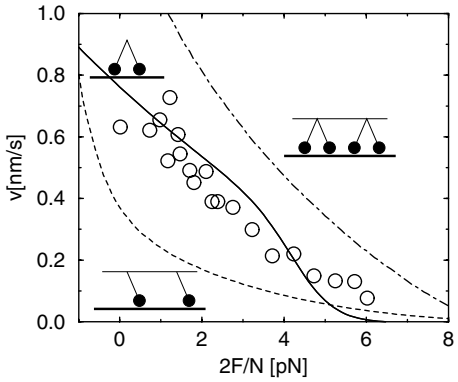

Figure 2.9: Force-velocity curves for kinesin. Experimental data from Ref. [153] at saturating ATP concentration and the theoretical curve for $\alpha = 0.5\,\mathrm{nm}^{-1}$, $t_d = 3\,\mathrm{ms}$, $t_a^0 = 700\,\mathrm{ms}$, $d = 4\,\mathrm{nm}$ and $k = 1.1\,\mathrm{pN/nm}$. The middle curve shows the result for one double-headed molecule, the upper one for many coupled double-headed molecules and the lower one for many single-headed molecules. These two curves were obtained from a Monte-Carlo simulation since the assumptions leading to Eq. (2.3) are not valid any more.

headed kinesin when operating in large groups.

Chapter 3

Elastic coupling

3.1 Introduction

Except for the work by Csahók et al. [32], which discusses the transport of elastically coupled particles driven by coloured noise, and some recent computer simulations on muscle models [33], all the existing models for cooperative molecular motors deal with motors placed on a rigid backbone, interacting with a rigid track. The assumption of stiff filaments seems to be appropriate under physiological conditions in muscles, since the measured extensions of few nanometers [79, 174, 62] are sufficiently small compared to the myosin step-size, which is about 10 nm [48]. However, it certainly can become invalid in gliding assays of the type discussed in Refs. [162, 141] if an actin filament glides over widely separated linearly placed motors. If the spacing between motors is large enough, the elasticity of the backbone or track section between two motors can become comparable to the elasticity of a single motor head. Experiments with myosin molecules bound to an elastic background are conceivable as well.

In this Chapter, which is a somewhat extended revision of Ref. [170], we investigate qualitatively and quantitatively the influence of filament elasticity on the operation of myosin-like motors. Our major quantity of interest is again the force-velocity-relation (filament velocity as a function of the external load). We want to identify the universal effects of filament elasticity and at the same time keep the model as close as possible to experiments. The elasticity modelled by linear harmonic springs may either originate from the flexible backbone or from the flexible track (Fig. 3.1). As long as we are dealing with small relative elongations, both sources of flexibility are equivalent and our model should apply

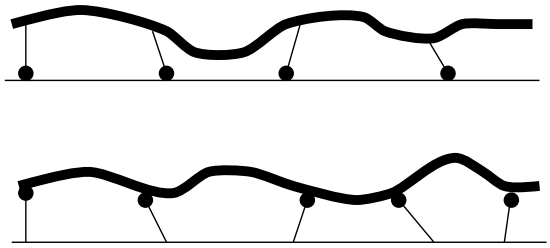

Figure 3.1: Two possible sources of elastic coupling of collective molecular motors: elastic backbone (upper figure) and elastic track (lower figure). Except for very soft backbones/tracks, the description of both models is equivalent.

to both cases. For specificity we use a formulation with an elastic backbone and a stiff track.

3.2 Definition of the model

We consider the one-dimensional model described in Chapter 2. In order to concentrate on the effects of the elastic backbone, we introduce some simplifications. So we neglect thermal fluctuations and the discreteness of binding sites on the track. Besides simplicity, this approximation is also motivated by the finding that discrete binding sites (with a spacing of 5.5 nm) and thermal fluctuations only have a minor effect on the resulting force-velocity-relation. In the following we also assume constant (strain-independent) attachment and detachment times t_a and t_d. A discussion of strain-dependent reaction rates will follow later in Section 3.6.

Again, each attached motor is described as a harmonic spring connecting its root at the backbone (position y) and its head on the track (position x). The force this motor produces between the track and the backbone is given as $k(x-y)$, with a spring constant k. Since the motor is in a forward leaning position before attachment (see Fig. 3.2), it attaches to the track at the point x^n, which is the position y of the root of the motor before attachment, shifted by the displacement d ("power stroke")

$$x^n = y + d \,. \tag{3.1}$$

While assuming a stiff track, we model the backbone as a linear spring with compliance γ^{-1} per unit length. But note that this is merely a convention. Our

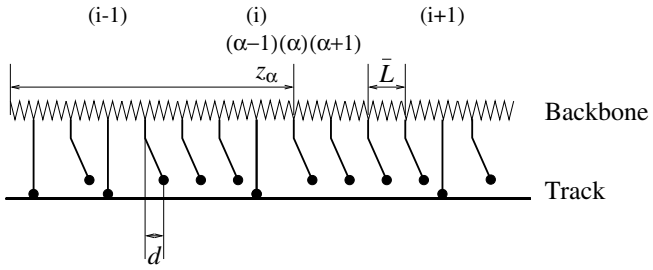

Figure 3.2: Definition of the model. Motors are fixed on the elastic backbone at uniform spacing $\bar{L}$ and attach to the stiff track. z_α denotes the position of α-th motor on the unstrained backbone. Due to the conformational change, the head of each motor attaches at the distance d from its root.

results apply equally well to the reverse situation, where the molecular motors are fixed on a (rigid) cover slip and the elasticity is due to the molecular track transported by them. We consider $\bar{N}$ motors placed on the backbone at uniform spacing $\bar{L}$, so that the total backbone length is $\bar{N}\bar{L}$. The assumption of uniform spacing is made solely for simplicity. Any other distribution which is homogeneous on length scales L would lead to the same exponential distribution of gap widths (see Eq. 3.3 below). The position of the α-th motor on the unstrained backbone will be referred to as z_α. In the following, the actual positions of motor heads $x_\alpha(t)$ and of motor roots $y_\alpha(t)$ are measured relative to z_α (Fig. 3.3).

Instead of using the quantities $\bar{N}$ and $\bar{L}$ it will prove helpful to use the mean number of attached motors $N = \bar{N}t_a/(t_a + t_d)$ and the mean spacing between two attached motors $L = \bar{L}(t_a + t_d)/t_a$. Since for now we are dealing with strain-independent reaction rates the distribution of attached and detached states does not depend on the motion of their positions. The probability of finding a gap with α detached motors between two attached ones is given by the geometric distribution

$$p_\alpha = \left(\frac{t_d}{t_a + t_d}\right)^\alpha \frac{t_a}{t_a + t_d} \,. \tag{3.2}$$

In order to keep the model as lucid as possible we assume a small duty ratio [70], meaning that a motor molecule spends most of its time in the detached state, $t_a \ll t_d$. Since we are dealing with nonprocessive motors ("rowers" [99]), this assumption is certainly valid. While keeping the mean number N of attached motors and their average spacing L constant, we consider the limit $\bar{L} \to 0$. With

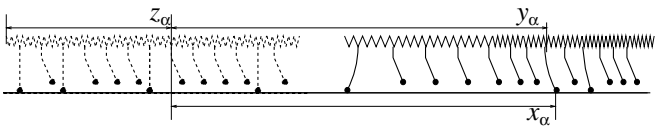

Figure 3.3: The moving backbone (solid line) and its initial position at time $t = 0$ (dashed line). y_α denotes the root position of the α-th motor, relative to its initial value (z_α). x_α denotes the head position of the α-th motor, also relative to the initial position of the α-th root, z_α.

this simplification the model becomes continuous. Also, the assumption about equidistantly placed motors on the backbone becomes superfluous in this limit. The distribution of motors is insignificant as long as it is sufficiently homogeneous on the length scale L. The attachment rate per length L (between the positions z and $z + L$ on the backbone) obeys $r_a = L/\bar{L}t_d = 1/t_a$. The distribution of gap widths (3.2) takes the form of an exponential distribution

$$p(l) = \frac{1}{L} e^{-l/L} \, . \tag{3.3}$$

3.3 Results

In this Section we summarise our main results for the analysis of the model described above (infinite size, constant reaction rates). The details of the analytical calculation are given later in Sec. 3.4.

As described by now the model contains seven independent parameters: t_a, N, L, F, k, γ and d. Upon measuring the force per motor, F/N, in units of the force during one power stroke, kd, and measuring the backbone elasticity per unit length, γ/L, in units of the motor head elasticity, they may be reduced to two adimensional parameters: $\hat{F} = F/Nkd$ and $\hat{\gamma} = \gamma/kL$. Then the velocity in units of a single motor velocity $\hat{v} = vt_a/d$ is given by a "scaling" function $\hat{v} = \eta(\hat{F}, \hat{\gamma})$.

As shown in Sec. 3.4 we find that in case of a time-independent external force it does not matter whether this force pulls on one end or homogeneously on the whole backbone with a density $f = F/NL$. A quite remarkable result of our analysis is that the force-velocity relation remains linear for flexible backbones and that the zero load velocity d/t_a does not depend on the backbone elasticity. The force-velocity relations for a stiff and an elastic backbone are shown in Fig. 3.4.

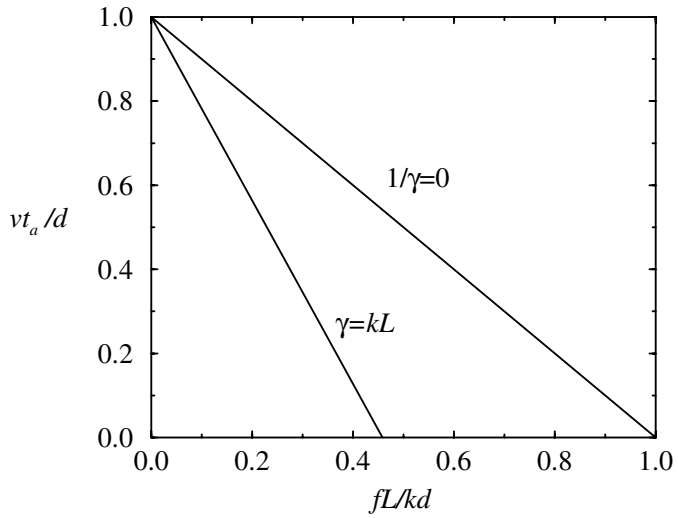

Figure 3.4: Force-velocity-relation for the stiff ($\gamma = \infty$) and elastic ($\gamma = kL$) backbone.

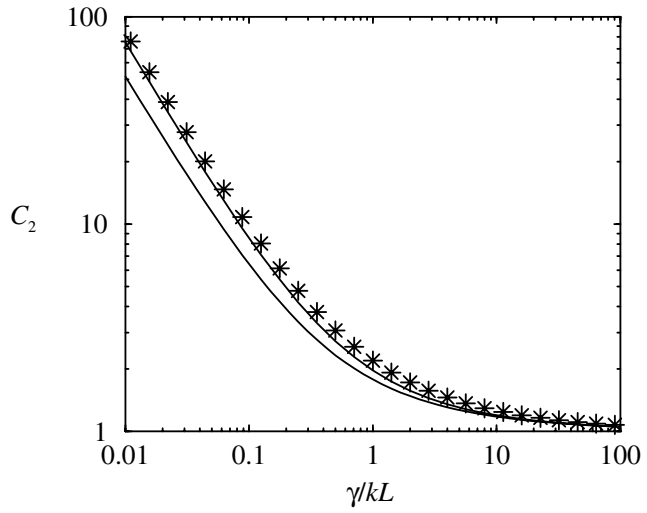

Figure 3.5: The slope of the force-velocity relation (coefficient C_2 in Eq. (3.19)), as a function of the relative backbone stiffness γ/kL: computer simulation (stars), analytic approximation without correlations (lower curve), with correlations to the distances to nearest neighbours (upper curve). In both analytic curves the numerical result for $k\langle 1/K_e\rangle$ from Fig. 3.8 was used.

γ/kL	C_2
0.001	828
0.01	84.3
0.1	9.81
1	2.20
10	1.26
100	1.075
1000	1.023

Table 3.1: Numerical values of the coefficient C_2, giving the slope of the force-velocity relation. Data were obtained from a simulation with the average number of motors $N = 500$ and periodic boundary conditions. Each value results from 4×10^8 simulation steps (preceded by an initiation run with 1×10^8 steps).

If the relative backbone stiffness $\hat{\gamma}$ lies below 1, the slope of the force-velocity curve and consequently the stall force differ significantly from those for a stiff backbone (Fig. 3.5). While the stall force f_{stall} is proportional to the motor stiffness ($f_{\text{stall}} = kd/L$) for stiff backbones, it becomes a function of backbone stiffness for very flexible backbones and is given as $2\gamma d/\nu L^2$. Here ν is a numerical constant which has the value $\nu \approx 1.64$ as obtained from the computer simulation. Using analytical tools based on a Master-Equation approach with correlations between the position of a motor and the distances to its neighbours, we obtain the value $\nu \approx 1.50$, which is in good agreement. For completeness Fig. 3.5 also shows the result of a Master-Equation without correlations, yielding $\nu = 1$. Some numerical values of the coefficient C_2 are given in Table 3.1.

Due to the generic features of our two-state model one expects that the effects we have discussed here should as well apply to other models which contain the same basic mechanisms of force generation, e.g. [99, 81]. However, models of the type discussed in Ref. [32], which describe particles in an asymmetric periodic potential subject to a temporally correlated noise, are based on a thoroughly different driving mechanism. Therefore, one expects and actually finds a variety of disparate effects including a strong influence of the coupling strength on the velocity even without external load.

3.4 Analytical solution

In this Section the calculation leading to the force-velocity-relation for strain-independent detachment rates and without considering finite-size effects is given. This is done in several steps: first we show that the model behaves equivalently if a force acts on one end of the filament or homogeneously along the whole length. As second we calculate the effective compliance of a semi-infinite chain, which is an important input quantity for later use. Then we show the linearity of the force-velocity-relation, show that the zero-load velocity does not differ from its value for stiff backbones and finally calculate its slope in two different approximations.

A generic situation found in many experimental setups is that a force F, usually produced by an optical tweezer, acts on the rear end of the backbone. Another possibility is to produce the force by a viscous liquid, flowing along the backbone. Such a force acts more or less homogeneously on the whole backbone. In both cases the main quantity of interest is the resulting mean backbone velocity depending on the load F. In the following we show that both situations are equivalent within the scope of a theoretical description.

3.4.1 Point force

From now on we use the index i, which runs over attached motors only, instead of the index α, running over all motors. x_i and y_i denote the head and root positions of i-th attached motor relative to its initial position on the unstrained backbone (z_i) at time $t = 0$. The stiffness of the backbone fragment between the motors i and $i+1$ equals $\gamma/(z_{i+1} - z_i)$. At the point where the i-th motor is fixed to the backbone, the sum of all three forces (from the motor, from the left part of the backbone and from the right part of the backbone) must be zero:

$$k(x_i - y_i) - \gamma\frac{y_i - y_{i-1}}{z_i - z_{i-1}} + \gamma\frac{y_{i+1} - y_i}{z_{i+1} - z_i} = 0\,, \tag{3.4a}$$

$$k(x_1 - y_1) + \gamma\frac{y_2 - y_1}{z_2 - z_1} = F\,. \tag{3.4b}$$

The second equation describes the first attached motor and differs from the others since the backbone force acting from the left is replaced by the external force F. With given x_i and z_i this set of equations allows us to determine the values of y_i.

The *detachment* rate equals t_a^{-1} for each motor. The detachment of one motor is described by cancelling its position in the set of x- and z-values. Afterwards, all the y-values are determined anew from Eq. (3.4).

The process of *attachment* occurs at the rate N/t_a and consists of choosing a random position z^n between 0 and NL, calculating the corresponding $y(z^n)$ (the root position of the new motor before attaching) and $x^n = y(z^n) + d$, and finally adding a new motor with its head at x^n and its root at z^n. Again, all the y-values have to be recalculated as stated by Eq. (3.4). Expressing $y(z^n)$ through the positions of the neighbours (the index "−" describes the first attached motor on the left and "+" on the right hand side) yields

$$x^n = y^n + d = \frac{y_-(z_+ - z^n) + y_+(z^n - z_-)}{z_+ - z_-} + d \; . \tag{3.5}$$

3.4.2 Equivalence to the model with a homogeneous force

In the model described by now, the external force acts on one end of the backbone. This leads to some difficulties, e.g. one can only consider a semi-infinite chain with one boundary condition. Furthermore, the resulting solutions are not translationally invariant since the strain decreases along the backbone.

Replacing the point force by a homogeneous one acting on the whole backbone with a density $f = dF/dz$ would allow us to perform the calculation on an infinite chain of completely equivalent motors. The ability to use periodic boundary conditions in the computer simulation would be an additional advantage.

Fortunately, both models, i.e. with a point force and a homogeneous force are actually equivalent. It is instructive to show this equivalence in the continuum formulation of the model. Instead of the discrete set of variables y_i^P we use a function $y^P(z)$. The continuum representation of Eqn. (3.4)) is given by the following set of equations

$$\gamma \frac{d^2 y^P}{dz^2} = -\sum_i \delta(z - z_i) k(x_i^P - y^P(z_i)) \; , \tag{3.6a}$$

$$\gamma \left. \frac{dy^P}{dz} \right|_{z=0} = F \; . \tag{3.6b}$$

The first equation expresses the constant tension between the attached motors with jumps at the positions where the motor roots are placed. The second equation describes the strain at the boundary of the backbone.

On the other hand, in the homogeneous force model the strain grows linearly with z

$$\gamma \frac{d^2 y^H}{dz^2} = f - \sum_i \delta(z - z_i) k(x_i^H - y^H(z_i)) \; . \tag{3.7}$$

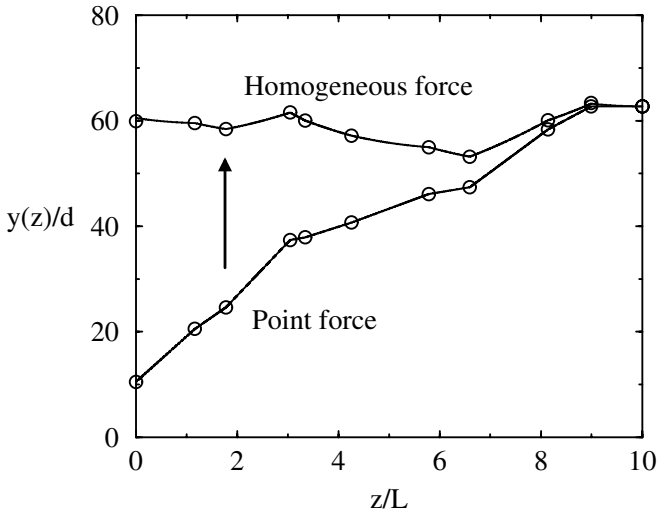

Figure 3.6: Transformation from the model with a point force to the model with a continuous force, given through Eq. (3.8), on a typical configuration during the motion. The circles represent attached motors, the detached ones lie on the line. z denotes the position a motor would have on an unstrained backbone, y its root position relative to z (Fig. 3.3).

Since we are dealing with a force constant in time and with quasistationary solutions, we can show that both models are equivalent up to a transformation which shifts the heads and roots of motors, depending on their z position. As may be easily verified by comparing Eqns. (3.6) and (3.7), the following transformation

$$\left\{ \begin{array}{c} x_i^H \\ y_i^H \end{array} \right\} = \left\{ \begin{array}{c} x_i^P \\ y_i^P \end{array} \right\} + \frac{f}{2\gamma}(NL - z_i)^2 \tag{3.8}$$

with $F = NLf$ preserves the properties of the model. The transformation is shown schematically in Fig. 3.6. After having shown the equivalence of both models, we can return to the original formulation. The transformed equations (3.4) and (3.5) become (in the following we omit the index ^{H})

$$k(x_i - y_i) - \gamma \frac{y_i - y_{i-1}}{z_i - z_{i-1}} + \gamma \frac{y_{i+1} - y_i}{z_{i+1} - z_i} - f \frac{z_{i+1} - z_{i-1}}{2} = 0 \tag{3.9}$$

and

$$x^n = \frac{y_-(z_+ - z^n) + y_+(z^n - z_-)}{z_+ - z_-} + d - \frac{f}{2\gamma}(z_+ - z^n)(z^n - z_-)\ . \tag{3.10}$$

The additional term represents the displacement of a uniformly loaded spring, tightly bound at its ends at z_- and z_+. Of course, these equations also follow directly from (3.7).

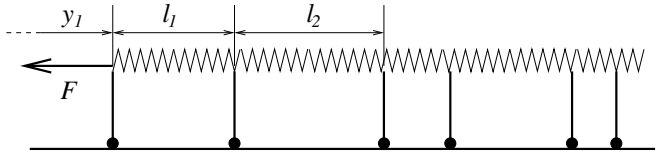

Figure 3.7: Effective spring constant of a semi-infinite chain with randomly distributed displacements between bridges.

3.4.3 Effective compliance of a semi-infinite chain

A quantity frequently needed during the analytical solution of the model described in Sect. 3.2 is the elasticity of a semi-infinite stochastic chain as shown in Figure 3.7. It is defined as

$$\frac{1}{K_e} = -\left.\frac{dy_1}{dF}\right|_{x_i=\text{const}} \tag{3.11}$$

where y_1 is a part of the solution of Eq. (3.4). As defined in Sect. 3.2, the spring constant of the motors is given by k. The values of l_i are distributed randomly with average L and the exponential distribution (3.3).

The compliance of a chain with a given configuration (given l_i-values) can be calculated recursively. The chain is built up of a spring with stiffness k, connected in parallel to two other springs, which themselves are connected in series. The first one describes the piece of backbone with elasticity γ/l_1. The second spring is again a replacement for another semi-infinite chain starting with the second motor. We denote its stiffness as K_e'.

$$K_e = k + \frac{1}{\frac{l_1}{\gamma} + \frac{1}{K_e'}} \tag{3.12}$$

Repeating the same procedure for K_e' etc. and finally averaging over all configurations $(l_1, l_2, \dots)$ with their statistical weights yields

$$\left\langle \frac{1}{K_e} \right\rangle = \int_0^\infty dl_1 p(l_1) \int_0^\infty dl_2 p(l_2) \dots \frac{1}{k + \cfrac{1}{\frac{l_1}{\gamma} + \cfrac{1}{k + \cfrac{1}{\frac{l_2}{\gamma} + \cfrac{1}{k + \frac{1}{\dots}}}}}} \; . \tag{3.13}$$

The convenient way to solve this high-dimensional integral, however, is by using the Monte-Carlo method. Its result is shown in Fig. 3.8.

One possibility to give an analytic approximation for $\langle K_e^{-1} \rangle$ is the use of a mean-field like theory by assuming that all displacements l_i are exactly equal

to their mean value L. Then the above expression becomes self-similar and we obtain the recursion relation

$$\left\langle \frac{1}{K_e} \right\rangle = \frac{1}{k + \frac{1}{\frac{L}{\gamma} + \left\langle \frac{1}{K_e} \right\rangle}} \tag{3.14}$$

with the solution

$$\left\langle \frac{1}{K_e} \right\rangle = \frac{L}{2\gamma} \left(\sqrt{1 + 4\frac{\gamma}{kL}} - 1 \right) . \tag{3.15}$$

In Fig. 3.8 the approximation, Eq. (3.15) is plotted against the (exact) Monte-

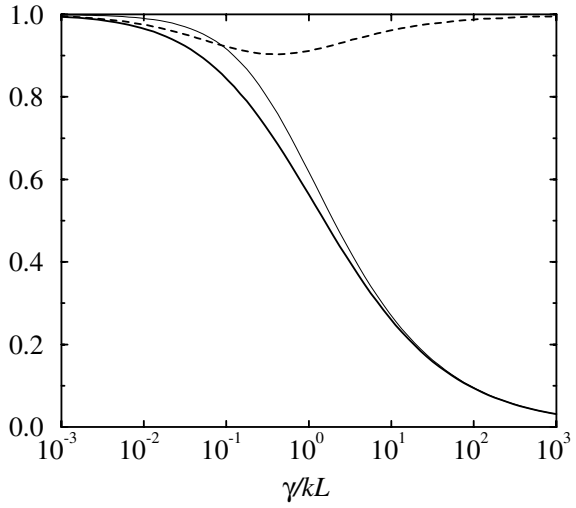

Figure 3.8: The effective compliance of a semi-infinite chain $k\langle 1/K_e \rangle$. Thick line: Monte-Carlo result. Thin line: approximation given by Eq. (3.15). Dashed line: the ratio between the Monte-Carlo result and the approximation.

Carlo solution of (3.13). The deviations lie below 10% over the entire parameter range. The approximation becomes exact for both very soft and very rigid backbones. In the case of large γ this is due to the fact that the long-range coupling makes the detailed distribution of l_i irrelevant. The case of low γ is trivial since the motors get decoupled and the stiffness of the chain is determined solely by the first motor ($\langle K_e^{-1} \rangle = \frac{1}{k}$).

3.4.4 Linearity of the force velocity relation

For rigidly coupled motors it was already shown in [99] that the velocity is linear in the applied force f as well as in the step size d. In the following we present

a simple argument why this remains valid for elastically coupled motors. We denote the number of currently attached motors by n and their positions on the backbone by a vector $\mathbf{x}$ containing the components $x_1 \dots x_n$. From the structure of Eqns. (3.9) and (3.10) it is evident that the process of attachment can be described by the following equation

$$\mathbf{x}^{(i+1)} = A\mathbf{x}^{(i)} + \mathbf{u}_1 \frac{fL}{k} + \mathbf{u}_2 d \tag{3.16}$$

where the $(n+1, n)$-matrix A and the $(n+1)$-vectors $\mathbf{u}_1$ and $\mathbf{u}_2$ depend in a complex way on $\{z_i\}$ and γ/Lk. The detachment of one head is described by another $(n-1, n)$-matrix A as

$$\mathbf{x}^{(i+1)} = A\mathbf{x}^{(\mathbf{i})} \; . \tag{3.17}$$

After a series of consecutive attachments and detachments this gives

$$\mathbf{x}^{(i)} = \tilde{A}\mathbf{x}^{(0)} + \tilde{\mathbf{u}}_1 \frac{fL}{k} + \tilde{\mathbf{u}}_2 d \; . \tag{3.18}$$

Finally we set $\mathbf{x}^{(0)} = 0$ and calculate the mean motor position $\langle x \rangle = \operatorname{tr} \mathbf{x}/n$. Since the time needed for i steps is proportional to t_a, we obtain the relation

$$v = \frac{1}{t_a} \left(C_1 d - C_2 \frac{fL}{k} \right) \; , \tag{3.19}$$

which is linear in d and in f. The constants C_1 and C_2 get independent of the mean number of motors N for $N \to \infty$.

The force-velocity-relations for the elastic and for the stiff backbone are compared in Fig. 3.4. Due to the linearity of the force-velocity relation the problem can be separated in two parts: determining the backbone velocity without external forces ($f = 0$) and the velocity with external force but without power strokes ($d = 0$). The remaining work consists of determining the constants C_1 and C_2.

3.4.5 Master-equation

An adequate description of the model is given by $P(\dots, l_2, l_1; x, t; r_1, r_2, \dots)$, the probability density to find a head at position x and with distances $l_1 \equiv z_i - z_{i-1}$ and $r_1 \equiv z_{i+1} - z_i$ to its nearest attached neighbours, the distances $l_2 \equiv z_{i-1} - z_{i-2}$ and $r_2 \equiv z_{i+2} - z_{i+1}$ between the nearest and the next nearest attached neighbours etc.. Of course, this distribution varies with time. Because the problem is linear

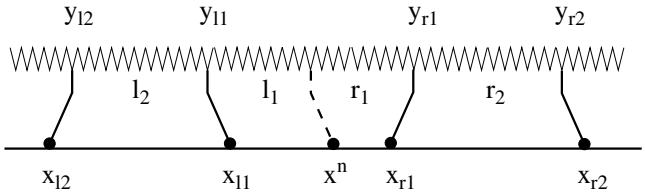

Figure 3.9: Attachment of a new head.

in x and y, there is no need for determining the correlations between the positions of different motor heads on the track. P can be expressed by

$$P(\dots, l_2, l_1; x, t; r_1, r_2, \dots) = P(x,t)_{\dots, l_2, l_1; r_1, r_2, \dots} p(\dots, l_2, l_1; r_1, r_2, \dots) \,. \quad (3.20)$$

The second factor describes the probability for a motor to have the distances l_1, r_1, l_2, r_2, ... to its neighbours. In a steady solution it is given by Eq. (3.3)

$$p(\dots, l_2, l_1; r_1, r_2, \dots) = \frac{e^{-l_1/L}}{L} \frac{e^{-r_1/L}}{L} \frac{e^{-l_2/L}}{L} \dots \quad (3.21)$$

The first factor gives the distribution of the head positions x for the given set of distances. Since the transition rates are constant (strain-independent), the first factor does not influence the second one.

We describe the temporal development of P in terms of a Master equation. The detachment of motors is described as drain, attachment as source. Additional terms result from the fact that the attachment/detachment of a motor also changes the l and r-values in its neighbourhood.

The detachment rate is equal to the probability density divided through the mean life time of the attached state

$$r_d(\dots, l_2, l_1; x, t; r_1, r_2, \dots) = \frac{1}{t_a} P(\dots, l_2, l_1; x, t; r_1, r_2, \dots) \,. \quad (3.22)$$

Once the distribution of z-values ($p(\dots, l_2, l_1; r_1, r_2, \dots)$) is in equilibrium, the attachment and detachment rate integrated over x have to be equal. They can only differ in the x-dependence. Thus we write the attachment rate the same way as the detachment rate except for a different factor containing the distribution of x-positions of the newly attached heads.

$$r_a(\dots, l_2, l_1; x, t; r_1, r_2, \dots) = \frac{1}{t_a} p(\dots, l_2, l_1; r_1, r_2, \dots) P^n(x,t)_{\dots, l_2, l_1; r_1, r_2, \dots} \quad (3.23)$$

The x-distribution of attaching motors depends on the x-distributions of all the neighbours. It is determined as the integral over all (properly weighted) configurations which lead to a motor attachment at position x^n:

$$P^n(x,t)_{\dots,l_2,l_1;r_1,r_2,\dots} = \dots \int dx_{l1} P(x_{l1},t)_{\dots,l_3,l_2;l_1,r_1\dots} \int dx_{r1} P(x_{r1},t)_{\dots,l_1,r_1;r_2,r_3\dots} \dots \\ \delta\left(x^n(\dots,x_{l1},x_{r1},\dots) - x\right) \quad (3.24)$$

As follows form Eq. (3.10), x^n can be expressed through y_{l1} and y_{r1}

$$x^n = \frac{y_{l1}r_1 + y_{r1}l_1}{l_1 + r_1} + d - \frac{f}{2\gamma} lr \;, \quad (3.25)$$

which again are functions of all x_i and can be determined through Eq. (3.9).

The detachment/attachment of one specific site leads to destruction respectively creation of the following states (see also Fig. 3.9):

Detachment

destroyed	created
$(\dots,l_2,l_1;x;r_1,r_2,\dots)$	
$(\dots,l_3,l_2;x_{l1};l_1,r_1,\dots)$	$(\dots,l_3,l_2;x_{l1};l_1+r_1,r_2,\dots)$
$(\dots,l_1,r_1;x_{r1};r_2,r_3,\dots)$	$(\dots,l_2,l_1+r_1;x_{r1};r_2,r_3,\dots)$
$\vdots$	$\vdots$

Attachment

destroyed	created
	$(\dots,l_2,l_1;x^n;r_1,r_2,\dots)$
$(\dots,l_3,l_2;x_{l1};l_1+r_1,r_2,\dots)$	$(\dots,l_3,l_2;x_{l1};l_1,r_1,\dots)$
$(\dots,l_2,l_1+r_1;x_{r1};r_2,r_3,\dots)$	$(\dots,l_1,r_1;x_{r1};r_2,r_3,\dots)$
$\vdots$	$\vdots$

The Master equation for P, using the transition rates (3.22, 3.23) finally reads

$$
\begin{aligned}
&\frac{d}{dt}P(\xi,t)_{\dots,\lambda_2,\lambda_1;\rho_1,\rho_2,\dots}p(\dots,\lambda_1;\rho_1,\dots) = \int dx \int dl_1 \int dr_1 \dots \\
&\Big[\quad r_d(\dots,l_2,l_1;x,t;r_1,r_2,\dots)\Big(-\delta(\xi-x)\,(\cdots\delta(\lambda_1-l_1)\delta(\rho_1-r_1)\cdots) \\
&\quad +P(x,t)_{\dots,l_3,l_2;l_1,r_1\dots}(-\cdots\delta(\lambda_2-l_3)\delta(\lambda_1-l_2)\delta(\rho_1-l_1)\cdots \\
&\qquad +\cdots\delta(\lambda_2-l_3)\delta(\lambda_1-l_2)\delta(\rho_1-(l_1+r_1))\delta(\rho_2-r_2)\cdots) \\
&\quad +P(x,t)_{\dots,l_1,r_1;r_2,r_3\dots}(-\cdots\delta(\lambda_2-l_1)\delta(\lambda_1-r_1)\delta(\rho_1-r_2)\cdots \\
&\qquad +\cdots\delta(\lambda_2-l_2)\delta(\lambda_1-(l_1+r_1))\delta(\rho_1-r_2)\delta(\rho_2-r_3)\cdots) \\
&\quad \vdots \\
&\quad \Big) \\
&\quad +r_a(\dots,l_2,l_1;x,t;r_1,r_2,\dots)\Big(\delta(\xi-x)\,(\cdots\delta(\lambda_1-l_1)\delta(\rho_1-r_1)\cdots) \\
&\quad +P(x,t)_{\dots,l_3,l_2;l_1+r_1,r_2\dots}(-\cdots\delta(\lambda_1-l_2)\delta(\rho_1-(l_1+r_1))\delta(\rho_2-r_2)\cdots \\
&\qquad +\cdots\delta(\lambda_1-l_2)\delta(\rho_1-l_1)\delta(\rho_2-r_1)\cdots) \\
&\quad +P(x,t)_{\dots,l_2,l_1+r_1;r_2,r_3\dots}(-\cdots\delta(\lambda_2-l_2)\delta(\lambda_1-(l_1+r_1))\delta(\rho_1-r_2)\cdots \\
&\qquad +\cdots\delta(\lambda_2-l_1)\delta(\lambda_1-r_1)\delta(\rho_1-r_2)\cdots) \\
&\quad \vdots \\
&\quad \Big)\Big]
\end{aligned}
\tag{3.26}
$$

Rather than in the distribution itself we are interested in the expectation value $\langle x(t)\rangle_{\dots,l_2,l_1;r_1,r_2,\dots}$. Its equation of motion follows directly form the Master equation.

$$
\begin{aligned}
&\frac{d}{dt}\langle x(t)\rangle_{\dots,\lambda_2,\lambda_1;\rho_1,\rho_2,\dots}p(\dots,\lambda_1;\rho_1,\dots) = \\
&\quad \frac{1}{t_a}\int dl_1 \int dr_1 \dots p(\dots,l_2,l_1;r_1,r_2,\dots)\Big[\\
&\quad -\langle x(t)\rangle_{\dots,l_2,l_1;r_1,r_2,\dots}\delta(\xi-x)\,(\cdots\delta(\lambda_1-l_1)\delta(\rho_1-r_1)\cdots) \\
&\quad +\langle x(t)\rangle_{\dots,l_3,l_2;l_1,r_1\dots}(-\cdots\delta(\lambda_2-l_3)\delta(\lambda_1-l_2)\delta(\rho_1-l_1)\cdots \\
&\qquad +\cdots\delta(\lambda_2-l_3)\delta(\lambda_1-l_2)\delta(\rho_1-(l_1+r_1))\delta(\rho_2-r_2)\cdots) \\
&\quad +\langle x(t)\rangle_{\dots,l_1,r_1;r_2,r_3\dots}(-\cdots\delta(\lambda_2-l_1)\delta(\lambda_1-r_1)\delta(\rho_1-r_2)\cdots \\
&\qquad +\cdots\delta(\lambda_2-l_2)\delta(\lambda_1-(l_1+r_1))\delta(\rho_1-r_2)\delta(\rho_2-r_3)\cdots) \\
&\quad \vdots
\end{aligned}
$$

$$
\begin{aligned}
&+ \langle x^n(t)\rangle_{\dots,l_2,l_1;r_1,r_2,\dots}\delta(\xi - x)\,(\cdots\delta(\lambda_1 - l_1)\delta(\rho_1 - r_1)\cdots) \\
&+ \langle x(t)\rangle_{\dots,l_3,l_2;l_1+r_1,r_2\dots}(-\cdots\delta(\lambda_1 - l_2)\delta(\rho_1 - (l_1 + r_1))\delta(\rho_2 - r_2)\cdots \\
&\qquad + \cdots\delta(\lambda_1 - l_2)\delta(\rho_1 - l_1)\delta(\rho_2 - r_1)\cdots) \\
&+ \langle x(t)\rangle_{\dots,l_2,l_1+r_1;r_2,r_3\dots}(-\cdots\delta(\lambda_2 - l_2)\delta(\lambda_1 - (l_1 + r_1))\delta(\rho_1 - r_2)\cdots \\
&\qquad + \cdots\delta(\lambda_2 - l_1)\delta(\lambda_1 - r_1)\delta(\rho_1 - r_2)\cdots) \\
&\vdots \\
&\Big] \qquad (3.27)
\end{aligned}
$$

This equation simplifies further if the distances l_i and r_i are distributed according to their equilibrium distribution (3.21), which is certainly the case after the motors have been running for some time.

Usually one is looking for the quasistationary solution with

$$\frac{d}{dt}\langle x(t)\rangle_{\dots,\lambda_2,\lambda_1;\rho_1,\rho_2,\dots} = v\ .$$

3.4.6 Zero load backbone velocity

In the special case of zero external load ($f = 0$) one can see that as long as the expectation value $\langle x\rangle_{\dots,l_2,l_1;r_1,r_2,\dots}$ is independent of the distances l_i and r_i, i.e.

$$\int dx\, x\, P(x,t)_{\dots,l_2,l_1;r_1,r_2,\dots} = \langle x\rangle\ , \qquad (3.28)$$

the same holds for y_i (determined from (3.9)) and for x^n, which follows from Eq. (3.25)

$$\langle x^n\rangle = \langle y\rangle + d = \langle x\rangle + d\ . \qquad (3.29)$$

In other words, if the average head position of the existing attached motors is not correlated to the distances between them, the position where the head of a new motor attaches is uncorrelated too. Thus we have shown self-consistently that $\langle x\rangle_{\dots,l_2,l_1;r_1,r_2,\dots}$ does not depend on l_i and r_i. The equation of motion (3.27) for the expectation value of x simplifies to

$$v \equiv \frac{d}{dt}\langle x\rangle = \frac{1}{t_a}\left(\langle x^n\rangle - \langle x\rangle\right) = \frac{d}{t_a}\ . \qquad (3.30)$$

This means

$$C_1 = 1 \qquad (3.31)$$

for the first coefficient in Eq. (3.19). The interesting point in this result is that it is independent of the backbone elasticity. As long as there is no external force, the velocity remains the same as in the case of a rigid backbone, this is $v(f = 0) = d/t_a$. This argument also applies for a finite system, it only has to be large enough in order that the situation in which all motors are detached at the same time does not to occur.

3.4.7 Slope of the force-velocity curve (correlations neglected)

In the previous section we have shown that in the case of zero external force the average x-position of a motor stays uncorrelated to the distances to its attached neighbours, which made the calculation of the force-velocity relation pretty easy. In the case of nonvanishing external forces (behaviour described by the coefficient C_2 in Eq. 3.19), the correlation doesn't vanish any more. However, as a first approximation we may still try to neglect it. Later we will take correlations with distances to the nearest neighbours into account and show that they improve the result significantly.

The solution is analogue to the previous section, except that we set $d = 0$ and $f \neq 0$ in Eq. (3.25). Another difference is that the average y-value differs from the average x-value by the mean force per attached motor (fL), divided through the motor stiffness k

$$\langle y \rangle = \langle x \rangle - \frac{fL}{k} \, . \tag{3.32}$$

Instead of this rather intuitive argument this equation can also be derived directly from Eq. (3.9) by summation over i.

This equation describes the y-position, averaged over all motors. However, the quantities needed in Eq. (3.25) are the expectation values of y_{r1} and y_{l1} (motors at the edge of a gap whose distance to one neighbour is $l_1 + r_1$ and to the other neighbour randomly distributed). Even with uncorrelated x-values the expectation values $\langle y_{l1} \rangle$ and $\langle y_{r1} \rangle$ are not the same as $\langle y \rangle$.

For a gap width equal to the mean distance between attached motors both quantities will not differ. Otherwise the average value of the y-positions beneath a gap of width $l_1 + r_1$ differ from $\langle y \rangle$ by the excess force acting on the gap between them ($f(l_1 + r_1)$) compared to the force on the average gap (fL), multiplied by

the effective compliance of a semi-infinite chain (Sect. 3.4.3)

$$\langle y_{l1}\rangle = \langle y_{r1}\rangle = \langle y\rangle - f\left\langle \frac{1}{K_e}\right\rangle \frac{l_1 + r_1 - L}{2} \tag{3.33}$$

The denominator 2 describes the fact that the force is distributed equally to both edges.

The mean x-position of the newly attached motor follows by combining Eqns. (3.25), (3.32), and (3.33):

$$\langle x^n\rangle_{l_1;r_1} = \langle x\rangle - f\left(\left\langle \frac{1}{K_e}\right\rangle \frac{l_1 + r_1 - L}{2} + \frac{L}{k} + \frac{l_1 r_1}{2\gamma}\right) \tag{3.34}$$

Since we want to neglect correlations between $\langle x\rangle$ and (l_i, r_i), we average over l_1 and r_1 ($\langle l_1\rangle = \langle r_1\rangle = L$)

$$\langle x^n\rangle = \langle x\rangle - f\left(\left\langle \frac{1}{K_e}\right\rangle \frac{L}{2} + \frac{L}{k} + \frac{L^2}{2\gamma}\right) . \tag{3.35}$$

In analogy to the previous subsection the final result for the dimensionless coefficient C_2 is

$$C_2 = \left(\frac{k}{2}\left\langle \frac{1}{K_e}\right\rangle + 1 + \frac{kL}{2\gamma}\right) . \tag{3.36}$$

The result is shown in Figure 3.5. In the limit of very soft backbones ($\gamma \ll kL$) the stall force (3.19)

$$f_{\text{stall}} = \frac{dk}{LC_2} \tag{3.37}$$

becomes $f_{\text{stall}} = 2d\gamma/L^2$, which is independent of the motor stiffness k. Our computer simulations show this behaviour, however with a different prefactor, resulting from the correlations which were neglected in this approximation:

$$f_{\text{stall}} \approx \frac{2d\gamma}{\nu L^2} \tag{3.38}$$

with $\nu \approx 1.64$.

In the limit of stiff backbones ($\gamma \gg kL$), we obtain using (3.15)

$$f_{\text{stall}} \approx dk\left(1 - \frac{1}{2}\sqrt{\frac{kL}{\gamma}}\right) . \tag{3.39}$$

3.4.8 First-order correlations

Contrary to the previous subsection where we neglected the correlation between the position x of a motor and the distances to its neighbours by using the ansatz (3.28), we now extend the calculation by taking correlation with distances to nearest neighbours into account. We replace the approximation (3.28) by introducing a function describing these correlations

$$\int dx\, x\, P(x,t)_{\dots,l_2,l_1;r_1,r_2,\dots} = \langle x(t)\rangle - \frac{fL}{k}\mu\left(\frac{l_1}{L};\frac{r_1}{L}\right) . \tag{3.40}$$

The function μ is scale invariant. It has to fulfil the condition

$$\int dl_1 \int dr_1 p(l_1;r_1)\mu\left(\frac{l_1}{L};\frac{r_1}{L}\right) = 0 . \tag{3.41}$$

This also means that the head positions of the motors limiting a gap of width $l_1 + r_1$ already differ from $\langle x\rangle$

$$\langle x\rangle_{l_1+r_1;} = \langle x\rangle - \frac{fL}{k}\int_0^\infty dr_2\, p(r_2)\mu\left(\frac{l_1+r_1}{L};\frac{r_2}{L}\right) \tag{3.42}$$

The equation (3.33) has to be extended by a term describing this influence. Since the roots of the motors are connected to their heads via elastic constants k and to the rest of the track via effective constants $K_e - k$, the correction in y corresponds to the x-correction attenuated by the factor k/K_e. Finally, the refined Eq. (3.34) reads

$$\langle x^n\rangle_{l_1;r_1} = \langle x\rangle - f\left(\left\langle\frac{1}{K_e}\right\rangle\frac{l_1+r_1-L}{2} + \frac{L}{k} + \frac{l_1 r_1}{2\gamma}\right) + k\left\langle\frac{1}{K_e}\right\rangle\left(\langle x\rangle_{l_1+r_1;} - \langle x\rangle\right) . \tag{3.43}$$

The correlation to farther neighbours is still neglected. This is expressed in the simplified equation of motion which is obtained by integrating both sides of (3.27) over all $\lambda_{i\geq 2}$ and $\rho_{i\geq 2}$

$$\begin{aligned}
&\frac{d}{dt}\langle x(t)\rangle\, p(\lambda_1;\rho_1) = \frac{1}{t_a}\int dl_1 \int dr_1 \dots p(\dots,l_1;r_1,\dots) \qquad (3.44)\\
[\;&- \;(\langle x(t)\rangle - (fL/k)\mu\,(l_1/L;r_1/L))\,(\delta(\lambda_1-l_1)\delta(\rho_1-r_1))\\
&+ \;(\langle x(t)\rangle - (fL/k)\mu\,(l_2/L;l_1/L))(-\delta(\lambda_1-l_2)\delta(\rho_1-l_1)+\delta(\lambda_1-l_2)\delta(\rho_1-(l_1+r_1)))\\
&+ \;(\langle x(t)\rangle - (fL/k)\mu\,(r_1/L;r_2/L))(-\delta(\lambda_1-r_1)\delta(\rho_1-r_2)+\delta(\lambda_1-(l_1+r_1))\delta(\rho_1-r_2))\\
&+ \;\langle x^n(t)\rangle_{l_1;r_1}\,(\delta(\lambda_1-l_1)\delta(\rho_1-r_1))\\
&+ \;(\langle x(t)\rangle - (fL/k)\mu\,(l_2/L;(l_1+r_1)/L)\,(-\delta(\lambda_1-l_2)\delta(\rho_1-(l_1+r_1))+\delta(\lambda_1-l_2)\delta(\rho_1-l_1))\\
&+ \;(\langle x(t)\rangle - (fL/k)\mu\,((l_1+r_1)/L;r_2/L))(-\delta(\lambda_1-(l_1+r_1))\delta(\rho_1-r_2)+\delta(\lambda_1-r_1)\delta(\rho_1-r_2))]\;,
\end{aligned}$$

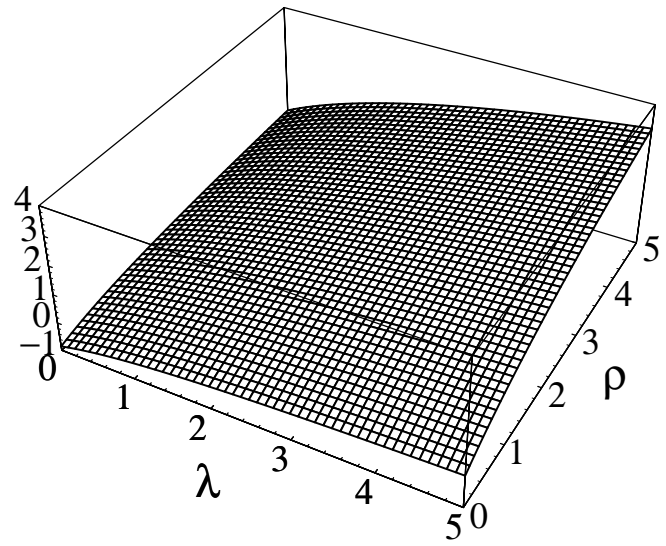

Figure 3.10: The function $\mu(\lambda;\rho)$ at $\gamma/kL = 1$.

which leads to an integral equation for μ and v. Its scale invariant form, using the coefficient $C_2 = vt_a k/f$, is

$$\begin{aligned} C_2 = &-3\mu(\lambda;\rho) + \int_0^\rho \mu(\lambda;\alpha)d\alpha + \int_0^\lambda \mu(\alpha;\rho)d\alpha \\ &+ \left(k\left\langle\frac{1}{K_e}\right\rangle\left(\frac{\lambda+\rho-1}{2}\right) + 1 + \frac{\lambda\rho}{2}\frac{kL}{\gamma}\right) \\ &+ k\left\langle\frac{1}{K_e}\right\rangle\int_0^\infty e^{-\alpha}\mu(\lambda+\rho;\alpha)d\alpha \\ &- (\lambda+\rho)\mu(\lambda;\rho) + \int_0^\infty e^{-\alpha}\mu(\lambda;\rho+\alpha)d\alpha + \int_0^\infty e^{-\alpha}\mu(\lambda+\alpha;\rho)d\alpha\ . \end{aligned} \tag{3.45}$$

A self-consistent solution that holds for all λ and ρ can be calculated numerically. The resulting coefficient C_2 is shown in Fig. 3.5 and a typical shape of the μ-Function in Fig. 3.10. The correction ν, defined in (3.38), gets the value $\nu \approx 1.50$. Taking first-order correlations into account improved the agreement between theory and simulation significantly. The remaining deviation, due to neglected correlations with further neighbours, is about 9% at low γ and lies below 14% over the entire parameter range.

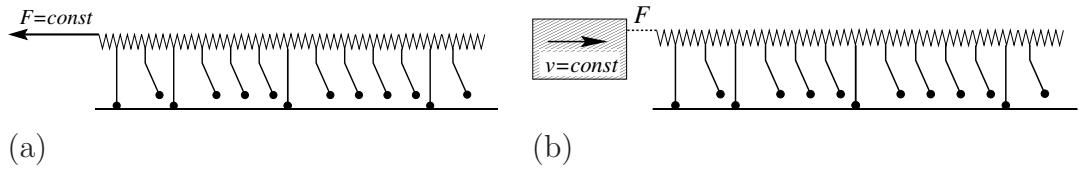

Figure 3.11: In a finite system, one has to distinguish between the force-velocity relation obtained for a constant force (a) and for a constant velocity (b).

3.5 Finite size effects

By now we have studied an infinitely long chain of elastically coupled motors, which reduced the number of model parameters to one. Of course, in any experimental realization we deal with a system of a finite length. Therefore, we address in this section the question to what extent and how the finite-size effects influence the force-velocity relation. Analytical arguments given in Sec. 3.4.6 have shown that the zero-load velocity remains unchanged by finite size effects (as well as by the backbone elasticity itself). On the other hand, they can well influence the slope of the f-v relation and therefore the stall force.

In an infinite system the f-v relation does not depend on whether the backbone moves with a constant velocity and one measures the average force or is loaded with a constant force and one measures the average velocity. The situation changes if the number of motors is finite (Fig. 3.11). If the backbone is infinitely stiff, its constant-velocity f-v relation remains the same as for an infinite system. The average velocity in the constant-force case actually diverges, since from time to time the situation occurs in which all motors detach at the same time and then the backbone, which is still loaded with a constant force, gets flushed away to infinity. The average time between two such encounters is given as

$$T = \frac{t_a}{N} e^N \ . \tag{3.46}$$

As one can see it becomes increasingly long for large N. Therefore, we can avoid these encounters by only observing the motion during the time between them. One obtains a new f-v relation, however with a lower stall force than obtained for the constant-velocity case.

3.5.1 Stiff backbone

In the following, we calculate the force-velocity relation of a group of stiffly coupled motors with a low duty ratio and the average number of attached motors N. The probability to find n motors in the attached state is given by the Poisson distribution

$$P_n = \frac{N^n}{n!} e^{-N} \,. \tag{3.47}$$

The rates for the transitions $n \to n \pm 1$ then read

$$r_{n\to n+1} = N t_a^{-1} \tag{3.48a}$$

$$r_{n\to n-1} = n t_a^{-1} \,. \tag{3.48b}$$

Since we want to exclude encounters in which all motors detach at the same time, we "forbid" the reaction $(n = 1) \to (n = 0)$ and obtain a new distribution

$$P'_n = \begin{cases} \frac{P_n}{1-P_0} & \text{for } n > 0 \\ 0 & \text{for } n = 0 \,. \end{cases} \tag{3.49}$$

While the mean x-value (the position of the attached motor heads) remains on average unchanged if a motor detaches, its change during an attachment event is

$$\Delta x = \frac{1}{n+1} \left(d - \frac{fN}{kn} \right) \,, \tag{3.50}$$

leading to the velocity

$$v = \sum_{n=1}^{\infty} P'_n r_{n\to n+1} \Delta x = \frac{d}{t_a} - \frac{f}{k t_a} \frac{1}{1-P_0} \sum_{n=1}^{\infty} \frac{N^n}{n!} e^{-N} \frac{N^2}{n(n+1)} \tag{3.51}$$

Expanding the second term for large N yields

$$v = \frac{d}{t_a} - \frac{f}{k t_a} \left(1 + \frac{2}{N} + \mathcal{O}(N^{-2}) \right) \,. \tag{3.52}$$

To summarise, even if the backbone is infinitely stiff, the finite size effects will reduce the stall force in the constant-force case.

3.5.2 Elastic backbone

With an elastic backbone, the situation becomes more complex. Again, we distinguish between the constant-velocity case, in which one end of the elastic backbone

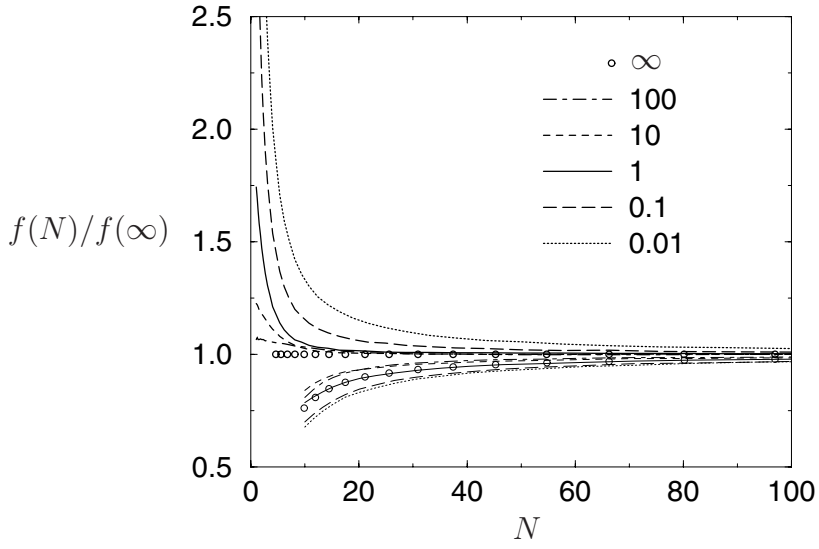

Figure 3.12: The normalized stalling force ($f = F/N$) for a finite group of N elastically coupled motors, divided through its bulk value; $f(N)/f(\infty)$. Data were obtained from a computer simulation with different values of the effective backbone stiffness γ/kL. The thick curves show the constant-velocity case and always lie above 1. The thin curves show the constant-force case and lie below 1. The circles indicate an infinitely stiff backbone.

is being moved with a constant velocity, and the constant-force case, in which a constant force pulls on that end (Fig. 3.11).

We have shown that the backbone elasticity lowers the efficiency of motors. In a finite system, the motors close to the ends are even more softly coupled to the rest. Therefore, in the constant-force case one intuitively expects a lower stall force per motor than in an ifinite system. On the other hand, in the constant-velocity case, one end is stiffly anchored. Therefore, one expects an improved efficiency on that side, but a worse one on the other side.

We have solved the model in both cases using computer simulations. The resulting normalised stall force is shown in Figure 3.12. One can see that the forces always lie above the bulk values in the constant-velocity case and below them in the constant-force case.

3.6 Strain-dependent detachment rates

By now, we have discussed the model with strain-independent detachment rates. This simplification allowed us to gain analytical insight into the model and describe its behaviour quantitatively and qualitatively. However, we have shown in Chapter 2 that the introduction of strain-dependent detachment rates is inevitable for a quantitative comparison with experiments on the actin-myosin system. Since the very beginning of muscle research it has been known that the force-velocity-relation rather has a hyperbolic form, also called the Hill curve [63]. It has also been known that the energy liberation in a stretching muscle depends on velocity, which is also called the Fenn effect [47]. The most natural way to reproduce these physiological measurements is the introduction of a strain-dependent detachment rate, meaning that the lifetime of the attached state $t_a = t_a(x_i - y_i)$ is larger for those heads that have just gone through the power stroke and produce maximum force than for those which have already done their work and now pull backwards. For simplicity we model this dependence as an exponential $t_a(\xi) = t_a^0 \exp(\alpha\xi)$, which suffices to fit the force-velocity-relation [63].

Strain-dependent detachment rates combined with an elastic backbone enhance the difficulty of an analytic solution of our model enormously, since the distribution of attached and detached motors depends on the distribution of head positions (x_i). Therefore, we will mainly use computer simulations and restrict analytic arguments on limiting cases. The results of a simulation are shown in Fig. 3.13. They show that two major analytic results of the strain-independent case carry over to the strain-dependent case: (i) If the backbone flexibility exceeds its characteristic value, the stall force decreases strongly. (ii) The backbone flexibility has only little influence on the zero-load velocity.

For stiff backbones ($\gamma/kL \gg 1$) the force-velocity-relation as measured by Hill [63] is reproduced perfectly using the value $\alpha d = 0.58$. For decreasing backbone stiffness ($\gamma/kL \ll 1$) the stall force decreases and the force-velocity-curve becomes increasingly linear. This can be understood as follows: The forces which lead to positive velocities become smaller and so does the strain on single motors. The small strain does not have any significant influence on the detachment rate any more and the results obtained for a strain-independent detachment rate become exact. The crossover from the Hill curve to a linear relation is shown in Fig. 3.13. There $\alpha d = 0.5$ is used, but the curves look qualitatively similar for other

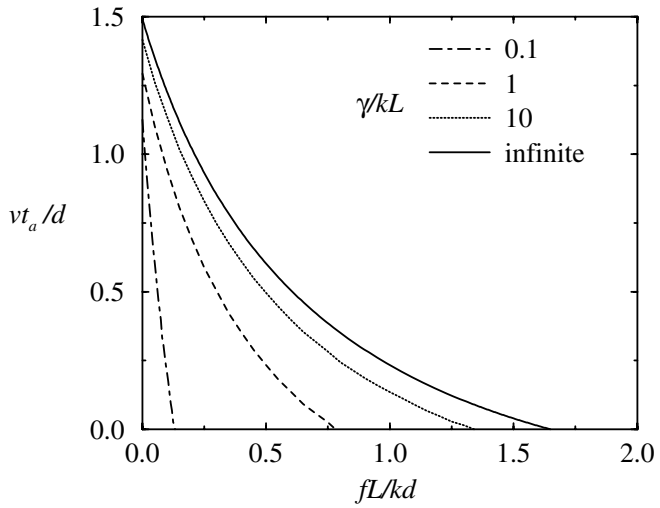

Figure 3.13: Simulation results for force-velocity-relations with strain-dependent detachment rates ($\alpha d = 0.5$) and different backbone stiffnesses. Note the crossover from the Hill curve at stiff backbones to a nearly linear relation at soft backbones.

positive values.

In Section 3.4 we showed that for very flexible backbones ($\gamma/kL \ll 1$) and strain-independent reaction rates ($\alpha = 0$) the zero-load velocity remains $\frac{d}{t_a}$, while the stall force is limited through the backbone stiffness as $f(v = 0) = 2\gamma d/\nu L^2$. The mean strain on a motor is given as $\langle\xi\rangle = fL/k$, or $2\gamma d/\nu kL$ at maximum load. For very flexible backbones this means $\alpha\langle\xi\rangle \ll 2\alpha d \approx 1$. The strain-dependence becomes negligible and the results from Sec. 3.4 are exact. From this simple argument we expect that the force-velocity relation becomes linear. The crossover from the hyperbolic to the linear shape takes place at $\gamma/kL \approx 1$. While the stall force (force at zero velocity) $f_{\text{stall}} = e^{\alpha d}kd/L$ is limited through the motor stiffness k for stiff backbones, it depends solely on the backbone stiffness for soft backbones, $f_{\text{stall}} = 2\gamma d/\nu L^2$. This behaviour is in agreement with our computer simulations, the results are shown in Fig. 3.13.

3.7 Implications for experiments

In order to apply our theory to experiments, we need the spring constants of the myosin heads and of the actin filaments. The elasticity of the attached myosin head was measured by a number of experimentalists [48, 80, 121, 113, 167] with

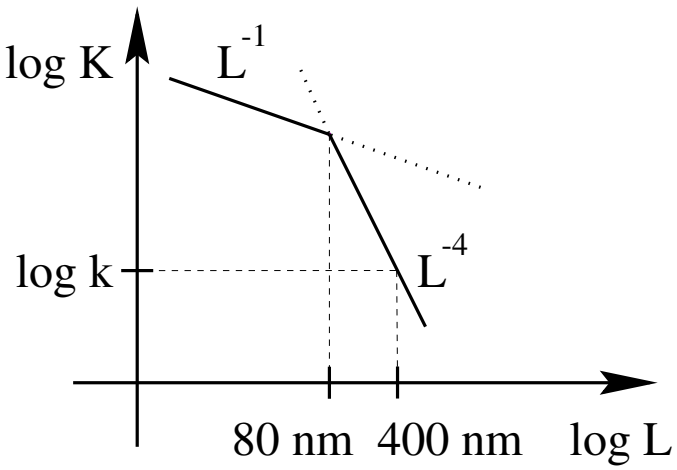

Figure 3.14: A schematic representation of the linear spring constant of an actin filament (or a fragment of it) as a function of its length. For short filaments, the stiffness is limited by the elastic modulus of actin and thus proportional to L^{-1}. For longer filaments, it becomes reduced due to the buckling modes and is proportional to L^{-4}.

the result of about $k = 0.65\,\mathrm{pN/nm}$.

In our model we assumed springs with flexibility proportional to their length, obeying $k_{\mathrm{spring}} = \gamma/L$. Actually actin is a semiflexible polymer. Its elastic behaviour was subject of many theoretical and experimental studies in last years [104, 94, 179, 53, 88]. There are essentially two contributions to the elasticity of actin: the longitudinal elastic modulus and the buckling of the polymer, induced through thermal fluctuations.

For short filaments or at very high loads, the stiffness is limited by the elastic modulus of actin and is proportional to L^{-1},

$$k_{\mathrm{actin}} = \gamma L^{-1} \tag{3.53}$$

with $\gamma \approx 44000\,\mathrm{pN}$ [88].

Otherwise, the buckling modes limit the stiffness of actin. In the linear response approximation, the stiffness of a polymer with length L obeys the law

$$k_{\mathrm{polymer}} = 90 k_B T \ell_p^2 L^{-4} \tag{3.54}$$

where ℓ_p denotes the persistence length. Although we assume springs obeying an L^{-1}-law, we can still use the L^{-4}-law to give an estimate for the characteristic distance for which $k_{\mathrm{polymer}}(L_{\mathrm{ch}}) \approx k$.

Recent measurements provide the value $\ell_p = 7.4\mu\mathrm{m}$ [142]. With these data, we find that the transition between the linear and the fourth-power behaviour

takes place at a filament length of about 80 nm, where the stiffness is about $K \approx 300\,\mathrm{pN/nm}$. Since this is much higher than the elasticity of a single myosin head, the filament elasticity only becomes crucial for longer filaments, in the regime dominated by thermal undulations (Fig. 3.14). With these values we finally estimate the characteristic distance between attached motors $L_{\mathrm{ch}} = (90 k_B T \ell_p^2 / k)^{1/4} \approx 400\,\mathrm{nm}$. If the mean displacement between attached motors is larger than L_{ch}, we expect that the effects of backbone elasticity should be observable.

In muscles the length of a half sarcomere is about 500 nm [10, 2]. Since one end of the actin filament is always connected with a Z-disc, we have to deal with the constant-force case in the classification made in the section about finite-size effects (Sect. 3.5). A rough estimate (300 myosin heads in one thick filament, 3 actin filaments per one thick filament, 10% of heads in the attached state) leads to L values about 50 nm, significantly below the characteristic length L_{ch}. Therefore the leading contribution to the actin elasticity is the intrinsic actin elasticity. This leads to an estimate of $\gamma/kL \approx 1300$, which gives a decrease of stall force by 2% according to Table 3.1. The finite-size effects would even further increase the efficency. However, as we have shown in Sect. 3.5, they are negligible as soon as more than a few motors are attached on average. This implies that the elasticity of actin filaments does not influence the operation of muscles significantly. This result is not surprising – backbone elasticity always reduces the efficiency of motors and it would be hard to understand why muscles should spoil their high efficiency in such a prodigal way.

Further effects of elasticity, which are not considered in our model, include the extension of the overleap zone between the thick and the thin filaments. Softer filaments mean that the number of active motors increases at higher forces. These effects have been studied by Daniel *et al.*, [33].

Chapter 4

Spontaneous wave generation

In Chapter 2 we have shown that a two-state model for molecular motors can show anomalous force-velocity relations. This causes a dynamic instability since there are several values of the velocity which lead to the same force. If a group of such motors pulls against an elastic spring, this leads to nonlinear oscillations. If we combine an anomalous force-velocity relation with the elastic coupling as discussed in Chapter 3, we expect the oscillations to go over into propagating waves. This situation resembles the spontaneous wave generation in flagella. In the following, we give a short summary of the most important experimental findings about flagellar movement.

4.1 Oscillatory microtubule sliding in the flagella

Flagella are used by sperm cells and certain protozoa for cell propulsion. They are about 50 microns long, 0.25 μm in diameter, and can generate waves with a constant amplitude and a typical frequency of $30\,\mathrm{s}^{-1}$. These waves then propel the cell. The waves always spread from the anchored towards the free end [101]. Usually the anchored end is in the cell body, but there are some exceptions.

Cilia are very similar in their composition but shorter [2]. Also the asymmetry is more pronounced, which allows a cilium to propel the surrounding fluid perpendicular to its axis. Cilia cover the surfaces of mammalian respiratory passages (e.g. the nose) where they move outwards particles that have been collected in the secretions. Some protozoa are also covered with cilia and use them for loco-

motion. They beat in a whiplike fashion with typical frequencies of 5-10 s^{-1}. Two reviews about experimental findings and theoretical models for cilia and flagella are given in [101, 22].

The essential part of a flagellum is a bundle of usually 9 outer and 2 inner microtubules, called the axoneme (Fig. 4.1). Between each pair of microtubules, dynein motors are placed in two rows every 24 nm. They pull the microtubules along each other, thus bending them. Like myosin, dynein obtains the necessary energy from ATP hydrolysis. The arrangement of microtubules causes an anisotropic bending stiffness having the consequence that the waves are planar. However, sometimes the central pair of microtubules is lacking. Then the anisotropy vanishes and the waves become helical. Such rotating cilia seem to be involved in establishing the left-right asymmetry during the growth an organism [1]. Calcium-regulation is mainly used by the cells to control the underlying curvature of a flagellum and thus for steering the direction of swimming.

Flagella keep their beating in viscous solutions up to ten times the viscosity of water, however the amplitude and the shape of the waves change at high viscosities [23]. Deletion of inner and outer arm dyneins from the flagella has different consequences for the generation of waves [22]. Flagella without outer arm dynein beat with almost unchanged waveforms, but at about half the frequency. Flagella lacking some inner arm dyneins, on the other hand, keep their frequency but strongly reduce the amplitude of the waves. It has also been shown that three microtubule doublets with corresponding dynein motors suffice to generate propagating waves *in vitro* [169].

Most theoretical models for flagellar beating are based on a self-organised mechanism. Some earlier models used a feedback mechanism in which the attachment probability of a dynein cross-bridge depends on the local curvature of the flagellum [21]. Newer models [120] are mainly based on a dynamic instability in the operation of dynein motors. An alternative model, the so called "Geometric Clutch" [101] again proposes that the dynein cross-bridges are activated when the tubulin doublets come closer to each other due to geometric effects.

In this section we will show that our model of elastically coupled motors with anomalous force-velocity relations describes the basic properties of self-organised generation of flagellar waves. We will use our model to derive the basic properties and the scaling laws of the generated waves.

A flagellum can essentially be described as a pair of parallel elastic rods with motors running between them (Fig. 4.2). We follow the standard nomenclature

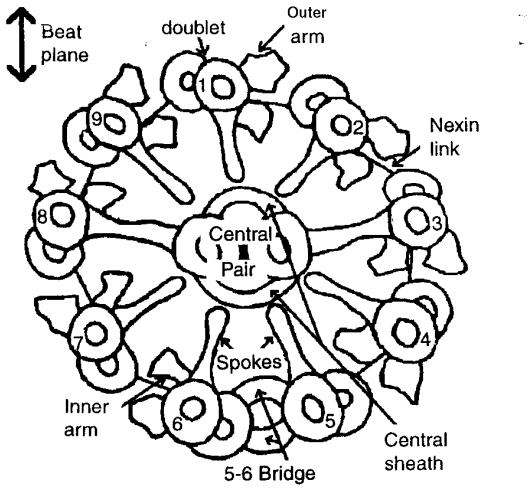

Figure 4.1: Cross-section of an axoneme which is the central end essential component of a cilium or a flagellum (from [101]). The outer doublets, arranged in a ring of nine, each posses an inner and outer row of dynein motors (also called dynein arms) causing a shear force. The exact structure can vary from species to species.

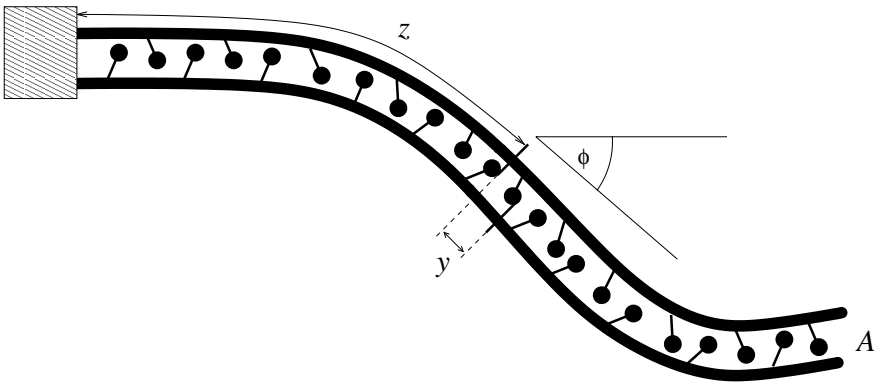

Figure 4.2: Schematic representation of two pair of microtubules (e.g. #2-3 and #8-9 in Fig. 4.1) with motors between them, representing the essential component of a flagellum. Without hydrodynamic friction, the model is equivalent to the linear model of elastically coupled motors.

and characterise the dynamics of a flagellum by the shear angle ϕ as function of the longitudinal coordinate z. The shear, which is equivalent to the linear backbone displacement y, is related to ϕ as $y = \phi A$, where A is the distance between both microtubules. The force density produced by the motors, f, causes a torque (density) Af, which bends the filaments according to

$$Af = \kappa \frac{d^2\phi}{dz^2} = \frac{\kappa}{A}\frac{d^2y}{dz^2} \; . \tag{4.1}$$

κ denotes the total bend stiffness of both filaments. This relation is equivalent to Eqns. (3.6a) and (3.7) with

$$\gamma \equiv \frac{\kappa}{A^2} \; . \tag{4.2}$$

During the bending, the shear angle between the microtubule doublets denoted as 7 and 8 (Fig. 4.1) approximately equals that between 8 and 9, between 4 and 3 and between 3 and 2. However, the motors fixed on doublets 2 and 3 and running along doublets 3 and 4 pull in the opposite direction as those between the doublets 7 and 8 and 8 and 9. We therefore use a model with an equal number of motors pulling in each direction.

A correct treatment of nexin links which connect each microtubule doublet with its two neighbours and stabilises the structure of the axoneme would require an additional term $f \propto -kz$. We neglect this term in the following treatment.

Hydrodynamic friction, which has been modelled as simple local viscous drag in many models [56, 24], certainly is an important issue. Since it is a function of the velocity of motion of a certain point on the flagellum, it becomes non-local in a representation in terms of the shear angle ϕ. We expect that it can significantly influence the waveform if the surrounding liquid is viscous enough. On the other hand, flagella can still move at viscosities an order of magnitude higher than water [23]. Also the waves show patterns similar to those obtained from our model at low viscosities, but change their form at higher viscosities. The behaviour of a flagellum close to the "critical point" where viscous load stops beating has been studied in Ref. [24]. It has been shown that in this limit the shape of the waves and even the direction of motion depend crucially on whether and how the flagellum head is clamped.

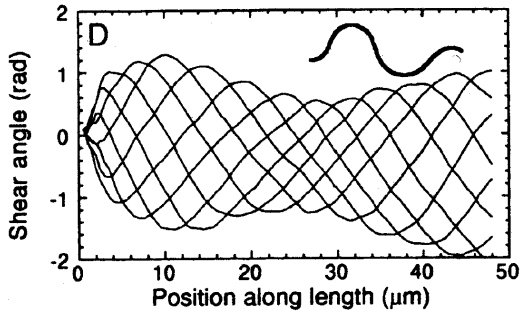

Figure 4.3: The shear angle ϕ of a flagellum, computed from its shape (stroboscopic photograph with taken with a frequency of 300 Hz). An example of the flagellum shape is shown in the upper right corner. Figure from Ref. [23].

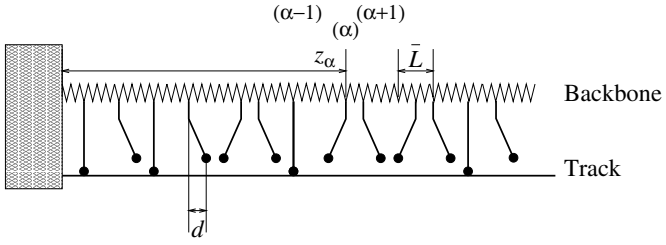

Figure 4.4: Definition of the model. Motors are fixed on the elastic backbone at uniform spacing $\bar{L}$ and attach to the stiff track. z_α denotes the position of α-th motor on the unstrained backbone. To model the effect of two sets of motors bending the flagellum in opposite directions, we reverse every second motor. At the left end, the backbone and the track are stiffly coupled.

4.2 Model definition

For single motors we will use the model as described in Chapter 2, however we will leave out discrete binding sites and thermal fluctuations, since they have been found to play only a minor role in the force-velocity-relation (Sect. 2.3). We further assume an antisymmetric force-velocity-relation since half of the dynein motors in a flagellum cause bending in one direction and the other half into the other one.

As in Sect. 3.2, we consider a backbone with $\bar{N}$ motors, placed at average displacement $\bar{L}$ (Fig. 4.4). The mean time a motor stays in the detached state is again denoted as t_d. The detachment rate is given as $t_a^{-1}(\xi)$, where ξ is the strain on that motor. We assume a low duty-ratio, $t_d \gg t_a$. We further assume that we are dealing with a relatively stiff backbone, $\gamma/kL \gg 1$.

The motion of motors is then described by Equations (3.4a) and (3.5). In order to achieve the antisymmetric force-velocity relation every second motor should point backwards, thus we set $d_{\alpha+1} = -d_\alpha$ and $t_a^{(\alpha+1)}(\xi) = t_a^{(\alpha)}(-\xi)$. We chose boundary conditions with left end fixed and right end open, thus $y_{\alpha=0} = 0$ and $y_{\alpha=\bar{N}} - y_{\alpha=\bar{N}-1} = 0$.

Figure 4.6 shows the motion of the endpoint $y_{\alpha=\bar{N}}$ of a chain, obtained from a computer simulation, and the shapes of the function $y(z)$. The stationary state contains waves, spreading from the fixed towards the open end. They indeed show high similarity with the the measured shear angle in a flagellum (Fig. 4.3). The force-velocity curve of the underlying motor model is shown in Fig. 4.5.

4.3 Local mean-field approach

A stiff backbone corresponds to a coupling of infinite range in the sense that each motor interacts with others only by sensing the backbone position y, which is the average of all head positions x_i. Therefore a mean-field theory provided an exact solution in Sect. 2.2.

Since we observe a relatively stiff backbone, $\gamma/kL \gg 1$, we may still apply that approximation locally. In analogy to (2.4) the local Master equation for each half of motors reads

$$(\partial_t - \dot{y}(z)\partial_\xi)\,\Phi_a(z,\xi,t) = \frac{1}{2\bar{L}t_d}\delta(\xi - d) - \frac{\Phi_a(z,\xi,t)}{t_a(\xi)}\ . \tag{4.3}$$

The equivalent of (3.6a) becomes

$$\gamma\frac{\partial^2 y}{\partial z^2} = -f(z) \tag{4.4}$$

with $f(z,t) = \int d\xi \Phi_a(z,\xi,t)k\xi - \int d\xi \Phi_a(z,-\xi,t)k\xi$.

4.4 Scaling properties

The equations of motion reveal the following scaling properties: they remain invariant if one rescales the given quantities as

$$\begin{array}{lll} f \to \alpha f & \gamma \to \alpha\gamma & \\ z \to \beta z & \gamma \to \beta^2\gamma & \\ y \to \delta y & v \to \delta v & f \to \delta f \\ t \to \epsilon t & v \to \epsilon^{-1} v & \end{array}$$

Using these relations one obtains for the wavelength

$$\lambda \propto \sqrt{\frac{\gamma v_0 t_0}{f_0}}\,, \tag{4.5}$$

the amplitude

$$A \propto v_0 t_0 \tag{4.6}$$

and the frequency

$$\nu \propto \frac{1}{t_0} \tag{4.7}$$

of the waves, where v_0 is the characteristic velocity in the f-$v-$ relationship, f_0 the characteristic force density and t_0 the characteristic time scale, determined through the detachment rate. The propagation velocity of the waves scales as

$$c = \lambda\nu \propto \sqrt{\frac{\gamma v_0}{f_0 t_0}}\,. \tag{4.8}$$

Note that these waves are highly nonlinear and therefore possess a rather sawtooth than a sinusoidal form. Also characteristic is their property that they always propagate from the closed towards the open boundary.

4.5 The influence of fluctuations

After we have introduced the phenomenological approach with an effective force-velocity relation one might ask how dense the motors have to be in order to make such an approach justifiable. The critical quantity is the ratio of stochastic

fluctuations and the average force, observed on the interval where the waves are actually generated.

A realistic estimate for the average force density is $\bar{f} = \frac{1}{10}kd/L$. The force fluctuations on an interval of length l are then $\delta f = \sqrt{N}kd = \sqrt{l/L}kd$. If we estimate the interval that is crucial for the generation of waves as $[0, \lambda/10]$, we set $l = \lambda/10$ and obtain the ratio

$$r = \frac{\delta f}{\bar{f}\, l} = \sqrt{\frac{1000\, L}{\lambda}}\,, \tag{4.9}$$

which is a measure for the influence of fluctuations. We expect that for $r \gtrsim 1$ the waves get lost completely in fluctuations, while they obtain their regular shape for $r \ll 1$.

To estimate of the ratio r for a realistic flagellum, we estimate the distance between attached motors as $L \approx 6,\mathrm{nm}$ (dynein arms are placed on microtubules at a distance of 24 nm, we estimate the number of dynein arms involved in wave generation as 8 and assume that half of the motors are attached at a time), the wavelength as $\lambda = 20\,\mu\mathrm{m}$ and obtain $r \approx 0.5$. In reality, the influence of fluctuations is probably weaker since dynein motors can be much better optimised for anomalous force-velocity-relations than the simple strain-dependence of the detachment rate used here. Besides, viscous drag could have a stabilising effect.

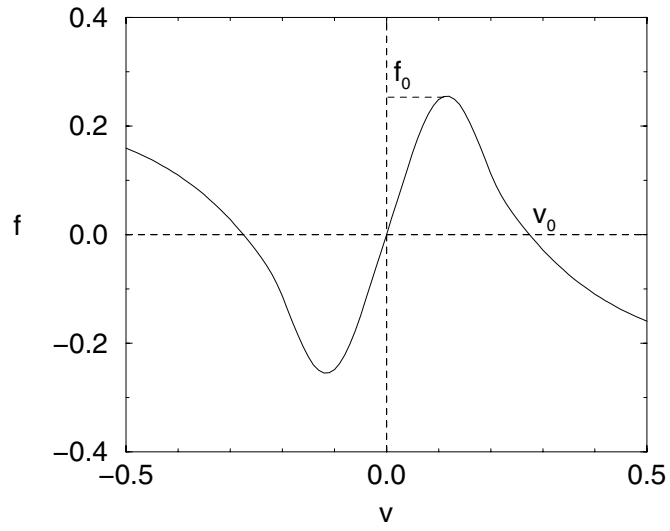

Figure 4.5: The anomalous force-velocity relation, obtained in a model with a detachment time $t_a = \exp(2 - 2\,\xi^2)$, power-stroke $d = 1$ and head elasticity $k = 1$. The same model has been used in all simulations of the wave generation.

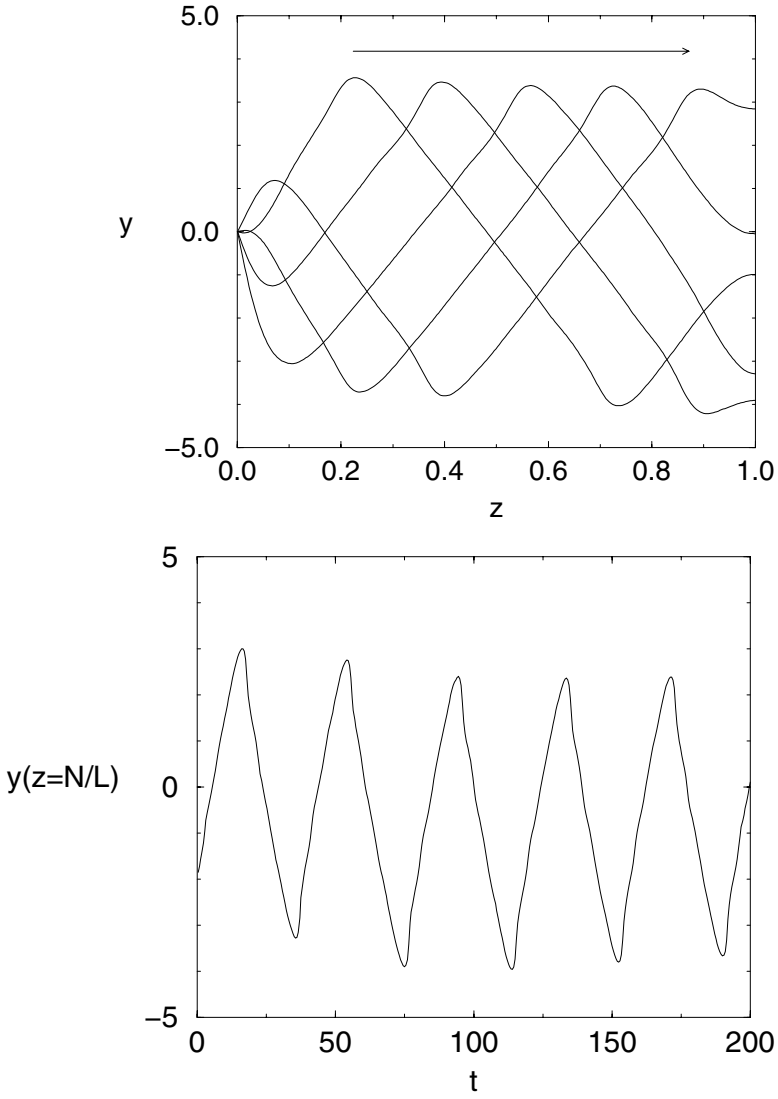

Figure 4.6: Snapshots of the backbone displacement $y(z)$ at times differing by 10 (top). The time dependence of the endpoint displacement $y(z = N/L)$ (bottom). Data were obtained form a computer simulation with $\gamma = 100$, $L = 1/360000$, $t_a = \exp(2 - 2\,\xi^2)$, $d = 1$ and $k = 1$. The estimate from Eq. (4.9) gives about $r = 1/20$. This value is sufficient to get periodic waves, although minor deviations are still visible.

Chapter 5

Decoration experiments

5.1 Introduction

In this Chapter we provide a theory describing passive motors at high densities. With "passive" we mean that they do not obtain any energy from ATP hydrolysis and therefore obey the law of detailed balance. High densities mean that a significant portion of binding sites is occupied at a time.

Our study is mainly motivated by experiments in which dimeric proteins from the kinesin family (kinesin, ncd ...) are adsorbed on the surface of microtubules. Such so called "decoration" experiments have become a standard method in biophysical chemistry to investigate the structure and the binding properties of kinesin. Decorated microtubules can be investigated using scanning transmission electron microscopy (STEM) with following image reconstruction, small angle X-ray scattering (SAXS) and biochemical investigations. These experiments allowed for new insights into the structure of kinesin and the way it binds to the microtubules [67, 86, 66, 68] thus providing important information for modelling kinesin movement along microtubules. They are either designed to measure the binding stoichiometries (number of kinesin molecules per tubulin binding site as a function of the kinesin solution concentration), or to reconstruct the structure of bound kinesin. One of the central questions to be answered is whether and under what circumstances both kinesin heads can bind simultaneously to a microtubule. A problem such experiments can encounter is the fact that even when simultaneous binding of both heads is possible, some of the kinesin molecules can still remain bound on one head just because there is no free binding site for the second one.

Although there is still much unknown about the binding of kinesin to microtubules, there seems to be convincing evidence that the kinesin heads can bind on two adjacent binding sites only in longitudinal but not in lateral direction [159]. This introduces a strong uniaxial anisotropy and distinguishes the adsorption process of protein dimers from simple inorganic dimers. If we take into account only steric interactions and neglect nearest neighbour attractive interaction, this reduces the dynamics to an essentially one-dimensional problem.

5.2 Definition of the model

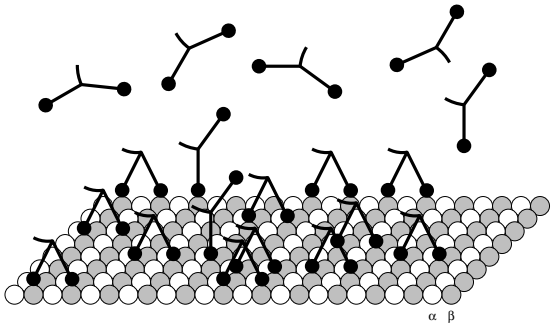

Figure 5.1: Schematic representation of the binding of kinesin dimers to a tubulin sheet. The binding sites are located on β subunits marked as black balls. A dimer can attach either with one head to one binding site or with two heads on two adjacent sites along the same protofilament. Two kinesin heads cannot attach to the same binding site.

Our model describes the experimental situation as found in most decoration assays. It starts with an empty tubulin sheet surrounded by a solution of double-headed kinesin. The kinesin molecules can either attach with one head onto a binding site on β-tubulin or with two heads on two adjacent binding sites on the same protofilament. The attached heads can also detach at some rate. The situation is sketched in Figure 5.1. To begin with, we assume that there is no interaction between attached kinesin molecules except for the fact that two heads cannot attach to the same binding site at a time. This means that kinesin dimers attached to different protofilaments do not influence each other. Each protofilament can be described independently and we can describe it by a one-dimensional model as shown in Figure 5.2.

A reaction scheme with all possible processes and their corresponding rate

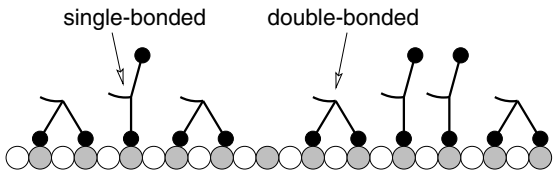

Figure 5.2: Schematic representation of the one-dimensional model describing a protofilament in the case without interaction.

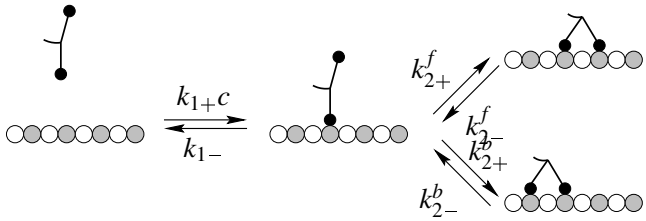

Figure 5.3: Reaction scheme for all possible binding and unbinding processes of kinesin dimers to the sites (shaded circles) of a one-dimensional lattice (called tubulin protofilament). Kinesin binding sites are located on β-tubulin subunits (shaded circles) while α-subunits (open circles) are irrelevant for our study.

constants is shown in Fig. 5.3. The binding rate $k_{1+}\,c$ for the first head is proportional to the solution concentration c of the dimeric proteins. Successively, the dimer may either dissociate from the protofilament with a rate k_{1-} or also bind with its second head to an unoccupied site in front (f) of or behind (b) the already bound head. Since both kinesin and microtubules are polar structures – a property which allows them to perform directed transport – the corresponding binding rates k^f_{2+} and k^b_{2+} are in general different from each other. The reverse process of detaching a front or rear head occurs at rates k^f_{2-} and k^b_{2-}. Since there is no energy source in the system (unlike situations where ATP is being hydrolysed), the reaction rates obey the principle of detailed balance. As a consequence, the reaction rates are actually not independent from each other but the ratio of the on- and off-rates has to equal the equilibrium binding constant

$$K_2 = k^b_{2+}/k^b_{2-} = k^f_{2+}/k^f_{2-} \tag{5.1}$$

similarly we have

$$K_1 = k_{1+}/k_{1-} \tag{5.2}$$

A particular coverage of the lattice is described as a sequence of dimers bound with both heads (D), one head only (1) and empty sites (0). We denote the probabilities to find a certain lattice site in one of these states by $2n_D$, n_1 and n_0, respectively. Of course, normalisation of the probabilities requires

$$n_0 + n_1 + 2n_D = 1 \; . \tag{5.3}$$

The major quantity of interest is the binding stoichiometry, giving the number of attached kinesin heads per tubulin binding site as a function of kinesin concentration. Generically, even the noninteracting model is described by six reaction rates $k_{i\pm}$. However, the equilibrium binding stoichiometry depends only on the solution concentration c and the free energy difference between the states, which is expressed in the reaction constants (K_1 and K_2). They are characteristic for the particular type of the motor protein (different kinds of kinesin or ncd) and the nucleotide bound to it (ADP, AMP-PNP etc.).

At low concentrations, when the attached molecules do not hinder each other, the binding constants can be written as

$$\begin{aligned} K_1 &= \frac{[\text{Kin. bound on one head}]}{[\text{Kin. in solution}][\text{Tubulin}]} \\ K_2 &= \frac{[\text{Kin. bound on both heads}]}{[\text{Kin. bound on one head}]} \; . \end{aligned}$$

5.3 Symmetries

We start our analysis with the stoichiometry of the final steady state. Important information can be gained already by exploiting the symmetries of the kinetic process. A glance at the reaction scheme in Fig. 5.4 reveals a "particle-hole" symmetry. Upon interchanging the role of dimers bound on a single head and vacant sites

$$0 \leftrightarrow 1$$

the reaction scheme and hence the dynamics remains invariant for

$$(k_{1+}c, k^f_{2\pm}) \leftrightarrow (k_{1-}, k^b_{2\pm}) \; .$$

Since the coverage in the steady state is only a function of the quantities $K_1 c$ and K_2 this symmetry implies that the mean number of dimers attached with both

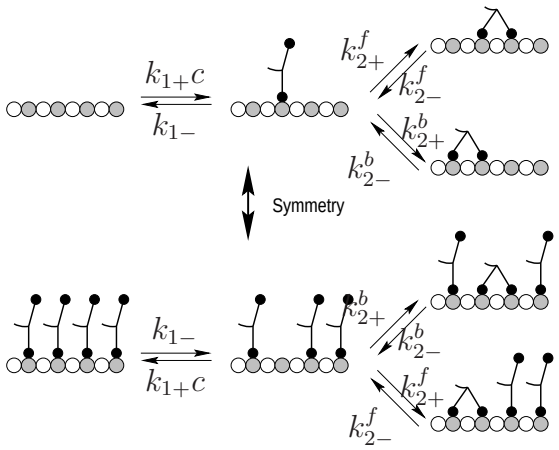

Figure 5.4: The model is invariant upon exchanging empty lattice sites (0) with single-bonded dimers (1) and the reaction rates as $(k_{1+}c, k^f_{2\pm}) \leftrightarrow (k_{1-}, k^b_{2\pm})$.

heads $n_D(K_1c, K_2)$ is invariant upon interchanging the attachment and detachment rates of the first head,

$$n_D(1/K_1c, K_2) = n_D(K_1c, K_2) \tag{5.4}$$

Similarly the mean total number of bound heads per lattice site (binding stoichiometry), $\nu = 2(n_1 + n_D)$, obeys the symmetry relation

$$\nu(1/K_1c, K_2) = 2 - \nu(K_1c, K_2)\ . \tag{5.5}$$

The symmetries can can be best seen in a logarithmic-linear plot as shown in Fig. 5.6. From these relations we already conclude that n_D reaches its maximum at $K_1c = 1$ and $\nu = 1$ at that point.

5.4 Equilibrium

We determine the actual value of the mean occupation numbers in the steady state using detailed balance and the fact that the dimers have only a hard-core interaction. Hence the probability to find a certain sequence of 0's, 1's and D's (e.g. "0,1,D,D,1,D") has to be invariant against permutations of these states (Fig. 5.5). In such a random sequence the probabilities to find a particular state 0, 1 or D at a certain place are given by $p_i = n_i/(n_0 + n_1 + n_D)$. Detailed balance requires that for each pair of possible configurations, their probabilities are in the

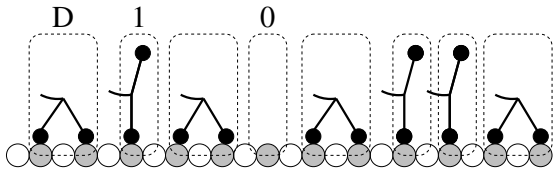

Figure 5.5: A configuration of bound kinesin molecules on a protofilament. The element D represents a dimer with two bound heads, the element 1 a dimer bound on one head and the element 0 an empty lattice site.

same ratio as the transition rates between them. Hence the ratio of probabilities to find a sequence with a 1 or 0 at a certain place is $k_{1+}c/k_{1-}$:

$$\frac{p_1}{p_0} = \frac{n_1}{n_0} = \frac{k_{1+}c}{k_{1-}} = K_1 c \; . \tag{5.6}$$

Similarly we get for transitions between D and 01

$$\frac{p_D}{p_0 p_1} = \frac{n_D(n_0 + n_1 + n_D)}{n_0 n_1} = \frac{k_{2+}^{b,f}}{k_{2-}^{b,f}} = K_2 \; . \tag{5.7}$$

These two equations, together with the normalisation condition, uniquely determine the values n_0, n_1 and n_D. The stoichiometry, i.e. the total number of heads per binding site $\nu = 2(n_1 + n_D)$ is given by

$$\nu = 1 + \frac{K_1 c - 1}{\sqrt{4K_1 K_2 c + (K_1 c + 1)^2}} \; . \tag{5.8}$$

The number of bound heads whose dimer partners are bound too is then given as $\nu_D = 2n_D$:

$$\nu_D = 1 - \left(\frac{4K_1 K_2 c}{(1 + K_1 c)^2} + 1 \right)^{-\frac{1}{2}} \tag{5.9}$$

and is shown in Fig. 5.6 The number of dimers bound width both heads per lattice site reaches its maximum $n_D^{\max} = 1/2 - 1/2\sqrt{K_2 + 1}$ for $K_1 c = 1$. At this concentration one always gets $\nu = 1$, as already shown above using symmetry arguments.

5.5 Scatchard plots

Scatchard plots are a standard method in biophysical chemistry to characterise ligand binding. The abscissa shows the average number of bound ligands per

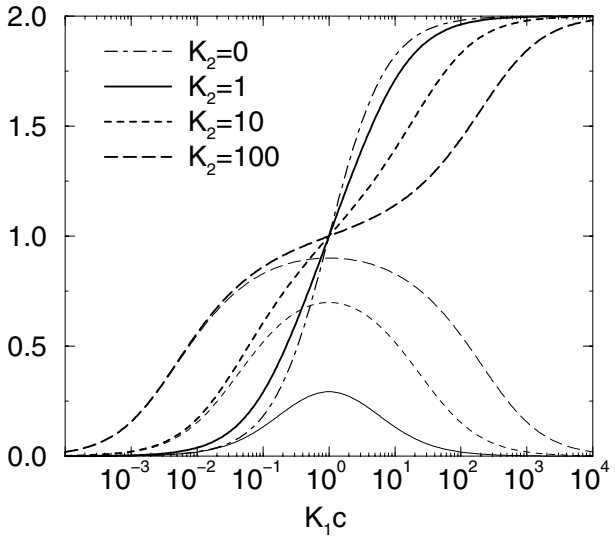

Figure 5.6: Binding stoichiometry ν as a function of the solution concentration c and the constant K_2. The thick curves show the total number of heads per lattice site (5.8). The thin curves show the fraction of binding sites occupied with double-attached dimers, ν_D.

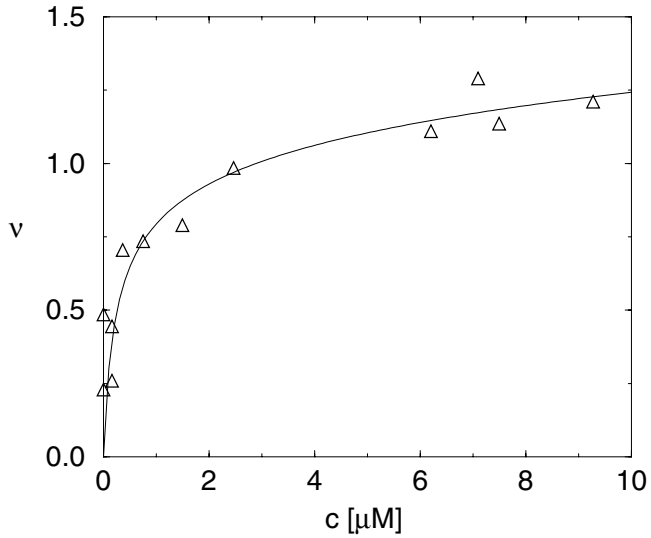

Figure 5.7: Binding stoichiometry ν as a function of the solution concentration c for K498 kinesin in the presence of AMP-PNP, compared with the result of Eq. (5.8). Data were fitted with $K_1 = 0.35\,\mu\mathrm{M}^{-1}$ and $K_2 = 6.0$. Experimental data are from Ref. [159].

binding site (in our case ν) and the ordinate the same number divided through the solution concentration (ν/c). Since models with independent ligands always show a linear dependence, any curvature indicates some cooperativity (which is already given if a dimer occupies two binding sites at a time). A Scatchard plot for different values of K_2 is shown in Fig. 5.8. The experimental data from Fig. 5.7 in Scatchard representation are shown in Fig. 5.9.

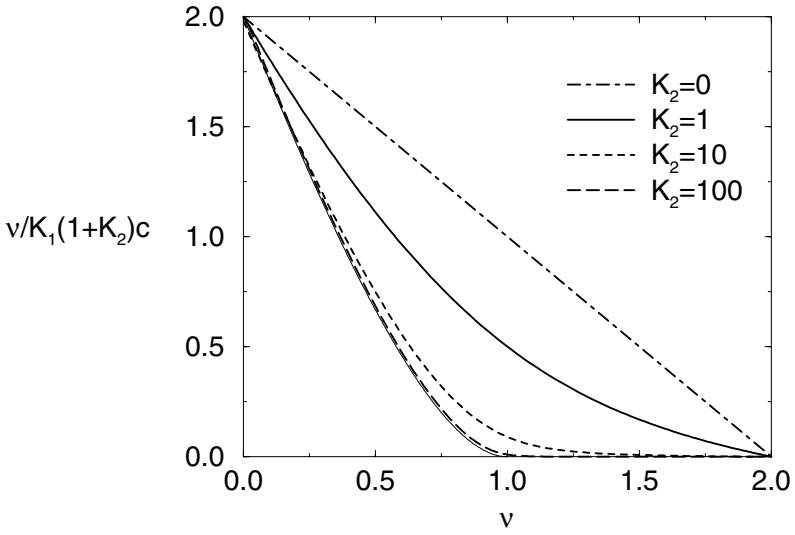

Figure 5.8: Scatchard plot (mean occupancy divided through solution concentration versus mean occupancy) of the dimer binding stoichiometry (5.8). The non-interacting monomer binding model would produce a linear curve, similar to that for $K_2 = 0$. The thin solid line shows the limit $K_2 \to \infty$ (stiff dimer model), given by Eq. (5.10).

In the limit $K_2 \to \infty$ the majority of dimers are either bound with both heads or not bound at all. This corresponds to the "stiff dimer" limit which will be discussed in Sect. 6.1 and has already been solved by McGhee and von Hippel [111]. Then the Scatchard curve obtains the form

$$\frac{\nu}{c}\frac{1}{2K_1(1+K_2)} \approx \frac{(1-\nu)^2}{1-\nu/2}\theta\,(1-\nu)\ , \tag{5.10}$$

in agreement with results by McGhee and von Hippel [111].

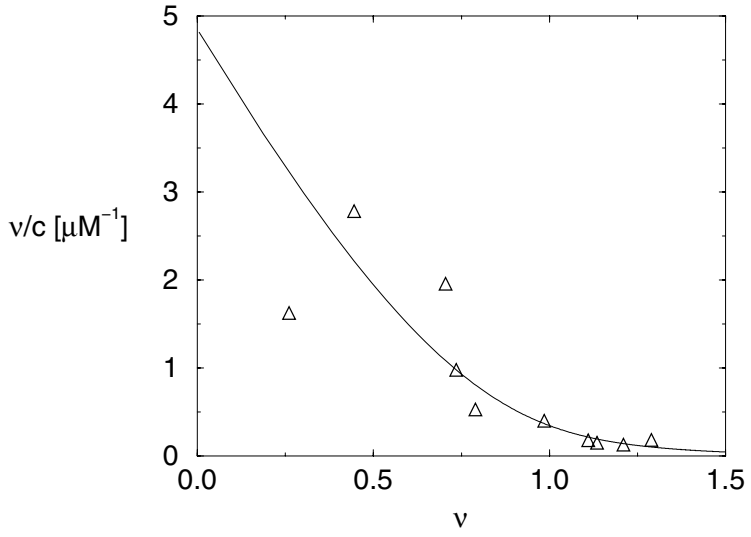

Figure 5.9: Same data as in Fig. 5.7, shown in a Scatchard plot.

Chapter 6

Relaxation towards equilibrium

How does a system evolve towards its steady state? Sometimes the answer is quite simple and the relaxation process is merely an exponential decay. If the deviations from equilibrium are small Onsager's regression hypothesis [125] asserts that the relaxation is governed by the same laws as the fluctuations in equilibrium. This hypothesis certainly fails for systems with an absorbing steady state such as simple models for diffusion-limited chemical reactions [160, 161, 137, 130]. Here there are no fluctuations in the steady state but the approach towards the absorbing state is critical in the sense that it exhibits slow power-law decay and universal scaling behaviour [25]. Symmetries, and conservation laws derived from them, in conjunction with correlations play a crucial role in understanding the origin of such anomalous kinetics [12, 151, 144, 26]. Most of these models are chosen to be mathematically transparent hoping that they still resemble some of the essential features of actual systems occurring in nature. Unfortunately, experimentally accessible systems where the above theoretical ideas can be tested explicitly have remained rare to date. This is in particular true for one-dimensional systems. In this chapter, we show that the simple dimer adsorption model introduced in Chapter 5 shows complex nonequilibrium dynamics which is both mathematically transparent and a realistic candidate to be accessible to experimental observation.

The adsorption of kinesin has two specific properties which distinguish it from the adsorption of simple inorganic dimers. First, there is the strong uniaxial anisotropy, connected with the fact that motors are able to move along a single protofilament [138], suggesting that both heads can bind on two adjacent binding sites only in longitudinal but not in lateral direction. Evidence supporting this assumption also come from analysis of decorated microtubules [159]. The second

important property of kinesin arises from the fact that a dimer remains together after binding and can not dissolve like inorganic dimers do [184]. This distinguishes our model from Ref. [12] where regrouping of the dimers after binding is allowed.

Although our primary motivation is to describe the binding of kinesin to microtubules, the model and the two-stage relaxational behaviour should apply to a broader range of problems. One is the binding of dimeric myosin on actin (which is naturally a one-dimensional problem) [127]. Another similar situation is the binding of tropomyosin to actin [177, 178], except that tropomyosin occupies seven actin binding sites.

The purpose this theoretical study of the relaxational dynamics of dimer adsorption models is twofold. First, it allows us to determine the equilibration time of the observed system. The equilibration time is important to be known in an experiment in order to know whether one really measures the equilibrium configuration and stoichiometry. Second, in some cases the measurement of the relaxational dynamics could provide information about reaction rates even when they are too fast for direct observation.

6.1 Stiff dimer model as limiting case

We now turn to the nonequilibrium dynamics of our model. In order to avoid unnecessary complications we restrict ourselves to the limit

$$K_2 \gg 1, \qquad K_1 c \ll 1 \tag{6.1}$$

with $K = K_1 K_2 c$ fixed. The first condition states that the second head is unlikely to be found in the unbound state if it has a place where it can bind. The second condition additionally states that isolated single-site vacancies are unlikely to be occupied with single-bonded dimers. Therefore our model reduces to a dimer deposition-evaporation model where the dimers can only bind and unbind with both heads at the same time. We will refer to this model as "stiff dimer model" in the following. The vacancy concentration in the steady state, given as $1-\nu+\nu_T$ in Eq. (5.8) and (5.9), then simplifies to $n_0 = 1/\sqrt{1+4K}$. This simplified model still captures all the essential aspects of the nonequilibrium dynamics. It is similar to a model introduced by Stinchcombe and coworkers [12, 151], the crucial difference being that our model does *not* allow for regrouping of adsorbed

dimers. Stinchcombe *et al.* [151] have shown that in the steady state the autocorrelation functions for the dimer density shows an interesting power-law decay $\propto t^{-1/2}$. This behaviour can be directly linked to the gapless spectrum in an associated spin model [151]. This power-law decay is lost (and becomes a simple exponential) due to the permanent linkage between the two heads of the dimer, as we will show later in Sect. 6.4. Intuitively this may be understood as follows: only if regrouping of dimers is allowed there are locally jammed configurations in the final steady state which slow down the dynamics. These jammed configurations contain checkerboard states with alternating occupied and unoccupied sites, which locally allow neither an attachment or a detachment. The difference between the occupation numbers on even and odd sites then represents a conserved quantity slowing down the dynamics. In our model, the conservation law is trivial since the difference between occupation numbers on even and odd sites always disappears.

In the following we describe how the kinetics of the stiff dimer model follows from our general dimer model. In the limit we are observing, the detachment of a single-bound dimer is always much faster than the attachment of a new one ($k_{1-} \gg k_{1+}c$) and the attachment of the second head much faster than its detachment ($k_{2+}^{f,b} \gg k_{2-}^{f,b}$). We do not put any other limitations on the reaction rates for now.

In a general treatment, the attachment and detachment rates also depend on the occupancy of the neighbouring sites. We therefore have to distinguish between four cases: both neighbours empty, front neighbour occupied, rear neighbour occupied and both neighbours occupied.

- **Both neighbours empty**

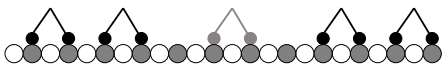

A dimer attaches with its first head at the rate $k_{1+}c$. Afterwards, the second head can attach at the total rate $k_{2+}^f + k_{2+}^b$, while the first head can detach with rate k_{1-}. This leads to the total attachment rate per lattice site

$$k_+ c = \frac{k_{1+}c(k_{2+}^f + k_{2+}^b)}{k_{1-} + k_{2+}^f + k_{2+}^b} \,. \tag{6.2}$$

The process of detachment starts with the detachment of the front or back head. The detachment gets completed if the other head detaches too (rate k_{1-}) and fails if the detached head reattaches again (rate $k_{2+}^f + k_{2+}^b$). The

detachment rate then becomes

$$k_- = \frac{k_{1-}(k_{2-}^f + k_{2-}^b)}{k_{1-} + k_{2+}^f + k_{2+}^b} \,. \tag{6.3}$$

- **Front neighbour occupied** 

The first head can either attach on the site beneath the occupied one or to the other one, both at the rate $k_{1+}c$. In the first case the probability that the second head will attach before the first one detaches is $k_{2+}^b/(k_{1-}+k_{2+}^b)$. In the second case the probability that the second head attaches in front of the first one is $k_{2+}^f/(k_{1-}+k_{2+}^f+k_{2+}^b)$. These two terms taken together give the attachment rate to the given pair of sites

$$k_+c = k_{1+}c\left(\frac{k_{2+}^b}{k_{1-}+k_{2+}^b} + \frac{k_{2+}^f}{k_{1-}+k_{2+}^f+k_{2+}^b}\right) \,. \tag{6.4}$$

If the process of detachment starts with detaching the front head (rate k_{2-}^f), the probability that the whole dimer will detach afterwards is $k_{1-}/(k_{1-} + k_{2+}^f + k_{2+}^b)$. If it starts with detaching the rear head (rate k_{2-}^b), this probability is $k_{1-}/(k_{1-} + k_{2+}^b)$. This gives the total detachment rate

$$k_- = k_{1-}\left(\frac{k_{2-}^b}{k_{1-}+k_{2+}^b} + \frac{k_{2-}^f}{k_{1-}+k_{2+}^f+k_{2+}^b}\right) \,. \tag{6.5}$$

- **Rear neighbour occupied** 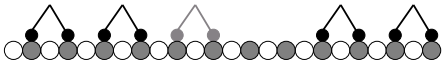

This case is analogue to the previous one, except that the indices f and b have to be exchanged. The attachment rate becomes

$$k_+c = k_{1+}c\left(\frac{k_{2+}^b}{k_{1-}+k_{2+}^f+k_{2+}^b} + \frac{k_{2+}^f}{k_{1-}+k_{2+}^f}\right) \tag{6.6}$$

and the detachment rate

$$k_- = k_{1-}\left(\frac{k_{2-}^b}{k_{1-}+k_{2+}^f+k_{2+}^b} + \frac{k_{2-}^f}{k_{1-}+k_{2+}^f}\right) \,. \tag{6.7}$$

- **Both neighbours occupied** 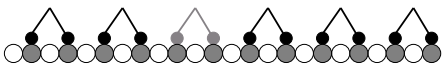

If the first head attaches in the front place inside the vacancy (rate $k_{1+}c$),

the probability for the second one to attach before the first one detaches is $k_{2+}^b/(k_{1-} + k_{2+}^b)$. Together with the analogue case in which the first head attaches to the rear site inside the vacancy, the total attachment rate becomes

$$k_+ c = k_{1+} c \left(\frac{k_{2+}^b}{k_{1-} + k_{2+}^b} + \frac{k_{2+}^f}{k_{1-} + k_{2+}^f} \, . \right) \tag{6.8}$$

After the front head has detached (rate k_{2-}^f), the probability that the whole dimer will follow is $k_{1-}/(k_{1-} + k_{2+}^f)$. Adding the pathway starting with the detachment of the rear head gives the detachment rate

$$k_- = k_{1-} \left(\frac{k_{2-}^b}{k_{1-} + k_{2+}^b} + \frac{k_{2-}^f}{k_{1-} + k_{2+}^f} \, . \right) \, . \tag{6.9}$$

Of course, all these rates fulfil detailed balance, which states that

$$\frac{k_+ c}{k_-} = K = K_1 K_2 c \, . \tag{6.10}$$

Processes in which one head detaches on one side and subsequently attaches on the other side also lead to an *explicit* diffusion of attached dimers. A diffusive step forwards occurs if the rear head detaches (rate k_{2-}^b) and reattaches on the front side (probability $k_{2+}^f/(k_{1-} + k_{2+}^f + k_{2+}^b)$). The hopping rate (which is, of course, equal for backward steps) then reads

$$r_d = \frac{k_{2+}^f k_{2+}^b}{K_2 (k_{1-} + k_{2+}^f + k_{2+}^b)} \, . \tag{6.11}$$

Later we will introduce the effective diffusion, which, in addition, contains terms arising from total detachment of a dimer and reattachment one place aside.

6.1.1 Strong diffusion

In some cases, the Equations (6.2-6.9) can be further simplified. If both attachment rates of the second head are significantly higher than the detachment rate of the first head,

$$k_{1-} \ll \min(k_{2+}^f, k_{2+}^b) \, , \tag{6.12}$$

a dimer can diffuse over many sites before it detaches, $r_d \gg k_-$.

The attachment rate simplifies to

$$k_+ = \begin{cases} k_{1+} & \text{for} \\ \left(1 + \frac{k^b_{2+}}{k^b_{2+}+k^f_{2+}}\right) k_{1+} & \\ \left(1 + \frac{k^f_{2+}}{k^b_{2+}+k^f_{2+}}\right) k_{1+} & \\ 2k_{1+} & \end{cases} \tag{6.13}$$

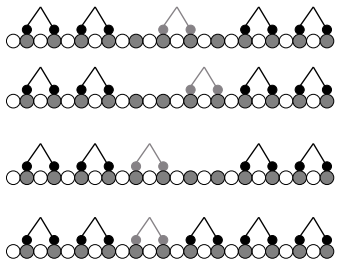

and analogously the detachment rates.

6.1.2 Vanishing diffusion

In the other limit, at least one of both attachment rates of the second head is much smaller than the detachment rate of the first head,

$$k_{1-} \gg \min(k^f_{2+}, k^b_{2+}) \ , \tag{6.14}$$

making the explicit diffusion negligible as compared to the detachment rate, $r_d \ll k_-$.

Further, a glance at Equations (6.2-6.9) reveals that the attachment rates become independent of the neighbourhood and always equal those given by (6.2) and (6.3). It is intuitively clear that the neighbourhood can not influence the attachment and detachment rates in the case of vanishing diffusion. Unless differently specified, we will always refer to this case in the rest of the chapter.

6.2 Two-stage relaxation

To study the kinetics we choose the same initial condition as typically used in a microtubule decoration experiment, namely an all empty lattice. Fig. 6.1 shows computer simulation data for the average vacancy concentration as a function of time for a set of different values of the binding constant $K = k_+c/k_- \equiv K_1K_2c$. We find qualitatively very different approaches to the final steady state depending on the value of the binding constant K. For $K \ll 1$, where the off-rates k_- are much larger than the on-rates k_+c, there is no crowding on the lattice and the dimeric nature of the molecules does not affect the approach to the equilibrium, which is, like in the monomeric case, exponential with a decay rate k_-. In the opposite limit, $K \gg 1$, we find a *two-stage relaxation* towards the steady state.

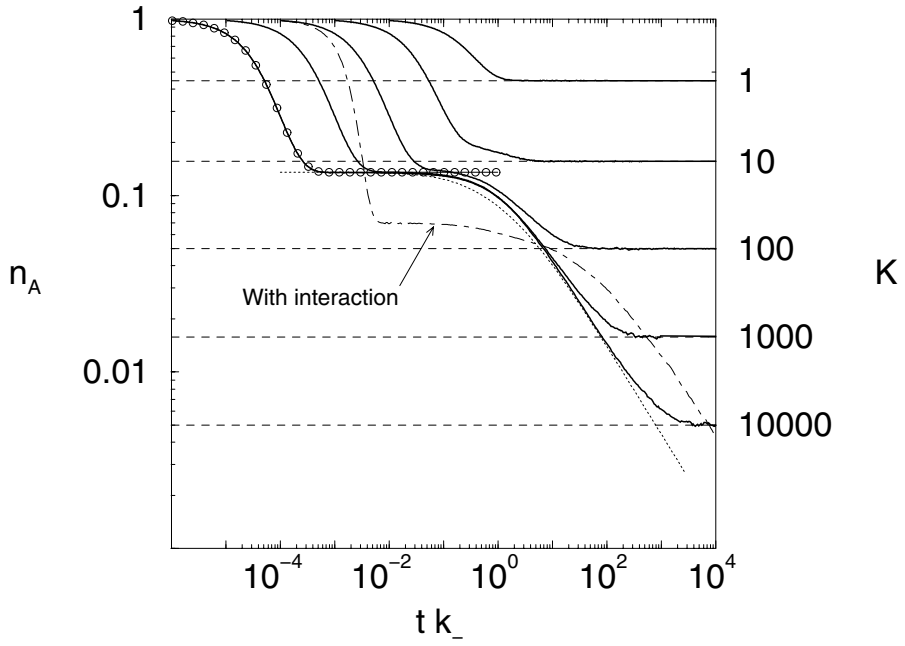

Figure 6.1: Vacancy concentration as a function of time t for $K = k_+c/k_- = 1$, 10, 100, 1000 and 10000. Dashed lines show the steady state concentration $n_0 = 1/\sqrt{1+4K}$ at given K. The line with circles shows the short-time limit for $K = 10000$ (Eq. 6.15), and the dashed line the result of the reaction-diffusion model (Eq. 6.18). The thin dot-dashed curve shows the behaviour of the model for $K = 100$ with an attractive interaction between bound dimers with parameters $A = 10$ and $B = 1/10$ (a dimer is 10 times as likely to associate to and 10 times less likely to dissociate from a certain site if one of the neighbours is present).

The vacancy concentration as function of time reveals *four regimes*, an initial attachment phase, followed by an intermediate plateau, then a power-law decay and finally an exponential approach towards equilibrium.

6.2.1 Initial attachment

At short time scales, $t \ll k_-^{-1}$, when only deposition processes are frequent but detachment processes are still very unlikely, the kinetics of the model belongs to the class of problems referred to as *random sequential adsorption* (RSA). The deposition of stiff dimers has already been studied by Flory [51]. Later, it was pointed out by Page [128] (see also a note by Downton [39]) that the final distribution depends on whether dimers bind with both ends in parallel or with one end first. An article addressing this point and giving analytical solutions for both cases was published by Nord and Evans [124]. An analytical solution for the

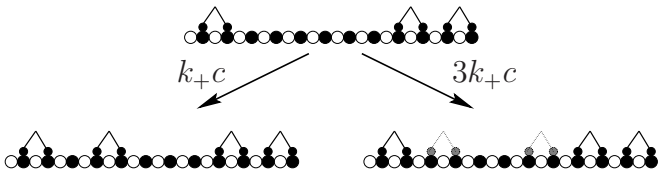

Figure 6.2: In the limit with strong diffusion, the rate at which pairs attach to each position inside the free interval is r, while the attachment rates to both boundary places together give $3r$.

time-dependence of the lattice coverage was given by McQuistan and Lichtman [112]. A review on RSA has been written by Evans [45].

According to McQuistan's and Lichtman's result [112], the vacancy concentration in our model obeys

$$n_0(t) = \exp\left(-2 + 2e^{-k_+ ct}\right) \ . \tag{6.15}$$

during the initial phase. It locks at an intermediate plateau $n_0 = e^{-2} \cong 0.1353$ [51] in the time interval between the characteristic attachment time $\tau_+ = 1/k_+c$ and detachment time $\tau_- = 1/k_-$. This Flory plateau is known for its jammed dimer configuration, i.e. all the remaining vacancies are isolated causing the system to be unable to accommodate for the deposition of additional dimers.

Similar behaviour can also be observed in the limit of strong diffusion, assumed that there is still a time scale separation between the attachment rate and the diffusion rate, $k_+c \gg r_d$. However, there is a difference, namely that dimers are more likely to bind beneath occupied sites than in the middle of an empty interval on the lattice. From (6.13) one can see that the deposition rate at both ends of an empty interval (Fig. 6.2) together gives $3k_+c$, while it equals k_+c for places inside the interval and $2k_+c$ for a pair of vacant sites surrounded by occupied ones. In this case the kinetics is equivalent to the "head-on" filling model [128, 124]. The vacancy concentration at the plateau becomes

$$n_0 = \sqrt{2\pi e}(\mathrm{Erf}(\sqrt{2}) - \mathrm{Erf}(1/\sqrt{2})) - 1 \cong 0.1233 \ , \tag{6.16}$$

slightly smaller than in the standard dimer model. The difference is plausible since a higher probability of binding beneath other dimers leads to some clustering and thus reduces the number of leftover standalone vacancies.

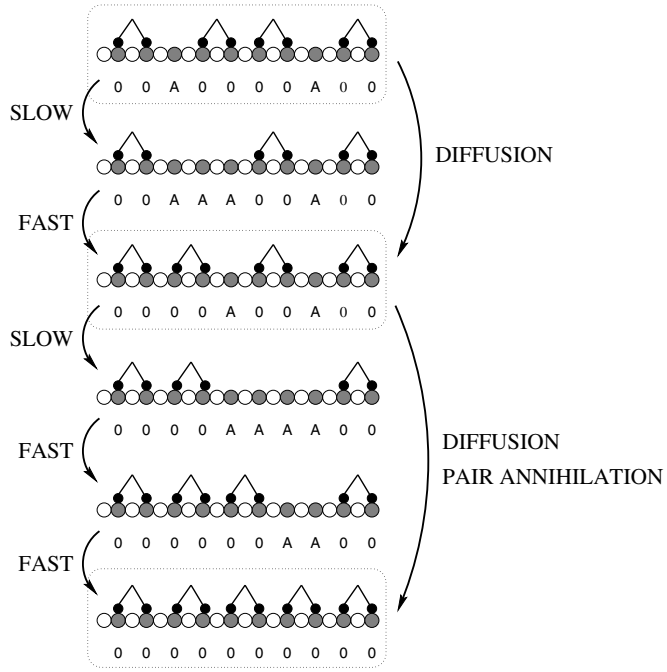

Figure 6.3: Time evolution of a state, consisting of attachment (fast) and detachment (slow) events. The coarse-grained interpretation includes only long-living states (in boxes). The effective steps include diffusion, pair annihilation and pair creation (not shown).

6.2.2 Algebraic decay

The secondary relaxation process towards the final steady state is enormously slowed down. Our simulation shows a broad time domain with a power-law $\propto t^{-1/2}$ instead of a simple exponential decay. To explain this remarkable behavior, we introduce a particle representation in the following way. We denote each vacancy on the lattice as a "particle" A, and each bound dimer as an inert state (00). The detachment of a dimer then corresponds to a pair creation process $00 \to AA$, and the decoration process to pair annihilation $AA \to 00$. Since we consider the limit $K \gg 1$, states with two vacancies A on neighbouring sites have a very short lifetime. We may thus introduce a coarse-grained model by eliminating these states (see Fig. 6.3). Then processes like $A00 \to AAA \to 00A$ (the rate for the first transition is k_- and the branching ratio of the second one 1/2) result in an *effective diffusion* for particle A with a hopping rate to each site

$$r_{\mathrm{hop}} = k_-/2 \tag{6.17}$$

and an effective step width of two lattice sites. There is however one exception from this expression. If the rates with which a particle jumps to the site next to another particle ($A00A \to 00AA$) is $k_-/3$. In the case of nonvanishing diffusion, the explicit diffusion rate (6.11) has to be added to r_{hop}. *Pair annihilation*, $AA \to 00$, occurs very quickly (with a rate k_+c), as soon as two particles have reached two neighbouring sites by means of effective diffusion. *Pair creation*, on the other hand, occurs mainly through the process $0000 \to 00AA \to AAAA \to A00A$. The pair creation rate can be calculated as follows. The first reaction ($00 \to AA$) occurs with a rate of k_- at each pair of lattice sites occupied with one dimer, which makes $k_-/2$ per lattice sites. The probability that a second dimer will detach on either side before the gap gets filled is $2k_-/k_+c = 2/K$. Finally, the branching ratio of the third transition ($AAAA \to A00A$) is 1/3. Therefore the pair creation rate per lattice site is $k_-/3K$ and hence largely suppressed with respect to the annihilation process as long as the particle concentration is far above its steady-state value. Other processes involve more particles and are of higher order in terms of a power series in K^{-1}. They are negligible for $n_A \ll 1$ and $K \gg 1$. A similar mapping has been used by Privman and Nielaba for the description of dimer deposition with diffusion [135].

In summary, for $K \gg 1$, our dimer model can be mapped onto a one-particle reaction-diffusion model $A + A \to 0$. Pair creation processes, $0 \to A + A$, are highly suppressed and do not play any role until the system comes close the steady state. Note that there is a slight difference between this and conventional reaction-diffusion models, namely that particles can only jump over two sites. But, this does not change the behaviour significantly if the average distance between the particles is more than a few lattice sites.

Models like the simple reaction-diffusion model $A + A \to 0$ show interesting nonequilibrium dynamics [25]. Using methods adapted from quantum field theory one can show [97] that asymptotically the particle density $n_A(t)$ decays algebraically, $n_A(t) \propto t^{-1/2}$ which nicely explains the slow decay observed in simulation data (see Fig. 6.1). Note that a mean-field like rate equation approach would predict $n_A(t) \propto t^{-1}$. In our analysis we can even go beyond the asymptotic scaling analysis and try to compare with exact solutions of the model for a random initial distribution with density p by Krebs et al. [92][1] (extending the exact solution for an initially half-filled lattice which was first found by Spouge

[1] We start with Equation (6.27) from [92] and take the limit $L \to \infty$ assuming $p < 1$. We

[149]). They find (adapted to our situation with two-site hopping)

$$n_A(t) = \frac{1}{2\pi} \int_0^2 du \, \frac{\sqrt{u(2-u)}\, p^2 \, e^{-16 u r_{\rm hop} t}}{u \left(u(\frac{1}{2} - p) + p^2 \right)} \; . \tag{6.18}$$

The amplitude for the asymptotic algebraic relaxation has also been determined before by Torney and McConnel [160] for a continuous system and by Lushnikov [102] for a discrete lattice and reads

$$n_A = (32 \pi r_{\rm hop} t)^{-1/2} \; ; \tag{6.19}$$

note that the asymptotic limit is independent of the initial particle concentration in the Flory plateau.

Our Monte-Carlo data (see Fig. 6.1) are in agreement with the predictions of Eq. 6.18. Minor deviations at times between the plateau and the power-law decay are due to the assumption of a random particle distribution underlying the derivation of Eq. 6.18 (the random sequential adsorption process leads to some particle correlations in the intermediate plateau regime) and partly to the fact that we have to deal with two-site hopping.

---

then obtain

$$c(t) = -\frac{1}{2} \int_0^1 d\hat{k} \left(\frac{1}{\frac{1+(1-2p)^2}{2(1-2p)} - \cos(\pi \hat{k})} - \frac{1}{1 - \cos(\pi \hat{k})} \right) \sin^2(\pi \hat{k}) e^{-4Dt\left(1-\cos(\pi \hat{k})\right)}$$

and after the substitution $u = 1 - \cos(\pi \hat{k})$

$$c(t) = \frac{1}{2\pi} \int_0^2 du \frac{\sqrt{u(2-u)}\, p^2 \, e^{-4uDt}}{u \left(u(\frac{1}{2} - p) + p^2 \right)} \; .$$

Finally we set $D = 4\, r_{\rm hop}$ since our particles always jump over two sites. This is, of course, an approximation only valid if the average distance between particles is more than a few sites ($p \ll 1$).

An alternative view would also be possible, namely to introduce a superlattice with double period. In this picture the hopping rate would equal $r_{\rm hop}$ while the particle density would have the double value. We would then obtain

$$n_A(t) = \frac{1}{4\pi} \int_0^2 du \frac{\sqrt{u(2-u)}\, p^2 \, e^{-4 u r_{\rm hop} t}}{u \left(u(\frac{1}{8} - \frac{p}{2}) + p^2 \right)} \; .$$

This approximation contains an overestimate of the annihilation rate (if two particles are three sites apart we use an annihilation rate $2\, r_{\rm hop}$ instead of $4/3\, r_{\rm hop}$) as well as an underestimate (if two particles are on neighbouring sites, but belong to different sites on the superlattice, we use an annihilation rate $2\, r_{\rm hop}$ instead infinity).

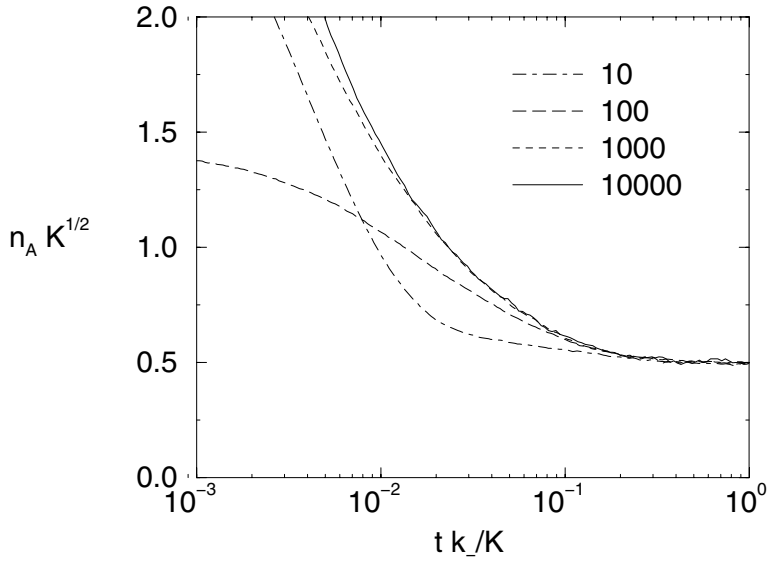

Figure 6.4: The final approach to the steady state becomes scale-invariant in the limit of large K.

6.3 Scale invariance

The results from the $A + A \to 0$ model also become invalid for very long times where the particle concentration comes close to its equilibrium value and the pair creation rate comes into play. Note that in this limit the model becomes scale-invariant. As soon as the particles are far apart from each other, the kinetics of the model should not change upon scaling the particle density $n_A = \alpha\hat{n}$, at the same time scaling the hopping rate $r_{\text{hop}} = \alpha^{-2}\hat{r}$ and the equilibrium concentration, thus $K = \alpha^{-2}\hat{K}$. With these relations, the particle concentration can be written in scaling form (Fig. 6.4)

$$n_A(t) = K^{-1/2}\hat{n}(r_{\text{hop}}t/K) \tag{6.20}$$

with a diverging characteristic time scale $\tau_K \propto K$.

In this sense the ratio K^{-1} of the off-rate to the on-rate acts like an external magnetic field and $K \to \infty$ corresponds to the critical limit (see e.g. Ref. [137, 26]). Note, that contrary to the reversible reaction-diffusion model considered recently by Rey and Cardy [140] there is no conservation law in our model which would make even the terminal approach towards equilibrium algebraic instead of exponential.

6.4 Autocorrelation functions in the steady state

Fig. 6.5 shows an example of the two-time one-point autocorrelation functions of our model in the steady state. Note that there is a difference between the dimer autocorrelation function defined as

$$C_D(\tau) = \left\langle \hat{n}_{(i,i+1)}(t)\hat{n}_{(i,i+1)}(t+\tau)\right\rangle - \left\langle \hat{n}_{(i,i+1)}(t)\right\rangle^2 \tag{6.21a}$$

and the vacancy autocorrelation function

$$C_0(\tau) = \langle \hat{n}_{0_i}(t)\hat{n}_{0_i}(t+\tau)\rangle - \langle \hat{n}_{0_i}(t)\rangle^2 \ . \tag{6.21b}$$

To calculate their initial values, we need the expectation values

$$\left\langle \hat{n}_{(i,i+1)}(t)\right\rangle = \left\langle \hat{n}^2_{(i,i+1)}(t)\right\rangle = n_d = \frac{1}{2}\left(1 - \frac{1}{\sqrt{4K+1}}\right) \tag{6.22a}$$

and

$$\langle \hat{n}_{0_i}(t)\rangle = \left\langle \hat{n}^2_{0_i}(t)\right\rangle = n_0 = \frac{1}{\sqrt{4K+1}} \ . \tag{6.22b}$$

The autocorrelation functions also show several regimes. Both start with a fast (exponential with an offset) decay at the time scale $1/k_+$. This is due to processes in which a dimer detaches and reattaches to the same site. In the limit $K \to \infty$, this effect becomes negligible. After that, the dimer autocorrelation function decays exponentially. The vacancy autocorrelation function shows a second exponential decay with a time constant $1/k_-$, which is the expectation value of the time a vacancy spends on a certain site before it diffuses away. After that it starts approaching the final exponential regime. Except for short time scales, the behaviour of the autocorrelation functions becomes scale invariant for $K \gg 1$. With a scaling as described in previous section, one obtains $C_D(t) = \hat{C}_D(\hat{t})$ and $\tilde{C}_0(t) = \alpha^2\hat{C}_0(\hat{t})$. Thus their scale invariant form reads

$$C_D(t) = \hat{C}_D(k_-t/K) \tag{6.23a}$$

$$C_0(t) = \frac{1}{K}\hat{C}_0(k_-t/K) \tag{6.23b}$$

The scaled correlation functions $\hat{C}_D$ and $\hat{C}_0$ are shown in Fig. 6.6. Although both correlations finally decay exponentially, the vacancy autocorrelation function decays much faster. This can intuitively be understood as follows: the

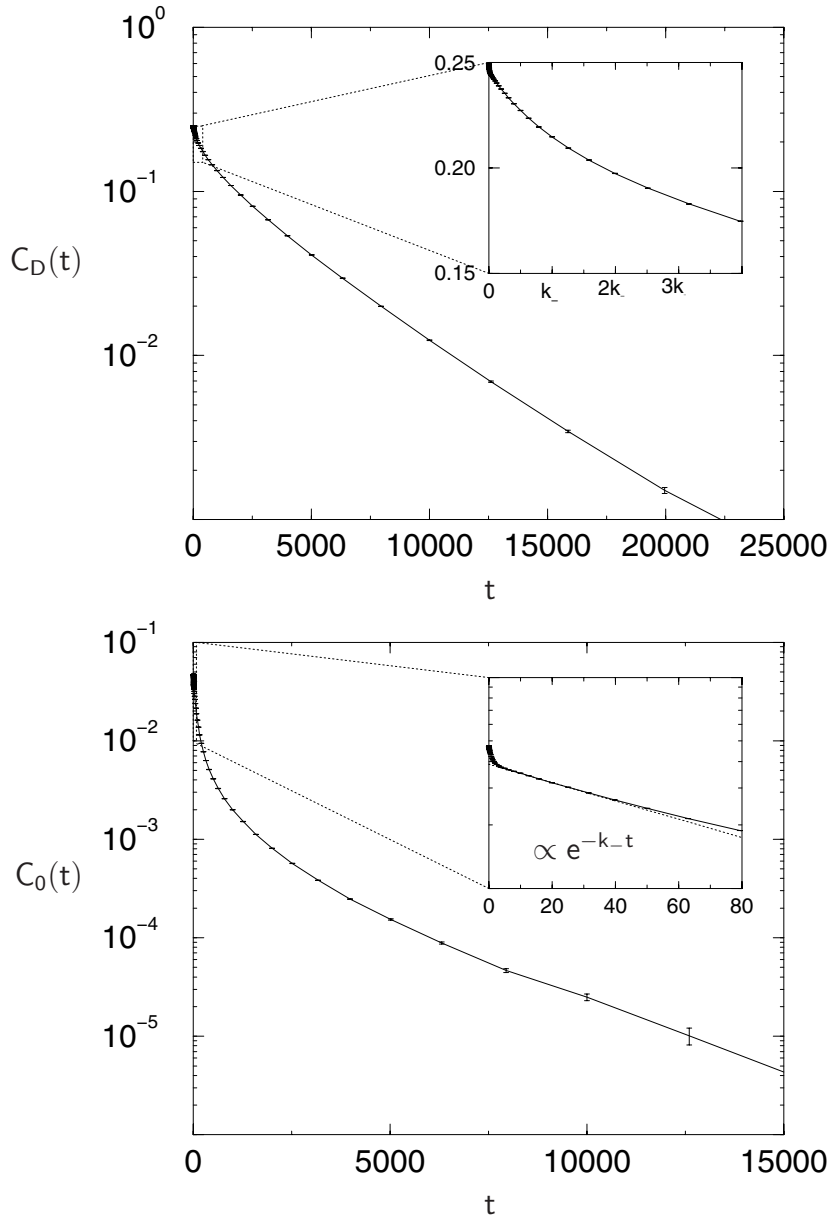

Figure 6.5: Autocorrelation functions of the dimer occupation number $C_D(t)$ (upper) and the vacancy occupation number $C_0(t)$ (lower) for $K = 100$ and $k_- = 0.01$. Data were obtained from a computer simulation on a lattice with 32768 sites and periodic boundary conditions. Error bars indicate the statistical error.

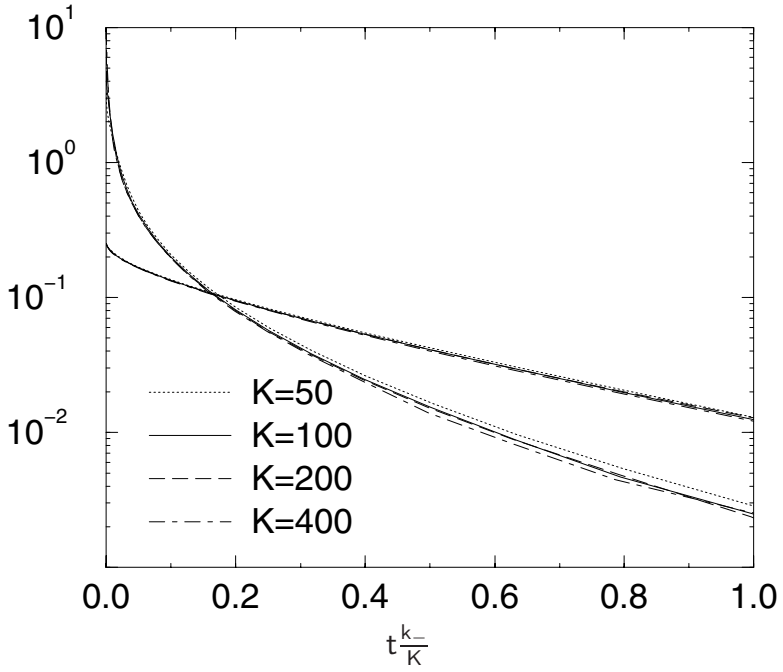

Figure 6.6: Scaled autocorrelation functions $\hat{C}_D(\hat{t}) = C_D(k_-t/K)$ (flatter curves) and $\hat{C}_0(\hat{t}) = KC_0(k_-t/K)$ (steeper curves) for four different values of K. All data were obtained from a simulation on a lattice of length 32768 with periodic boundary conditions. Minor deviations from the scaling law are partly a consequence of a too low K value (50) and partly due to statistical uncertainty in the simulation and finite-size effects.

vacancy autocorrelation function first decays strongly with a rate at which a vacancy jumps to a neighbouring site. Then, at some intermediate timescales, it is dominated by diffusion and thus proportional to $t^{-1/2}$. This regime is only visible for very large K values. At longer time scales, its decay rate is determined by the average lifetime of a vacancy, which is proportional to K/k_-. The decay is exponential in the leading order.

The dimer autocorrelation function, on the other hand, decays as a vacancy passes the observed dimer and thus displaces it by one lattice site. Therefore the dimer autocorrelation function shows no fast decay at short times. Its decay rate (the rate at which vacancies pass by) is also proportional to K/k_-, but the decay itself is slower.

When comparing the autocorrelation functions with those of conventional reaction-diffusion models, care has to be taken because in our model vacancies always jump over two sites and might stay "unobserved" by a correlation function

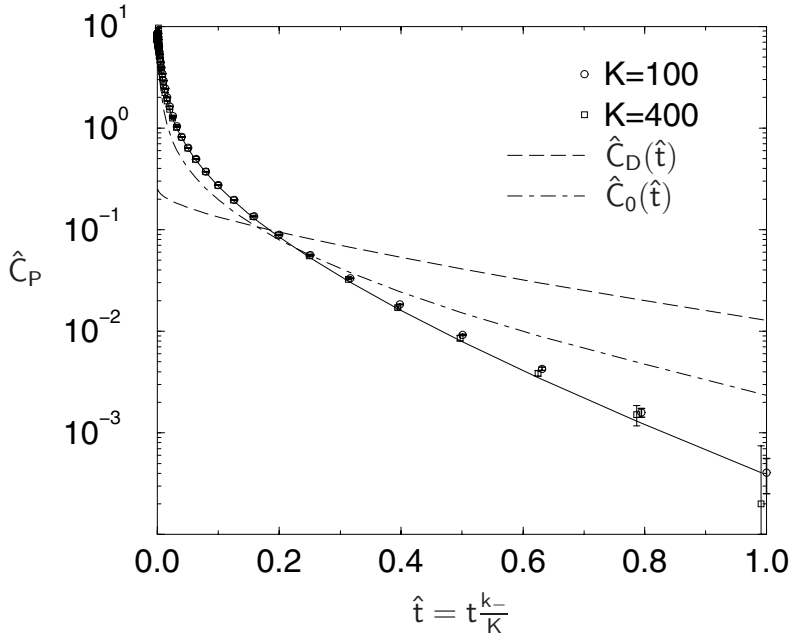

Figure 6.7: Scaled autocorrelation function $\hat{C}_P(\hat{t}) = KC_P(k_-t/K)$ obtained for $K = 100$ and $K = 400$ and compared with the prediction of (6.26) (solid line). Also shown are both scaling functions $\hat{C}_D(\hat{t})$ and $\hat{C}_0(\hat{t})$ from Fig. 6.4.

which looks at a site inbetween. To avoid this effect, we define a third autocorrelation function based on the probability that a vacancy is either on the site i or on the site $i + 1$

$$C_P(\tau) = \left\langle (\hat{n}_{0_i} + \hat{n}_{0_{i+1}} - \hat{n}_{0_i}\hat{n}_{0_{i+1}})(t) \times (\hat{n}_{0_i} + \hat{n}_{0_{i+1}} - \hat{n}_{0_i}\hat{n}_{0_{i+1}})(t+\tau) \right\rangle - \left\langle (\hat{n}_{0_i} + \hat{n}_{0_{i+1}} - \hat{n}_{0_i}\hat{n}_{0_{i+1}})(t) \right\rangle^2 . \quad (6.24)$$

In the second term we can use

$$\left\langle \hat{n}_{0_i} + \hat{n}_{0_{i+1}} - \hat{n}_{0_i}\hat{n}_{0_{i+1}} \right\rangle = \frac{2n_0}{1+n_0} = \frac{2}{\sqrt{4K+1}+1} . \quad (6.25)$$

The function C_P is shown in Figure 6.7 and decays even faster than the single-site autocorrelation function C_0. Its scaling form can be obtained from the article

by Bares and Mobilia [11] and reads[2]

$$\hat{C}_P(\hat{t}) = \left(\frac{e^{-2\hat{t}}}{\sqrt{2\pi\hat{t}}} - \operatorname{Erfc}\sqrt{2\hat{t}} \right) \operatorname{Erfc}\sqrt{2\hat{t}} \,. \tag{6.26}$$

For $\hat{t} \gg 1$ (not shown in the graph) we may use the asymptotic expansion of the error function

$$\operatorname{Erfc}\sqrt{x} \approx \frac{e^{-x}}{\sqrt{\pi x}} \left(1 - \frac{1}{2x} + \dots \right)$$

and obtain

$$\hat{C}_P(\hat{t}) \approx \frac{1}{8\pi\hat{t}^2} e^{-4\hat{t}} \,. \tag{6.27}$$

6.5 Beyond the stiff dimer model

6.5.1 $K_1 c \gg 1$

By now we have studied the limit $K_1 c \to 0$ and $K_2 \to \infty$, which simplified our model to the stiff dimer model. As one can see from the symmetry arguments given in Sect. 5.3, the case $K_1 c \to \infty$ with $K_2 \to \infty$ is completely equivalent if one interchanges the dimers bound with one head and empty lattice sites. The only difference arises from the initial condition, which is an empty lattice in both cases (it should be occupied with single-bound dimers if we wanted to have the truly mirrored situation).

The initial decoration runs similarly as in Sect. 6.2.1. If the rates obey $k_{2+}^f \gg k_{1+}c$ and $k_{2+}^b \gg k_{1+}c$, while the diffusion rate is still comparatively slow, $r_d \ll k_{1+}c$, the case of strong diffusion applies and the concentration of single-bound dimers on the Flory plateau is $n_1 \cong 0.1233$.

If, however, the attachment rate of the second head disappears on one side, e.g. $k_{2+}^f \gg k_{1+}c \gg k_{2+}^b$, we get a different situation. A dimer which bounds with its first head on an the front end of a vacant interval remains bound on one head, since the second head is not able to bind to the site behind the first one.

[2] The scaling function of $C_P(\tau)$ can be obtained from Eq. (81) in Ref. [11]. There we have to set $r = 0$ (one-point correlation function) and $t \to \infty$ (steady state). Then only the second term in the sum remains. Since we are interested in the scaling regime, we only consider the leading term in the limit $J/D \to 0$. The corresponding parameters are $D \equiv k_-/2$, $2D/J \equiv K$ and $\rho = \sqrt{J/2D} \equiv 1/\sqrt{K}$.

Therefore, the defect concentration on the Flory plateau increases drastically. In the following, we give a derivation.

Let $P_l(t)$, $l \geq 1$ denote the number of undecorated intervals of length l per lattice site. Since at the beginning the lattice is (almost) empty, the normalisation reads $\sum_l l P_l(0) = 1$. Then the rate at which new pairs attach to each pair of places inside an empty interval is $k_{1+}c$. With the same rate dimers attach to the foremost site of an empty interval and remain bound on one head. Our task is to calculate their concentration at the time when there are no empty sites left.

The rate at which intervals of length l are being destroyed is $lk_{1+}c$. The rate at which intervals of length $l+2$ get shortened to length l is $2k_{1+}c$ and the rate at which those of length $l+1$ get shortened to length l is $k_{1+}c$. Finally the rate at which intervals of length $l+2+m$ get divided into one interval of length l at the left and one interval of length m at the right equals $k_{1+}c$ and so does the rate for the mirrored situation. These terms constitute the Master-equation for the time evolution of P_l

$$\frac{d}{dt}P_l = r\left(-lP_l + P_{l+1} + 2\sum_{m=0}^{\infty} P_{l+2+m}\right) \tag{6.28}$$

Let further S denote the number of single-bonded dimers. They appear when a dimer attaches to the foremost site of any empty interval. Thus the time evolution of S is given as

$$\frac{d}{dt}S = r\sum_{l=1}^{\infty} P_l \tag{6.29}$$

The first Master equation can be solved using the ansatz

$$P_l(t) = p(t)a(t)^l \tag{6.30}$$

leading to two differential equations for p and a

$$\frac{1}{k_{1+}c\,a}\frac{da}{dt} = -1 \tag{6.31a}$$

$$\frac{1}{k_{1+}c\,p}\frac{dp}{dt} = a^2\left(1 + \frac{2}{1-a}\right) . \tag{6.31b}$$

They can be substituted to

$$\frac{1}{p}\frac{dp}{da} = -\frac{1+a}{1-a} . \tag{6.32}$$

At the beginning the intervals are very long, thus $a(t=0) \to 1_-$. The normalisation at that point states $p(t=0)/(1-a(t=0))^2 = 1$. This boundary condition leads to the solution of (6.32)

$$p(a) = (1-a)^2 e^{a-1} \; . \tag{6.33}$$

Equation (6.29), together with (6.31a) gives

$$\frac{dS}{da} = -\frac{p}{1-a} = -(1-a)e^{a-1} \tag{6.34}$$

and thus

$$n_1 = S(t=\infty) = S(a=0) = \int_0^1 (1-a)e^{a-1} da = 1 - 2e^{-1} \cong 0.2642 \; . \tag{6.35}$$

6.5.2 $K_1 c \approx 1$

A third case arises if we consider the limit $K_2 \to \infty$ with $K_1 c$ being of the order of magnitude 1. In this case neither the dimers bound with one head nor the empty lattice sites dominate and we have to introduce two particle types. As we are used to, particles A should denote vacancies on the lattice. In addition, we introduce particles B, representing dimers bound with only one head.

Reactions $A \to B$ and $B \to A$ occur at rates $k_{1+}c$ and k_{1-}. If we assume that both attachment rates of the second head k_{2+}^f and k_{2+}^b are significantly higher than $k_{1+}c$ and k_{1-}, we are again dealing with the limit of *strong diffusion*, similar as described in Sect. 6.1.1. The diffusion mechanism for vacancies (particles A) is exactly the same as in the model with stiff dimers and according to (6.11) the hopping rate obeys

$$r_d = \frac{k_{2+}^f k_{2+}^b}{K_2(k_{2+}^f + k_{2+}^b)} \; . \tag{6.36}$$

The diffusion rate of single-bonded dimers (particles B) has to be equal. This is due to the symmetry of our model upon exchanging particles A and B and at the same time the transition rates $k_{1+}c$ and k_{1-} (Sect. 5.3) and because the hopping rate does not depend on $k_{1+}c$ and k_{1-}. If a particle A and a particle B reach neighbouring sites, they annihilate quickly, while two particles of the same type do not disturb each other. To summarise, we obtain a reaction diffusion model of the type:

$$A \leftrightarrow B$$
$$A + B \leftrightarrow 0$$

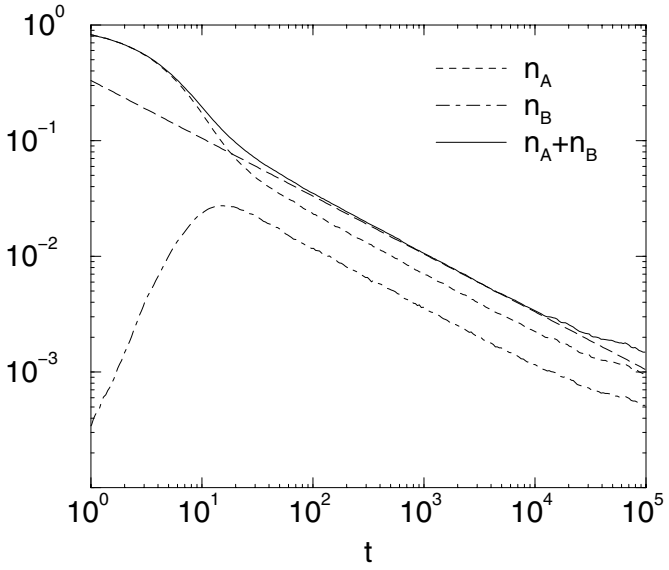

Figure 6.8: A computer simulation showing the time dependence of the vacancy (n_A) density, the single-bonded dimer (n_B) density and their sum for $K_1 c = 0.5$ and $K_2 = 10^6$. The long dashed line shows the predicted long-time limit of reaction-diffusion models given by Eq. (6.19). In detail, parameters are: $k_{1+}c = 0.1$, $k_{1-} = 0.2$, $k^f_{2+} = 10^6$, $k^f_{2-} = 1$, $k^b_{2+} = 0.1\, k^f_{2+}$ and $k^b_{2-} = 0.1\, k^f_{2-}$. The simulation has been performed on a lattice with 16384 sites and periodic boundary conditions.

While its dynamics is more complex at short times, the model becomes equivalent to the $A+A \leftrightarrow 0$ if the transitions between A and B become faster than the typical annihilation time, which is given as the diffusion time between two particles, displaced by the average distance between particles on the lattice, $\sim \frac{1}{r_{\mathrm{hop}} n^2}$. Therefore the power-law behaviour, given by (6.19) remains untouched by the fact that we are dealing with two different particle types. An example of a simulation in this regime is shown in Fig. 6.8.

Chapter 7

Model with interaction

Thus far we have assumed that there is no interaction between attached dimers, except for the fact that each binding site can be occupied at most by one head. However, in some cases there is strong experimental evidence for the existence of an attractive interaction [159]. Observation of two-dimensional crystalline ordering could hardly be explained without a lateral interaction between protofilaments. Observation of coexisting decorated and undecorated domains on microtubule sheets also implies the existence of a longitudinal interaction [109], leading to a phase-transition.

We model this interaction as follows: The presence of a head on the neighbour site which acts attractively shifts the attachment and the detachment rate of the observed head by factors A_i and B_i such that

$$k_{1,2+}^{\text{with neighbour}} = A_i \, k_{1,2+}^{\text{without neighbour}} \qquad k_{1,2-}^{\text{with neighbour}} = B_i \, k_{1,2-}^{\text{without neighbour}}$$

According to the principle of detailed balance, the interaction potential can be expressed through the factors A_i and B_i in the following way

$$J_i = k_B T \ln \frac{A_i}{B_i} \, . \tag{7.1}$$

A_i, B_i and J may be different for different constellations like longitudinal, transverse between two parallel dimers, transverse between a dimer with one attached head and one with two etc.. In most further calculations we will assume that the interaction influences the attachment rate by the same factor as the detachment rate, thus $B_i = 1/A_i$. Of course, this assumption is irrelevant for determining the equilibrium state, since the latter only depends on the interacting potential J and not on the single rates.

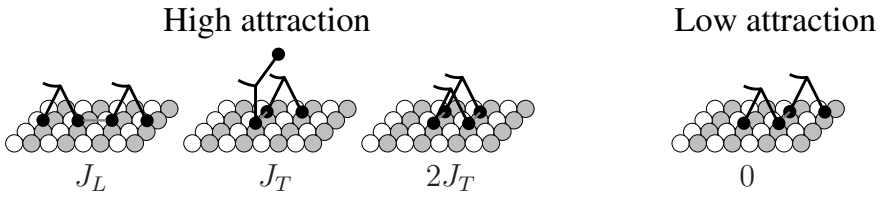

Figure 7.1: The interaction potential between two adsorbed kinesin molecules in different states and positions. We assume a longitudinal attraction J_L (independent of the second head) and a transverse attraction J_T, which acts always between two parallel heads on adjacent protofilaments except if they belong to two dimers displaced by one binding site (the rightmost pair in the figure). In the latter case we assume the interaction to be zero.

Even when assuming only nearest neighbour interaction, a general description would require 12 different constants giving the interaction strength between different states in different relative positions. Assuming a lateral symmetry, thus neglecting the fact that the lattice on tubulin is not orthogonal, reduces their number to 9.

Since this is still too many for a general treatment, we use a simplified model instead by introducing only two different interaction constants, a longitudinal and a transverse one (Fig. 7.1). This simplified description turns out to be sufficient to explain the essential experimental observations such as two-dimensional ordering and segregation of empty and decorated domains. The longitudinal interaction constant is denoted by J_L and acts always between two heads on neighbouring sites of the same protofilament. The transverse interaction has the strength J_T and acts between two heads attached on neighbouring sites of two protofilaments. Since the model has to explain the experimentally observed lateral ordering [159], binding of a dimer out-of-phase with the decoration on the neighbouring protofilament should be energetically less favoured than binding in-phase. In terms of our simplified description, we assume the interaction between two dimers attached on adjacent protofilaments and shifted by 8nm to be zero.

Computer simulation results for stoichiometry curves with different interaction strengths are shown in Figure 7.2. The interaction changes the form of the stoichiometry curves. If the interaction is stronger than its critical value, one can see the trace of a phase transition, somewhat smeared because of the finite size of the system. This phase transition explains the observed phase segregation at low kinesin concentrations. In the following we will estimate the interaction strength necessary for the existence of the phase transition and the solution concentration

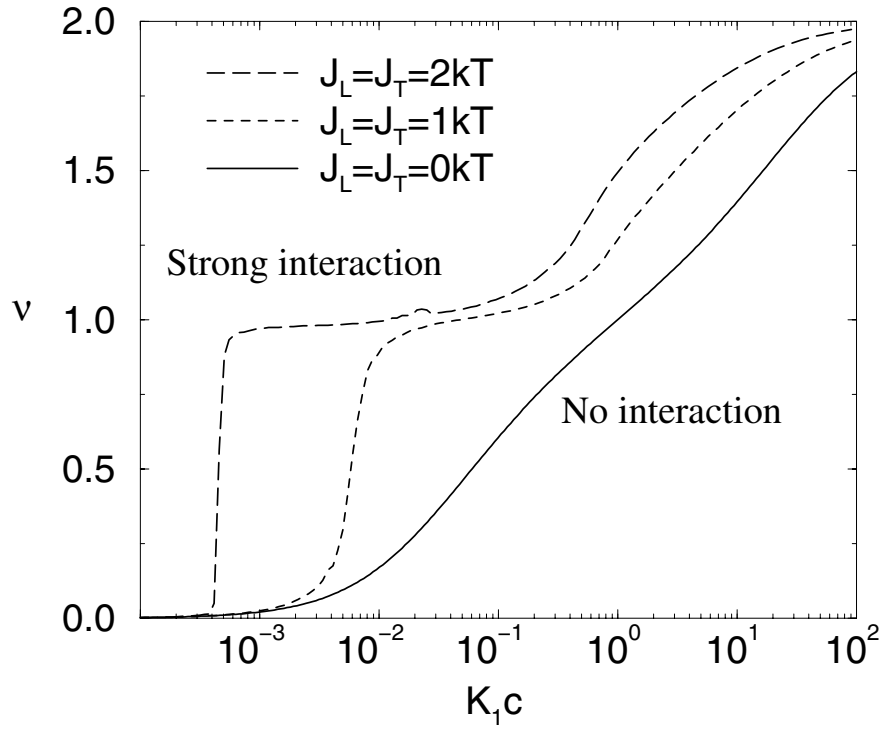

Figure 7.2: Binding stoichiometry (heads per binding site) for $K_2 = 10$ and three different values of the interaction strength $J_L = J_T = 0,\ 1$, and 2 kT. The curves for nonvanishing interaction were obtained from a computer simulation on a lattice with 100×14 sites.

at which it occurs.

7.1 The monomer model

The most instructive way to understand the phase transition between the empty and the decorated phase is to look at the simple monomer binding model, also called lattice gas model. Such models have been widely used to describe the adsorption of atoms on crystal surfaces. For simplicity we assume an isotropic interaction, having the same strength in longitudinal and lateral direction, although the final result applies for an anisotropic interaction as well.

Without interaction with the neighbours, the ratio of transition rates between an empty and an occupied state is given as Kc, where K is an effective reaction constant and c the solution concentration. The transitions can thus be described by an energy gap $\epsilon = k_B T \ln(Kc)$. Of course, this is just an effective energy

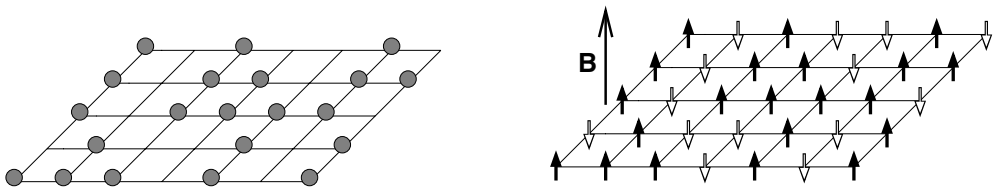

Figure 7.3: The monomer adsorption model, also known as lattice gas model, compared with the Ising model.

which actually corresponds to the Gibbs free energy and is much lower than the real binding energy, since it also contains entropic contributions. Two adsorbed molecules on nearest neighbour sites attract themselves with a binding potential J. The Hamiltonian of the system reads

$$\mathcal{H} = -J \sum_{\langle ij \rangle} n_i n_j - \epsilon \sum_i n_i \ , \tag{7.2}$$

where $\langle ij \rangle$ runs over all pairs of nearest neighbours. n_i is 1 for occupied sites and 0 for empty sites. In this form the model can be mapped onto a two-dimensional Ising model, whose Hamiltonian reads

$$\mathcal{H} = -J' \sum_{\langle ij \rangle} s_i s_j - \epsilon' \sum_i s_i \ . \tag{7.3}$$

The variables s_i have the value 1 for the state with spin parallel to the magnetic field ($\uparrow$) and -1 for the state with antiparallel spin ($\downarrow$). The transformation which maps both models to each other reads

$$s_i = 2n_i - 1 \qquad J' = \frac{1}{4} J \qquad \epsilon' = \frac{\epsilon}{2} + J \ . \tag{7.4}$$

The critical temperature of the two dimensional Ising model was first determined by Kramers and Wannier[1] [91]. In the absence of external field, the model has also been exactly solved by Onsager [126]. The resulting critical temperature is $k_B T_c = 2.269 J'$, or

$$J_c = 1.76 \, k_B T \ . \tag{7.5}$$

[1]The publication was submitted in 1941 as Kramers was in Holland and Wannier in Texas. It starts with a footnote "Owing to communication difficulties, one of the authors (G.H.W.) is entirely responsible for the printed text."

This result indicates that the attraction between adsorbed molecules has to be at least J_c in order to allow for a phase transition. The result also remains valid if the longitudinal and lateral interaction differ [126]. In this case the critical point is given as

$$\sinh \frac{J_L}{2k_BT} \times \sinh \frac{J_T}{2k_BT} = 1 \; . \tag{7.6}$$

The exact solution helped us to determine the critical point, i.e. the interaction strength needed to obtain a phase transition between an empty and a decorated state. The full form of the binding stoichiometry as a function of concentration, however, would be equivalent to calculating the magnetisation of the two-dimensional Ising model in the presence of an external field, which has not yet been done analytically. Therefore one has to rely on computer simulations to obtain the stoichiometry curves. An overview on Monte-Carlo simulations on lattice gas models can be found in [16]. The situation simplifies when one is far away from the critical point, i.e. when the coupling is much stronger than its critical value, $J \gg J_c$. This corresponds to the low-temperature limit in the Ising analogue, where the spin polarisation is always complete and points into the direction of the external field. The number of spins with orientation $\uparrow$ is given as $n = N\Theta(\epsilon')$. Back in the adsorption model, according to (7.4), the condition reads

$$\nu = \Theta(\epsilon + 2J) \; . \tag{7.7}$$

This expression can also easily be understood directly. The decoration is complete if an edge with two bound neighbours is stable and vanishes otherwise. Deviations from (7.7) can occur due to finite sized boundary conditions. The finite-size effect always lowers the number of bound molecules compared to the model on an infinite lattice.

The phase transition explains why decorated and empty microtubules can coexist beside each other. The situation is analogue to the liquid-vapour transition of a fluid. Then the binding stoichiometry corresponds to the density and the solution concentration to the pressure. At temperatures below the critical point, the liquid and the gaseous phase will coexist in a vessel if the amount of fluid lies within a certain range. Note that coexistence of empty and decorated microtubules is only possible in a finite system in which the solution concentration of kinesin also depends on the amount of adsorbed kinesin.

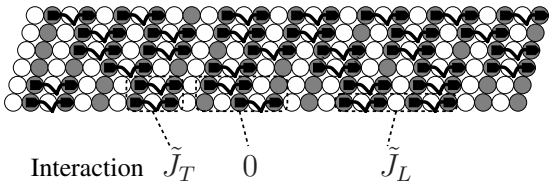

Figure 7.4: In the limit of large K_2 dimers always attach to the microtubule with both heads bound to two neighbouring sites on the same protofilament (we call this case the stiff dimer model). Two dimers are attracted with binding energy $\tilde{J}_L$ when binding next to each other on the same protofilament and with $\tilde{J}_T$ when attached beside each other on two adjacent protofilaments. We assume that there is no interaction between dimers attached on adjacent protofilaments if they are shifted by one lattice period (8nm).

7.2 Stiff dimer model

The simplest monomer adsorption model has allowed us to explain qualitatively and quantitatively the occurrence of the phase transition if the interaction is sufficiently strong. The next question is whether this state really shows two-dimensional crystalline ordering. These questions can be best studied on a simplified dimer binding model as introduced in Sect. 7.2. It differs form the monomer model in the way that it takes into account the dimeric nature of kinesin, however it assumes for simplicity that a dimer can bind only with both heads at the same time, corresponding to the limit limit $K_2 \gg 1$. We also restrict to the nondiffusive case, as described in Sect. 6.1.2. The parameters of the stiff dimer model can be derived from the original parameters as follows

$$\tilde{K} = K_1 K_2 \tag{7.8a}$$

$$\tilde{J}_L = J_L \tag{7.8b}$$

$$\tilde{J}_T = 2J_T \; . \tag{7.8c}$$

The interacting stiff dimer model is essentially a special case of the Axial next nearest neighbour interaction (ANNNI) model (for a review written by W. Selke see [146]), Fig. 7.5. However, here we have an infinite repulsion between nearest neighbours in longitudinal direction and an attraction between next nearest neighbours in longitudinal direction and between nearest neighbours in lateral direction. In ANNNI models, usually the opposite situation was studied since it leads to frustrations, while the zero-temperature state of our model is trivial.

Examples of stoichiometry curves of the dimer binding model with several interaction constants in a system of realistic size are shown in Figure 7.6. They are

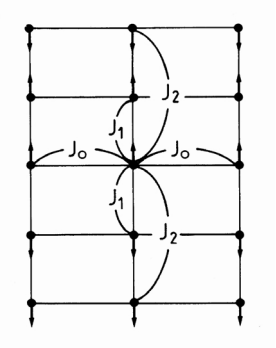

Figure 7.5: The definition of coupling constants in the ANNNI model from Ref. [146]. Our model corresponds to the situation with $J_0 \equiv \tilde{J}_T$, $J_1 = -\infty$ and $J_2 \equiv \tilde{J}_L$.

compared with the results of the monomer model. One can see that the difference between the monomer and the stiff dimer model decreases with increasing interaction. Above the critical interaction strength the equilibrium state also shows crystalline ordering in both directions (Fig. 7.7).

An explanation for the coexistence of empty and decorated domains has already been given using the monomeric model. The dimer model does not differ significantly from the monomer model in this point, however the parameters differ, since we have $\tilde{J}_T = 2J_T$ (the transverse attraction becomes twice as strong since it acts between two pairs of heads). The higher transverse interaction is one possible explanation why cooperative binding has only been observed with dimeric kinesin. Another possibility would be that the interaction is mediated by structural changes in tubulin, which only occur among bound dimers.

7.3 Nucleation

Thus far, we have shown when the equilibrium state contains homogeneous, defect-free decoration. There are, however, different ways how the equilibrium state is reached in an experiment starting with an empty tubulin plate. In the analogue Ising model, this would correspond to a sudden change in the external magnetic field from, e.g. $-\infty$ to a finite value.

The phase transition from the empty to the decorated state has to go through the process of nucleation. Before the decoration starts, the microtubules are always in the empty state. Then the kinesin concentration increases rapidly to the value c and the empty state becomes metastable. The transition to the stable state in which the microtubules are almost entirely decorated can occur after a cluster of adsorbed molecules has reached a critical size. Since the decorated area grows by extension of a single nucleus, it can form a regular lattice along

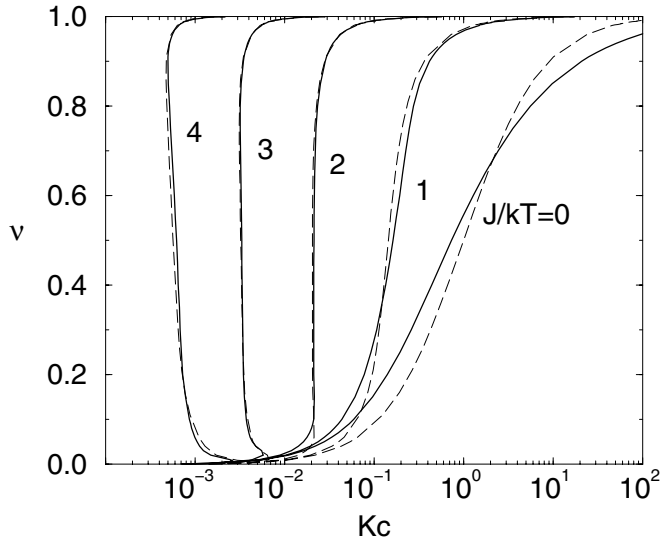

Figure 7.6: Binding stoichiometry (ν heads per lattice site) of stiff dimers as a function of the solution concentration c for different interaction constants $\tilde{J}_L = \tilde{J}_T = J$. Data were obtained from a computer simulation on a limited 14×100 lattice. For each data point, the number of adsorbed dimers was held constant during the simulation as the average concentration needed to maintain this number was calculated. When the concentration is held constant in an experiment, only the upper and the lower limb of the hysteresis are (meta-) stable. The dashed curves show the same quantity for a monomer model on a 14×50 lattice, which is equivalent to the Ising model.

the entire microtubule with 16 nm longitudinal periodicity. Single-site nucleation can thus provide an explanation for a homogeneous decoration over the whole microtubule, reached in a comparatively short time. The process of nucleation in surface adsorption has been studied by Becker and Döring [14]. A review can be found e.g. in [100].

Single-site nucleation can provide an explanation for homogeneous decoration over the whole microtubule, reached in a comparatively short time. If the nucleation time, i.e. the time needed before a nucleus appears is longer than the time a nucleus needs to grow over the surface, there is a good chance that the whole surface will be decorated from one nucleus and thus homogeneously. On the other hand, if a second nucleus appears before the first one is able to cover the surface, they can be out of phase (shifted by 8 nm) and thus a domain wall appears between them. The defects can be healed when these domain walls diffuse around and annihilate, similar as defects in the one-dimensional model (Chapter

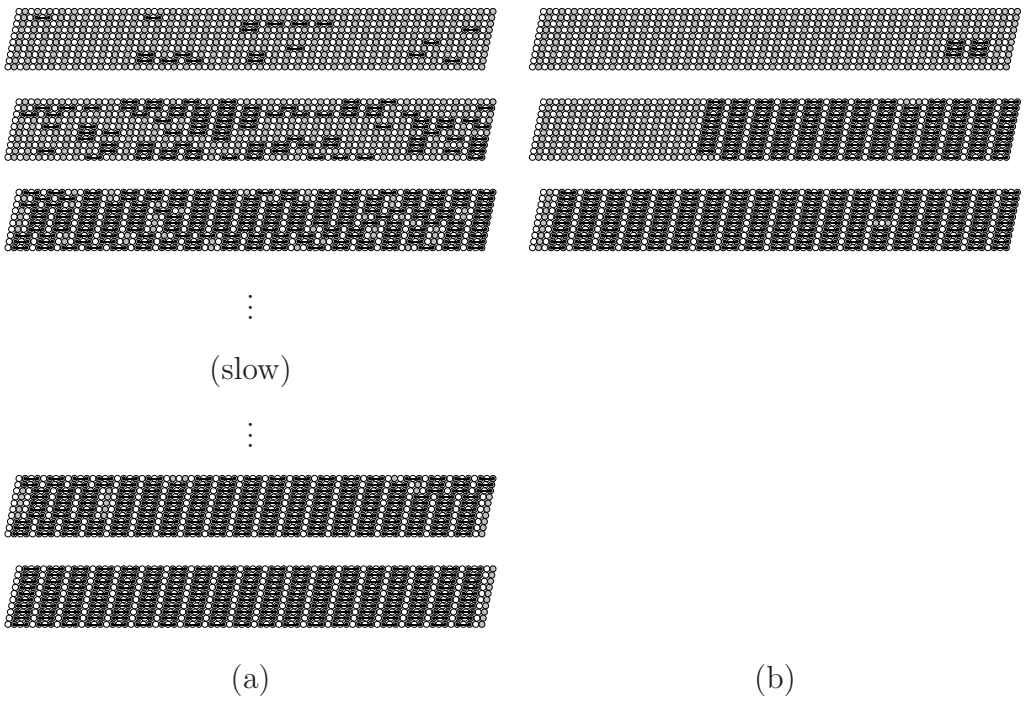

Figure 7.7: Computer simulation of multiple-site nucleation with subsequent annealing (a) and single-site nucleation (b). Both can lead to defect-free decoration. However, annealing can be extremely slow whereas single-site nucleation immediately leads to the ordered state.

6), but much slower. We will refer to this process as *annealing*. Both processes are compared in Fig. 7.7.

In the following we give a criterion on when to expect nucleation with a single nucleus which immediately leads to the ordered state. In general, we have to estimate the nucleation time t_{nuc} (the average time before a critical cluster appears) and the growth time t_{growth} a cluster needs to cover the whole surface. The criterion for nucleation with a single nucleus then reads

$$t_{\mathrm{growth}} \lesssim t_{\mathrm{nuc}} \; . \tag{7.9}$$

An analytical expression for the nucleation time can easily be given if the interaction is strong enough, and the critical cluster size becomes as small as 4, 3 or 2 molecules [14, 100]. However, we are mainly interested in giving a lower limit on interaction that is necessary to obtain a defect-free decoration, so that the nucleation clusters we are dealing with are larger. Therefore we use a computer simulation to determine parameter ranges for homogeneous and for inhomogeneous decoration. The results are shown in Fig. 7.8. Homogeneous decoration

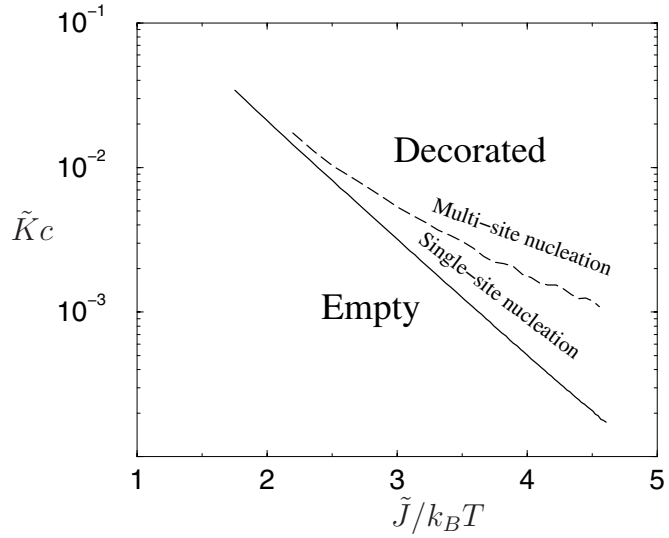

Figure 7.8: Phase diagram: The solid line shows the phase transition above which a decorated phase exists. The dashed line shows the border between homogeneous (defect-free) decoration reached immediately through nucleation and decoration with domain walls. The curves were obtained from a computer simulation on a lattice of 14×100 fields. $\tilde{J} = \tilde{J}_L = \tilde{J}_T$ was assumed. The upper line was determined by the following algorithm: Starting with an empty field, the simulation was being run until 90% of the field was decorated. If less than 5% of the field is decorated out of phase, the field is considered as homogeneously decorated. The line shows where the probability of homogeneous decoration drops below 50%.

is reached quickly through the process of single-site nucleation in the parameter range between both lines. In a realistic situation the kinesin concentration in solution drops during the decoration. If we are dealing with a 2-fold exceed on kinesin, the concentration will drop to half of its initial value. Therefore we estimate that the single-site nucleation has to be dominant at concentrations twice as high as at the phase transition. From Fig. 7.8 we therefore estimate the interaction needed to obtain monocrystalline ordering by single-site nucleation as $J \approx 3k_BT$. A further important implication of our model is that defect-free decoration is most probable at concentrations just above the phase transition (the threshold for decoration).

Nucleation is also essential for the occurrence of coexisting empty and decorated domains at sub-stoichiometric concentrations. If the nucleation is faster than the growth of the nuclei (multiple-site nucleation), the decoration will start at many microtubules in parallel. After some time, as an increasing amount of kinesin gets bound, its concentration in the solution drops and the growth of

decorated domains slows down until some equilibrium concentration is reached. After this initial phase, decorated domains are distributed over all microtubules. Then the smaller domains will loose their size on average while the bigger ones will grow, until the state with segregated phases is reached after some long time.

On the other hand, single-site nucleation leads to the occurrence of coexisting empty and decorated microtubules immediately. When a nucleus appears on one microtubule, it quickly covers its surface. This process can repeat on other microtubules until the concentration drops below the value at which the nucleation is possible.

How can one recognise in an experiment, which mechanism has lead to ordered decoration? One possibility would be to investigate the sheets in dependence of the time past since the beginning of the decoration. If the ordering is due to annealing, then the number of defects should decrease with the duration of the experiment. In the case of single-site nucleation, there should not be a significant difference. The other possibility would be to look at the form and distribution of decorated domains under sub-stoichiometric conditions. While annealing leads to round-shaped decorated domains on many plates, single-site nucleation causes some sheets to be filled up to the edges and others not at all. Finally, a prediction of the single-site hypothesis is that the probability to get defect-free decoration lowers with increasing kinesin concentration.

Chapter 8

Summary and outlook

To summarise, in this work we have studied cooperative behaviour of biological molecular motors. The first part is dedicated to the dynamical behaviour of active molecular motors.

In Chapter 2 we introduced a simple two-state power-stroke model and discussed its force-velocity relations. The essential component of the model is the form of the detachment rate as function of mechanical strain. Depending on it, we have shown that the model can show a much greater variety of phenomena than previously discussed. Simple forms of the detachment rate have been shown to lead to linear, hyperbolic, or non-monotonic force-velocity relations. We have derived an analytical criterion for the occurrence of non-monotonic relations which can lead to oscillations or wave generation in appropriate setups.

In Chapter 3 we investigated the influence of the backbone elasticity on the operation of motors. The elastic coupling makes the usual mean-field approach invalid and we have to take into account correlations between the position of a motor and the state of its neighbours. In the simplest case of strain-independent reaction rates we have shown exactly that the backbone elasticity does not influence the zero-load velocity, but it decreases the stall force. This decrease has been determined using different analytical approximations and compared with computer simulations. Applied to muscles, we have shown that their components are just stiff enough to keep losses caused by this effect low. But we expect the elasticity to become important in newer in vitro experiments. We have also discussed the finite-size effects in a system of elastically coupled motors. The force-velocity curve of a finite system depends on whether it is determined for a constant force or for a constant velocity. We have shown that in the first case a

finite system is less efficient than an infinite one, whereas in the second case a finite system becomes more effcient than an infinite one.

In Chapter 4 we have combined an anomalous force-velocity relation with an elastic backbone and shown that it can lead to propagating waves. Using a local mean-field approximation we have derived the scaling properties of these waves. We have shown that our model essentially describes the situation found in flagella.

In the second part we have studied the cooperative behaviour of passive motors, lacking an energy source like ATP. This part is motivated by decoration experiments frequently used in biophysical chemistry. In Chapter 5 we have introduced a general binding scheme for non-interacting dimers. We proposed that dimer can either bind with one head to one lattice site or with both heads on two adjacent sites. We have identified the symmetry properties of this model and determined its equilibrium configuration using combinatorial methods. The resulting expression for the binding stoichiometry helps improving the interpretation of experimental data.

In Chapter 6 we investigated the limit in which the dimers are likely to bind with both heads (stiff dimer model). First we discussed how the parameters of the stiff dimer model derive from the original parameters. We then investigated the relaxation from an initial state far from equilibrium. We have found a two-stage relaxation. In limiting cases we could map it to known models for random sequential adsorption (RSA) and reaction-diffusion models. Using Monte-Carlo simulations we have also determined the autocorrelation functions in the steady state and compared them with available analytical results.

In Chapter 7 we have extended our model by introducing an attractive interaction. We have investigated the question whether this interaction can lead to coexistence of empty and decorated domains and to two-dimensional crystalline ordering. We have also investigated whether the ordered state can be reached within a short time after the beginning of the decoration. We have shown that nucleation from a single nucleus explains both the periodic order and the coexistence of empty and decorated domains. The results have been used for the interpretation of decoration experiments with dimeric kinesin on microtubules.

The thesis has also shown that some questions remain open for future work. In Chapter 2 we have discussed how the strain-dependent detachment rate in a two-state model can lead to anomalous force-velocity relations. It would be interesting to know what other mechanisms (maybe in a model with more states)

can do the same. Also, the two-state model is only able to explain the basic properties of kinesin but fails on many details. We expect that a model with four chemical states will give a coherent explanation of the present experimental findings. Finally, we expect that the generalisation of our dimer-adsorption model to other systems, especially tropomyosin on actin, will provide experimentally relevant and verifiable results on relaxational dynamics.

Glossary

Actin Protein that forms fibres which support the shape of a cell and serve as a track for molecular motors (myosin). It is a major component of muscle cells and of the cytoskeleton. Actin can be found in the globular (dissolved) form, called G-actin, or in the polymerised form, called F-actin. Polymerised actin forms a double-helix with a half-pitch of about 36 nm. It has a defined polarity in the sense that one can distinguish between the so called + and the − end.

ADP Adenosine diphosphate, product of ATP hydrolysis.

AMP-PNP (Adenosine monophosphate)–P–N–P; an ATP substitute with a nitrogen atom between the phosphate groups, which makes it non-hydrolysable. It is widely used for studying intermediate states of motor molecules (those between the ATP binding and its hydrolysis). In the case of kinesin, it also tightens its binding to tubulin [31].

ATP Adenosine triphosphate, the major energy source in biological processes. It is built up of an adenine unit, followed by a ribose and three phosphate groups. Breaking the bindings between the phosphate groups releases a large amount of energy. The reaction reads [173]

$$\mathrm{A} + \mathrm{ATP} + \mathrm{H_2O} \rightarrow \mathrm{B} + \mathrm{ADP} + \mathrm{P_i} + \mathrm{H^+}$$

(in this case the energy was used to transform A into B). $\mathrm{P_i}$ denotes the inorganic orthophosphate. The equilibrium concentrations obey

$$\frac{[\mathrm{B}]}{[\mathrm{A}]} = e^{-\Delta G/RT}$$

with

$$\Delta G = \Delta G^0 + RT \ln \frac{[\mathrm{ADP}][\mathrm{P_i}][\mathrm{H^+}]}{[\mathrm{ATP}][\mathrm{H_2O}]} = \Delta G^{0\prime} + RT \ln \frac{[\mathrm{ADP}][\mathrm{P_i}]}{[\mathrm{ATP}]}$$

Under standard conditions (pH 7) the free energy change is about $\Delta G^{0\prime} = -30.5\,\mathrm{kJ/mol} = -0.32\,\mathrm{eV} = -12\,k_BT$. Under physiological conditions in a cell, this leads to about $\Delta G \approx -50\,\mathrm{kJ/mol} = -20\,k_BT = -83\,\mathrm{pN} \times \mathrm{nm}$. ADP can be further hydrolysed to AMP. The used ADP can be recombined to ATP by ATP synthases by using the energy gained e.g. from the oxidation of glucose.

Cilia Whips that cover the surfaces of mammalian respiratory passages (e.g. the nose) where they move outwards particles that have been collected in the secretions of these tissues. Some protozoa are also covered with cilia used for locomotion. They beat with typical frequencies of 5-10 s^{-1} thus producing a sidewards motion. Their structure strongly resembles that of flagella, however they are shorter.

Duty ratio The fraction of time a motor spends in the strongly bound state [70]. It is low for nonprocessive motors like muscle myosin and close to 100% for processive motors like kinesin.

Dynein A family of microtubule-associated motor proteins. There are two classes of dyneins: axonemal dyneins involved in ciliary and flagellar movement and cytoplasmic dyneins involved in intracellular transport (minus-end directed). A dynein molecule is larger and more complex than a kinesin molecule [54].

Flagellum

(1) Bacterial: a helical filament of the polymerised protein flagellin. It is attached to the rotatory bacterial flagellar motor. If the rotor rotates counterclockwise, several flagella draw together into a coherent bundle and the bacterium swims uniformly into one direction. If the rotor starts rotating clockwise, the flagella fly apart and the bacterium starts tumbling. The switching between directed and random motion gives the bacterium a simple mechanism to search for places with higher food concentration.

(2) Eucaryotic: used by sperm cells and certain protozoa for cell propulsion. It is about 50 microns long, 0.25 μm in diameter, and can generate waves with a constant amplitude and a typical frequency of 30 s^{-1}, thus propelling the cell. The waves usually spread from the cell towards the end of the flagellum, but there are also some exceptions [34]. A flagellum contain a bundle

of microtubules, called the axoneme. The waves are generated by several different kinds of dynein motors which are placed between the microtubules and pull them along each other.

Gliding assays (also called *in vitro* motility assays) Experiments in which motors are fixed on a surface while actin or tubulin filaments move in a worm-like fashion over them [93, 162, 60].

Kinesin superfamily Family of kinesin-like motor proteins; its representatives are usually dimeric (two-headed) and move along microtubules by hydrolysing ATP. They are involved in intracellular transport of vesicles and organelles [166] and chromosome movement during cell division.

Kinesin A motor protein with usually two heads that moves processively along microtubules (towards their plus-end) by hydrolysing ATP. It is involved in the vesicle transport to the cell periphery.

Microtubule A hollow tube with 24 nm diameter and up to several tens of micrometers long. It is assembled of tubulin heterodimers forming protofilaments. Usually a microtubule is built up of 13 protofilaments, but other values between 11 and 16 are also possible. Monomers are placed on a rhombic lattice, wound up to form (in the 13-protofilament-microtubules) three left-handed helices with a pitch of 12 nm (3 subunits). Microtubules have a defined polarity (+ and − end).

Microtubules are a component of the cytoskeleton and serve as tracks for the motion of kinesin and dynein motors. They are are further involved in the formation of mitotic spindles which sort the chromosomes during the cell division. They are also involved in the movement of cilia and flagella. Polymerisation of microtubules on one end combined with depolymerisation on the other end can lead to intriguing oscillations [27].

Myosin Motor protein family with representatives involved in muscle contraction and a variety of functions in the cytoskeleton. In muscles, myosin molecules bind together by means of self-assembly and form thick filaments.

ncd Non-claret disjunctional; a motor from the kinesin superfamily involved in chromosome segregation during cell division. It is "−" directed and non-processive [4].

Optical tweezers (laser tweezers) An experimental technique for positioning and tracking microscopic particles like single motor molecules. The observed molecule is attached to a dielectric (e.g. silica) bead with a diameter of about $0.5\,\mu$m. It is then held in a sharply focused laser beam. Since a dielectric is always pulled into an electric field, the bead becomes trapped in the focus [6, 147]. In addition, the position of the bead can be tracked with nanometer precision by interferometric methods.

Power stroke A conformational change in the motor molecule connected with force generation.

Processivity A motor is processive when a single molecule can make a large number of steps without dissociating from its track [58]. Double-headed kinesin is well known to be processive (recently a processive kind of myosin has been discovered as well [115]). A biochemical measure for the processivity is the constant $k_{\mathrm{bi(ratio)}}$ [57], giving the ratio between the ATP hydrolysis rate and the landing rate of a motor on its track. Its value is about 1 for myosin and about 100 for dimeric kinesin.

Protofilament Polymerised tubulin heterodimer with 8 nm periodicity which represents the longitudinal unit in a microtubule. A microtubule is usually composed of 13 protofilaments.

Sarcomere The basic contractile unit in a muscle. It is few microns long and few microns wide. It contains thick (myosin) filaments in the middle and thin (actin) filaments that slide between, thus causing the contraction.

Thick filament Myosin filament in muscle.

Thin filament Actin filament in muscle.

Tubulin Protein with a molecular weight of about $50,000$ and a diameter of about 4 nm. There are two different kinds of tubulin: α and β-tubulin. An α and a β subunit together form a tubulin heterodimer. Several heterodimers one after another can form a protofilament, which further assemble to microtubules. The kinesin binding site is located on the β subunit [148]. In vitro, tubulin can also be assembled to flat sheets.

Bibliography

[1] B. A. Afzelius, Asymmetry of cilia and of mice and men, *Int. J. Dev. Biol.* **43** (1999) 283.

[2] B. Alberts, D. Bray, J. Lewis, M. Raff, K. Roberts and J. D. Watson, *Molecular Biology of the cell*, Garland Publ., New York, 3rd edition, 1994.

[3] F. C. Alcaraz, M. Droz, M. Henkel and V. Rittenberg, Reaction-diffusion processes, critical-dynamics, and quantum chains, *Annals of Physics* **230** (1994) 250.

[4] M. W. Allersma, F. Gittes, M. J. deCastro, R. J. Stewart and C. F. Schmidt, Two-dimensional tracking of ncd motility by back focal plane interferometry, *Biophys. J.* (1998) 1043.

[5] I. Arnal, F. Metoz, S. DeBonis and R. H. Wade, Three-dimensional structure of functional motor proteins on microtubules, *Curr. Biol.* **6** (1996) 1265.

[6] A. Ashkin, Forces of a single-beam gradient laser trap on a dielectric sphere in the ray optics regime, *Biophys. J.* **61** (1992) 569.

[7] R. D. Astumian, Thermodynamics and kinetics of a Brownian motor, *Science* **276** (1997) 917.

[8] R. D. Astumian and M. Bier, Mechanochemical coupling of the motion of molecular motors to ATP hydrosysis, *Biophys. J.* **70** (1996) 637.

[9] R. D. Astumian and I. Derényi, A chemically reversible Brownian motor: application to kinesin and ncd, *Biophys. J.* **77** (1999) 993.

[10] C. R. Bagshaw, *Muscle Contraction*, Chapman & Hall, London, 1993.

[11] P.-A. Bares and M. Mobilia, Diffusion-limited reactions of hard-core particles in one dimension, *Phys. Rev. E* **59** (1999) 1996.

[12] M. Barma, M. D. Grynberg and R. B. Stinchcombe, Jamming and kinetics of deposition-evaporation systems and associated quantum spin models, *Phys. Rev. Lett.* **70** (1993) 1033.

[13] R. Bartussek, P. Hänggi and J. G. Kissner, Periodically rocked thermal ratchets, *Europhys. Lett.* **28** (1994) 459.

[14] R. Becker and W. Döring, Kinetische Behandlung der Keimbildung in übersättigten Dämpfen, *Annalen der Physik (V)* **24** (1935) 719.

[15] H. C. Berg and R. A. Anderson, Bacteria swim by rotating their flagellar filaments, *Nature* **245** (1973) 380.

[16] K. Binder and D. P. Landau, Monte carlo calculations on phase transitions in adsorbed layers, *Adv. Chem. Phys.* **76** (1989) 91.

[17] S. M. Block and K. Svoboda, Analysis of high resolution recordings of motor movement, *Biophys. J.* **68** (1995) 230s.

[18] L. Bourdieu, T. Duke, M. B. Elowitz, D. A. Winkelmann, S. Leibler and A. Libchaber, Spiral defects in motility assays: A measure of motor protein force, *Phys. Rev. Lett.* **75** (1995) 176.

[19] P. Boyer, The ATP synthase - a splendid molecular machine, *Annu. Rev. Biochem.* **66** (1997) 717.

[20] S. T. Brady, A novel brain ATPase with properties expected for the fast axonal transport motor, *Nature* **317** (1985) 73.

[21] C. J. Brokaw, Computer simulation of flagellar movement: IV. properties of an oscillatory two-state cross-bridge model, *Biophys. J.* **16** (1976) 1029.

[22] C. J. Brokaw, Control of flagellar bending: A new agenda based on dynein diversity, *Cell Motil. Cytoskeleton* **28** (1994) 199.

[23] C. J. Brokaw, Microtubule sliding, bend initiation, and bend propagation parameters of ciona sperm flagella altered by viscous load, *Cell Motil. Cytoskeleton* **33** (1996) 6.

[24] S. Camalet, F. Jülicher and J. Prost, Self-organized beating and swimming of internally driven filaments, *Phys. Rev. Lett.* **82** (1999) 1590.

[25] J. Cardy, Renormalization group approach to reaction–diffusion problems, in *Proceedings of mathematical beauty of physics*, edited by J.-B.

ZUBER, volume 24 of *Advanced Series in Mathematical Physics*, page 113, 1997, cond-mat/9607163.

[26] J. CARDY and U. C. TÄUBER, Field theory of branching and annihilating random walks, *J. Stat. Phys.* **90** (1998) 1.

[27] M. F. CARLIER, R. MELKI, D. PANTALONI, T. L. HILL and Y. CHEN, Synchronous oscillations in microtubule polymerization, *Proc. Natl. Acad. Sci. (USA)* **84** (1987) 5257.

[28] Y. CHEN and B. BRENNER, On the regeneration of the actin-myosin power stroke in contracting muscle, *Proc. Natl. Acad. Sci. (USA)* **90** (1993) 5148.

[29] C. M. COPPIN, J. T. FINER, J. A. SPUDICH and R. D. VALE, Detection of sub-8-nm movements of kinesin by high-resolution optical-trap microscopy, *Proc. Natl. Acad. Sci. (USA)* **93** (1996) 1913.

[30] C. M. COPPIN, D. W. PIERCE, L. HSU and R. D. VALE, The load dependence of kinesin's mechanical cycle, *Proc. Natl. Acad. Sci. (USA)* **94** (1997) 8539.

[31] I.-T. C. CREVEL, A. LOCKHART and R. A. CROSS, Weak and strong states of kinesin and ncd, *J. Molec. Biol.* **257** (1996) 66.

[32] Z. CSAHÓK, F. FAMILY and T. VICSEK, Transprot of elastically coupled particles in an asymmetric periodic potential, *Phys. Rev. E* **55** (1997) 5179.

[33] T. L. DANIEL, A. C. TRIMBLE and P. B. CHASE, Compliant realignment of binding sites in muscles: transient behavior and mechanical tuning, *Biophys. J.* **74** (98) 1611.

[34] J. DARNELL, H. LODISH and D. BALTIMORE, *Molecular Cell Biology*, Scientific American Books, 2 edition, 1990.

[35] I. DERÉNYI and T. VICSEK, Cooperative transport of Brownian particles, *Phys. Rev. Lett.* **75** (1995) 374.

[36] I. DERÉNYI and T. VICSEK, The kinesin walk: A dynamic model with elastically coupled heads, *Proc. Natl. Acad. Sci. (USA)* **93** (1996) 6775.

[37] P. DIMROTH, H. WANG, M. GRABE and G. OSTER, Energy transduction in the sodium F-ATPase of propienignium modestum, *Proc. Natl. Acad. Sci. (USA)* **96** (1999) 4924.

[38] M. Dogterom and B. Yurke, Measurement of the force-velocity relation for growing microtubules, *Science* **278** (1998) 856.

[39] F. Downton, A note on vacancies on a line, *J. Roy. Statist. Soc. B* **23** (1961) 207.

[40] T. Duke, E. Holy and S. Leibler, "Gliding assays" for motor proteins: A theoretical analysis, *Phys. Rev. Lett.* **74** (1995) 330.

[41] T. Duke and S. Leibler, Motor protein mechanics: A stochastic model with minimal mechanochemical coupling, *Biophys. J.* **71** (1996) 1235.

[42] T. J. Duke, Molecular model of muscle contraction, *Proc. Natl. Acad. Sci. (USA)* **96** (1999) 2770.

[43] E. Eisenberg, T. L. Hill and Y. Chen, Cross-bridge model for muscle contraction, *Biophys. J.* **29** (1980) 195.

[44] W. A. Engelhardt and M. N. Ljubimowa, Myosine and adenosinetriphosphate, *Nature* **144** (1939) 668.

[45] J. W. Evans, Random and cooperative sequential adsorption, *Rev. Mod. Phys.* **65** (1993) 1281.

[46] L. P. Faucheux, L. S. Bourdieu, P. D. Kaplan and A. J. Libchaber, Optical thermal ratchet, *Phys. Rev. Lett.* **74** (1995) 1504.

[47] W. O. Fenn, The relation between the work performed and the energy liberated in muscular contraction, *J. Physiol. (London)* **184** (1924) 373.

[48] J. T. Finer, A. D. Mehta and J. A. Spudich, Characterization of single actin-myosin interactions, *Biophys. J.* **68** (1995) 291s.

[49] J. T. Finer, R. M. Simmons and J. A. Spudich, Single myosin molecule mechanics: piconewton forces and nanometre steps, *Nature* **368** (1994) 113.

[50] M. E. Fisher and A. B. Kolomeisky, The force exerted by a molecular motor, *Proc. Natl. Acad. Sci. (USA)* **96** (1999) 6597.

[51] P. J. Flory, *J. Am. Chem. Soc.* **61** (1939) 1518.

[52] L. E. Ford, A. F. Huxley and R. M. Simmons, Tension responses to sudden length change in stimulated frog muscle fibres near slack length, *J. Physiol.* **269** (1977) 441.

[53] E. Frey, K. Kroy, J. Wilhelm and E. Sackmann, Statistical mechanics of semiflexible polymers: Theory and experiments, in *Dynamical*

Networks in Physics and Biology, edited by D. Beysens and G. Forgacs, EDP Sciences - Springer, Berlin, 1998, cond-mat/9707021.

[54] I. R. Gibbons, Dynein ATPases as microtubule motors, *J. Biol. Chem.* **263** (1988) 15837.

[55] I. Glyn, Two millennia of animal spirits, *Nature* **402** (1999) 353.

[56] J. Gray and G. J. Hancock, The propulsion of sea urchin spermatozoa, *J. Exp. Biol.* **32** (1955) 802.

[57] D. D. Hackney, Highly processive microtubule-stimulated ATP hydrolysis by dimeric kinesin head domains, *Nature* **377** (1995) 448.

[58] W. Hancock and J. Howard, Processivity of the motor protein kinesin requires two heads, *J. Cell. Biol.* **140** (1998) 1395.

[59] W. Hancock and J. Howard, Kinesin's processivity results from mechanical and chemical coordination between the ATP hydrolysis cycles of the two motor domains, *Proc. Natl. Acad. Sci. (USA)* **96** (1999) 13147.

[60] Y. Harada, A. Noguchi, A. Kishino and T. Yanagida, Sliding movement of single actin filaments on one-headed myosin filaments, *Nature* **326** (1987) 805.

[61] U. Henningsen and M. Schliwa, Reversal in the direction of movement of a molecular motor, *Nature* **389** (1997) 93.

[62] H. Higuchi, T. Yanagida and Y. E. Goldman, Compliance of thin filaments in skinned fibres of rabbit skeletal muscle, *Biophys. J.* **69** (1995) 1000.

[63] A. V. Hill, The heat of shortening and dynamic constants of muscle, *Proc. R. Soc. London Ser. B* **126** (1939) 136.

[64] T. L. Hill, *Cooperativity Theory in Biochemistry*, Springer Series in Molecular Biology, Springer-Verlag, New York, 1985.

[65] K. Hirose, R. A. Cross and L. A. Amos, Nucleotide-dependent structural changes in dimeric NCD molecules complexed to microtubules, *J. Molec. Biol.* **278** (1998) 389.

[66] K. Hirose, A. Lockhart, R. A. Cross and L. A. Amos, Three-dimensional cryoelectron microscopy of dimeric kinesin and ncd motor domains on microtubules, *Proc. Natl. Acad. Sci. (USA)* **93** (1996) 9539.

[67] A. Hoenger, E. P. Sablin, R. D. Vale, R. J. Fletterick and R. A. Milligan, Three-dimensional structure of a tubulin–motor-protein complex, *Nature* **376** (1995) 271.

[68] A. Hoenger, S. Sack, M. Thormählen, A. Marx, J. Müller, H. Gross and E. Mandelkow, Image reconstruction of microtubules decorated with monomeric and dimeric kinesis: Comparison with X-ray structure and implications for motility, *J. Cell. Biol.* **141** (1998) 419.

[69] J. Howard, The movement of kinesin along microtubules, *Annu. Rev. Physiol.* **58** (1996) 703.

[70] J. Howard, Molecular motors: structural adaptations to cellular functions, *Nature* **389** (1997) 561.

[71] J. Howard, A. J. Hudsepth and R. D. Vale, Movement of microtubules by single kinesin molecules, *Nature* **342** (1989) 154.

[72] A. J. Hunt, F. Gittes and J. Howard, The force exerted by a single kinesin molecule against a viscous load, *Biophys. J.* **67** (1994) 766.

[73] A. F. Huxley, Muscle structure and theories of contraction, *Prog. Biophys. Biophys. Chem.* **7** (1957) 255.

[74] A. F. Huxley and R. M. Niedergerke, Structural changes in muscle during contraction. interference microscopy of living muscle fibres, *Nature* **173** (1954) 971.

[75] A. F. Huxley and R. M. Simmons, Proposed mechanism of force generation in striated muscle, *Nature* **233** (1971) 533.

[76] H. E. Huxley, The double array of filaments in cross-striated muscle, *Biophysic. and Biochem. Cytol.* **3** (1957) 631.

[77] H. E. Huxley, The mechanism of muscular contraction, *Science* **164** (1969) 1356.

[78] H. E. Huxley and J. Hanson, The cross-striations of muscle during contraction and stretch and their structural interpretation, *Nature* **173** (1954) 973.

[79] H. E. Huxley, A. Stewart, H. Sosa and T. Irving, X-ray diffraction measurements of the extensibility of actin and myosin filaments in contracting muscle, *Biophys. J.* **67** (1994) 2411.

[80] A. Ishijima, H. Kojima, H. Higuchi, Y. Harada, T. Funatsu and T. Yanagida, Multiple- and single-molecule analysis of the actomyosin motor by nanometer-piconewton manipulation with a microneedle: unitary steps and forces, *Biophys. J.* **70** (1996) 383.

[81] F. Jülicher, A. Ajdari and J. Prost, Modeling molecular motors, *Rev. Mod. Phys.* **69** (1997) 1269.

[82] F. Jülicher and R. Bruinsma, Motion of RNA polymerase along DNA: a stochastic model, *Biophys. J.* **74** (1998) 1169.

[83] F. Jülicher and J. Prost, Cooperative molecular motors, *Phys. Rev. Lett.* **75** (1995) 2618.

[84] F. Jülicher and J. Prost, Spontaneous oscillations of collective molecular motors, *Phys. Rev. Lett.* **78** (1997) 4510.

[85] W. Kabsch, H.-G. Mannherz, D. Suck, E. F. Pai and K. C. Holmes, Atomic structure of actin:DNase I complex, *Nature* **347** (1990) 37.

[86] M. Kikkawa, T. Ishiwata, T. Wakabayashi and N. Hirokawa, Three-dimensional structure of the kinesin head-microtubule complex, *Nature* **376** (1995) 274.

[87] K. Kitamura, M. Tokunaga, A. H. Iwane and T. Yanagida, A single myosin head moves along an actin filament with regular steps of 5.3 nanometers, *Nature* **397** (1999) 129.

[88] H. Kojima, A. Ishijima and T. Yanagida, Direct measurement of stiffness of single actin filaments with and without tropomyosin by in vitro nanomanipulation, *Proc. Natl. Acad. Sci. (USA)* **91** (1994) 12962.

[89] H. Kojima, E. Muto, H. Higuchi and T. Yanagida, Mechanics of single kinesin molecules measured by optical trapping nanometry, *Biophys. J.* **73** (1997) 2012.

[90] A. J. Kolan, E. R. Nowak and A. V. Tkachenko, Glassy behavior of the parking lot model, *Phys. Rev. E* **59** (1999) 3094.

[91] H. A. Kramers and G. H. Wannier, Statistics of the two-dimensional ferromagnet. part I., *Phys. Rev.* **60** (1941) 252.

[92] K. Krebs, M. P. Pfanmüller, B. Wehefritz and H. Hinrichsen, Finite-size scaling studies of one-dimensional reaction-diffusion systems, *J. Stat. Phys.* **78** (1995) 1429.

[93] S. J. Kron and J. A. Spudich, Fluorescent actin filaments move on myosin fixed to a glass surface, *Proc. Natl. Acad. Sci. (USA)* **83** (1986) 6272.

[94] K. Kroy and E. Frey, Force-extension relation and plateau modulus for wormlike chains, *Phys. Rev. Lett.* **77** (1996) 306.

[95] F. J. Kull, E. P. Sablin, R. Lau, R. J. Fletterick and R. D. Vale, Crystal structure of the kinesin motor domain reveals a structural similarity to myosin, *Nature* **380** (1996) 550.

[96] S. C. Kuo, J. Gelles, E. Steuer and M. P. Scheetz, A model for kinesin movement from nanometer-level movements of kinesin and cytoplasmic dynein and force measurements, *Journal of Cell Science* **Suppl. 14** (1991) 135.

[97] B. P. Lee, Renormalization group calculation for the reaction $kA \to 0$, *J. Phys. A.* **27** (1994) 2633.

[98] S. Leibler, Moving forward noisliy, *Nature* **370** (1994) 412.

[99] S. Leibler and D. Huse, Porters versus rowers: A unified stochastic model of motor proteins, *J. Cell. Biol.* **121** (1993) 1357.

[100] B. Lewis and J. C. Anderson, *Nucleation and Growth of Thin Films*, chapter 4, Academic Press, London, 1978.

[101] C. B. Lindemann and K. S. Kanous, A model for flagellar motility, *Int. Rev. Cytol.* **173** (1997) 1.

[102] A. A. Lushnikov, Binary reaction $1 + 1 \to 0$ in one dimension, *Phys. Lett. A* **120** (1987) 135.

[103] R. W. Lymn and E. W. Taylor, Mechanism of adenosine trophosphate hydrolysis by actomyosin, *Biochemistry* **10** (1971) 4617.

[104] F. MacKintosh, J. Käs and P. Janmey, Elasticity of semiflexible biopolymer networks, *Phys. Rev. Lett.* **75** (1995) 4425.

[105] J. Maddox, Making models of muscle contraction, *Nature* **365** (1993) 203.

[106] J. Maddox, More models for muscle movement, *Nature* **368** (1994) 287.

[107] J. Maddox, The unexpected science to come, *Sci. Am.* **281** (1999) 62.

[108] M. O. Magnasco, Forced thermal ratchets, *Phys. Rev. Lett.* **71** (1993) 1477.

[109] E. Mandelkow and M. Thormählen, private communication.

[110] E.-M. Mandelkow and E. Mandelkow, Tau in Alzheimer's disease, *Trends in Cell Biol.* **8** (1998) 425.

[111] J. D. McGhee and P. H. von Hippel, Theoretical aspects of dna-protein interactions: Co-operative and non-co-operative binding of large ligands to a one-dimensional homogeneous lattice, *J. Molec. Biol.* **86** (1974) 469.

[112] R. B. McQuistan and D. Lichtman, Exact occupation kinetics of one-dimensional arrays of dumbbells, *J. Math. Phys.* **9** (1968) 1680.

[113] A. D. Mehta, J. T. Finer and J. A. Spudich, Detection of single-molecule interactions using correlated thermal diffusion, *Proc. Natl. Acad. Sci. (USA)* **94** (1997) 7927.

[114] A. D. Mehta, M. Rief, J. A. Spudich, D. A. Smith and R. M. Simmons, Single-molecule biomechanics with optical methods, *Science* **283** (1999) 1689.

[115] A. D. Mehta, R. S. Rock, M. Rief, J. A. Spudich, M. S. Mooseker and R. E. Cheney, Myosin-V is a processive actin-based motor, *Nature* **400** (1999) 590.

[116] M. Meister, S. R. Capland and H. C. Berg, Dynamics of a tightly coupled mechnism for flagellar rotation, *Biophys. J.* **55** (1989) 905.

[117] E. Meyhöfer and J. Howard, The force generated by a single kinesin molecule against an elastic load, *Proc. Natl. Acad. Sci. (USA)* **92** (1995) 574.

[118] A. Mogilner and G. Oster, Cell motility driven by actin polymerization, *Biophys. J.* **71** (1996) 3501.

[119] J. E. Molloy, J. E. Burns, J. Kendrick-Jones, R. T. Tregear and D. S. White, Movement and force produced by a single myosin head, *Nature* **378** (1995) 209.

[120] M. Murase and H. Shimitzu, A model of flagellar movement based on cooperative dynamics of dynein-tubulin cross-bridges, *J. Theor. Biol.* **139** (1986) 413.

[121] T. Nishizaka, H. Miyata, H. Hoshikawa, S. Ishiwata and K. Kinosita, Unbinding force of a single motor molecule of muscle measured using optical tweezers, *Nature* **377** (1995) 251.

[122] T. Nishizaka, T. Yagi, Y. Tanaka and S. Ishiwata, Right-handed rotation of an actin filament in an in vitro motile system, *Nature* **361** (1993) 269.

[123] H. Noji, R. Yasuda, M. Yoshida and K. Kinosita, Direct observation of the rotation of F1-ATPase, *Nature* **386** (1997) 299.

[124] R. S. Nord and J. W. Evans, Inequivalent models of irreversible dimer filling: "transition state" dependence, *J. Chem. Phys.* **93** (1990) 8397.

[125] L. Onsager, Reciprocal relations in irreversible processes. I., *Phys. Rev.* **37** (1931) 405.

[126] L. Onsager, Crystal statistics. I. A two-dimensional model with an order-disorder transition, *Phys. Rev.* **65** (1944) 117.

[127] A. Orlova and E. Engelman, Cooperative rigor binding of myosin to actin is a function of F-actin structure, *J. Molec. Biol.* **265** (1997) 469.

[128] E. S. Page, The distribution of vacancies on a line, *J. Roy. Statist. Soc. B* **21** (1959) 364.

[129] A. Parmeggiani, F. Jülicher, A. Ajdari and J. Prost, Energy transduction of isothermal ratchets: Generic aspects and specific examples close to and far from equilibrium, *Phys. Rev. E* **60** (1999) 2127.

[130] L. Peliti, Renormalization of fluctuation effects in the $A + A \to A$ reaction, *J. Phys. A.* **18** (1986) L365.

[131] C. S. Peskin, G. M. Odell and G. F. Oster, Cellular motions and thermal fluctuations: The Brownian ratchet, *Biophys. J.* **65** (1993) 316.

[132] C. S. Peskin and G. Oster, Coordinated hydrolysis explains the mechanical behavior of kinesin, *Biophys. J.* **68** (1995) 202s.

[133] G. Piazessi and V. Lombardi, A cross-bridge model that is able to explain mechanical and energetic properties of shortening muscle, *Biophys. J.* **68** (1995) 1966.

[134] R. J. Podolsky, Kinetics of muscular contraction: the approach to the steady state, *Nature* **188** (1960) 666.

[135] V. Privman and P. Nielaba, Diffusional relaxation in dimer deposition, *Europhys. Lett.* **18** (1992) 673.

[136] J. Prost, J. F. Chauwin, L. Peliti and A. Ajdari, Asymmetric pumping of particles, *Phys. Rev. Lett.* **72** (1994) 2652.

[137] Z. Rácz, Diffusion-controlled annihilation in the presence of particle sources: Exact results in one dimension, *Phys. Rev. Lett.* **55** (1985) 1707.

[138] S. Ray, E. Mayhöfer, R. A. Milligan and J. Howard, Kinesin follows the microtubule's protofilament axis, *J. Cell. Biol.* **121** (1993) 1083.

[139] I. Rayment, H. M. Holden, M. Whittaker, C. B. Yohn, M. Lorenz, K. C. Holmes and R. A. Milligan, Structure of the actin-myosin complex and its implications for muscle contraction, *Science* **261** (1993) 58.

[140] P.-A. Rey and J. Cardy, Asymptotic form of the approach to equilibrium in reversible recombination reactions, *J. Phys. A.* **32** (1999) 1585.

[141] D. Riveline, A. Ott, F. Julicher, D. A. Winkelmann, O. Cardosso, J. J. Lacapere, S. Magnusdottir, J.-L. Viovy, L. Gorre-Talini and J. Prost, Acting on actin: the electric motility assay, *Eur. Biophys. J.* **27** (1998) 403.

[142] D. Riveline, C. H. Wiggins, R. E. Goldstein and A. Ott, Elastohydrodynamic study of actin filaments using fluorescence microscopy, *Phys. Rev. E* **56** (1997) R1330.

[143] M. J. Schnitzer and S. M. Block, Kinesin hydrolyses one ATP per 8-nm step, *Nature* **388** (1997) 386.

[144] G. Schütz and S. Sandow, Non-Abelian symmetries of stochastic-processes - derivation of correlation-functions for random-vertex models and disordered-interacting particle-systems, *Phys. Rev. E* **49** (1994) 2726.

[145] K. Sekimoto and K. Tawada, Extended time-correlation of in-vitro motility by motor protein, *Phys. Rev. Lett.* **75** (1995) 180.

[146] W. Selke, The ANNNI model – theoretical analysis and experimental application, *Phys. Rep.* **170** (1988) 213.

[147] R. Simmons, Molecular motors: Single-molecule mechanics, *Current Biology* **6** (1996) 392.

[148] Y. H. Song and E. Mandelkow, Recombinant kinesin motor domain binds to beta-tubulin and decorates microtubules with a B surface lattice, *Proc. Natl. Acad. Sci. (USA)* **90** (1993) 1671.

[149] J. L. Spouge, Exact-solutions for a diffusion-reaction process in one dimension, *Phys. Rev. Lett.* **60** (1988) 871.

[150] T. Stearns, Motoring to the finish: Kinesin and dynein work together to orient the yeast mitotic spindle, *J. Cell. Biol.* **138** (1997) 957.

[151] R. B. Stinchcombe, M. D. Grynberg and M. Barma, Diffusive dynamics of deposition-evaporation systems, jamming and broken symmetries in related quantum-spin models, *Phys. Rev. E* **47** (1993) 4019.

[152] F. B. Straub, Actin, *Studies from the Inst. of Med. Chem. Univ. Szeged (reprinted by S. Karger, Basel-New York)* **2** (1943) 3.

[153] K. Svoboda and S. M. Block, Force and velocity measured for single kinesin molecules, *Cell* **77** (1994) 773.

[154] K. Svoboda, P. P. Mitra and S. M. Block, Fluctuation analysis of motor protein movement and single enzyme kinetics, *Proc. Natl. Acad. Sci. (USA)* **91** (1994) 11782.

[155] K. Svoboda, C. F. Schmidt, B. J. Schnapp and S. M. Block, Direct observation of kinesin stepping by optical trapping interferometry, *Nature* **365** (1993) 721.

[156] J. Talbot, G. Tarjus and P. Viot, Sluggish kinetics in the parking lot model, *J. Phys. A.* **32** (1999) 2997.

[157] H. Tanaka, A. Ishijima, M. Honda, K. Saito and T. Yanagida, Orientation dependence of displacements by a single one-headed myosin relative to the actin filament, *Biophys. J.* **75** (1998) 1886.

[158] N. Thomas and R. A. Thornhill, The physics of biological molecular motors, *J. Phys. D.* **31** (1998) 253.

[159] M. Thormählen, A. Marx, S. A. Müller, Y.-H. Song, E.-M. Mandelkow, U. Aebi and E. Mandelkow, Interaction of monomeric and dimeric kinesin with microtubules, *J. Molec. Biol.* **275** (1998) 795.

[160] D. C. Torney and H. M. McConnell, Diffusion-limited reactions in one dimension, *J. Phys. Chem.* **87** (1983) 1941.

[161] D. Toussaint and F. Wilczek, Particle-antiparticle annihilation in diffusive motion, *J. Chem. Phys.* **78** (1983) 2642.

[162] Y. Y. Toyoshima, S. J. Kron, E. M. McNally, K. R. Niebling, C. Toyoshima and J. A. Spudich, Myosin subfragment-1 is sufficient to move actin filaments in vitro, *Nature* **328** (1987) 536.

[163] T. P. Uyeda, H. M. Warrick, S. J. Kron and J. A. Spudich, Quantized velocities at low myosin densities in an in vitro motility assay, *Nature* **352** (1991) 307.

[164] T. Q. Uyeda, P. D. Abramson and J. A. Spudich, The neck region of the myosin motor domain acts as a lever arm to generate movement, *Proc. Natl. Acad. Sci. (USA)* **93** (1996) 4459.

[165] R. D. Vale, T. Funatsu, D. W. Pierce, L. Romberg, Y. Harada and T. Yanagida, Direct observation of single kinesin molecules moving along microtubules, *Nature* **380** (1996) 451.

[166] R. B. Vallee and M. P. Scheetz, Targeting of motor proteins, *Science* **271** (1996) 1539.

[167] C. Veigl, M. L. Bartoo, C. S. White, J. S. Sparrow and J. E. Molloy, The stiffness of rabit skeletal acotmyosin cross-bridges determined with an optical tweezers transducer, *Biophys. J.* **75** (1998) 1424.

[168] C. Veigl, L. M. C. J. D. Jontes, J. S. Sparrow, R. A. Milligan and J. E. Molloy, The motor protein myosin-I produces its working stroke in two steps, *Nature* **398** (1999) 530.

[169] G. G. Vernon and D. M. Wolley, The propagation of a zone of activation along groups of flagellar doublet microtubules, *Exp. Cell Res.* **220** (1995) 482.

[170] A. Vilfan, E. Frey and F. Schwabl, Elastically coupled molecular motors, *Eur. Phys. J. B* **3** (1998) 535.

[171] A. Vilfan, E. Frey and F. Schwabl, Force-velocity relations of a two-state crossbridge model for molecular motors, *Europhys. Lett.* **45** (1999) 283.

[172] K. Visscher, M. J. Schnitzer and S. M. Block, Single kinesin molecules studied with a molecular force clamp, *Nature* **400** (1999) 184.

[173] D. Voet and J. G. Voet, *Biochemistry*, John Wiley & Sons, 2nd edition, 1995.

[174] K. Wakabayashi, Y. Sugimoto, H. Tanaka, Y. Ueno, Y. Takezawa and Y. Amemiya, X-ray diffraction evidence for the extensibility of actin and myosin filaments during muscle contraction, *Biophys. J.* **67** (1994) 2422.

[175] H. Y. Wang, T. Elston, A. Mogilner and G. Oster, Force generation in RNA polymerase, *Biophys. J.* **74** (1998) 1186.

[176] M. D. Wang, M. J. Schnitzer, H. Yin, R. Landick, J. Gelles and S. M. Block, Force and velocity measured for single molecules of RNA polymerase, *Science* **282** (1998).

[177] A. Wegner, Equilibrium of the actin-tropomyosin interaction, *J. Molec. Biol.* **131** (1979) 839.

[178] C. Weigt, A. Wegner and M. Koch, Rate and mechanism of the assembly of tropomyosin with actin filaments, *Biochemistry* **30** (1991) 10700.

[179] J. Wilhelm and E. Frey, Radial distribution function of semiflexible polymers, *Phys. Rev. Lett.* **77** (1996) 2581.

[180] T. Yanagida and A. Ishijima, Forces and steps generated by single myosin molecules, *Biophys. J.* **68** (1995) 312s.

[181] K. Yasuda, Y. Shindo and S. Ishiwata, Synchronous behavior of spontaneous oscillations of sarcomeres in skeletal myofibrils under isotonic conditions, *Biophys. J.* **70** (1996) 1823.

[182] R. Yasuda, H. Noji, K. Kinosita and M. Yoshida, F1-ATPase is a highly efficient molecular motor that rotates with discrete 120 degree steps, *Cell* **93** (1998) 1117.

[183] H. X. Zhou and Y. Chen, Chemically driven motility of Brownian particles, *Phys. Rev. Lett.* **77** (1996) 194.

[184] R. M. Ziff, E. Gulari and Y. Barshad, Kinetic phase transitions in an irreversible surface-reaction model, *Phys. Rev. Lett.* **56** (1985) 2553.